

Fig. 8. Cross-sectional plots at X = 0 km of the inverse solution from (a) fitting the vertical magnetic transfer function alone, (b) fitting the impedance tensor alone, (c) fitting both data types. The data is generated from the synthetic model in Fig. 3b.

straint on background resistivities. As a first example, we consider joint inversion of VTF and the impedance tensor data derived for the synthetic model of Fig. 3a. As above we again tried a range of priori/initial models. Although in general the impedance tensor data can adjust the resistivity background, we still had difficulties getting the joint inversion to converge to the desired 5% misfit level, especially with priori models that differ greatly from the correct background resistivities. In this and other examples, we found that to achieve the target misfit for both data types, it was necessary to first fit the impedances to a half-space model, to determine a prior model for the joint inversion. Even with this additional step, we typically found it necessary to use increased error floors for the VTF data (but not the impedances) to achieve a normalized RMS of one.

Not surprisingly, a $50\,\Omega\,m$ half-space (as in Figs. 5 and 6 of Siripunvaraporn et al., 2005) yields a good fit to the synthetic impedance data for case 1. With error floors set to 15% for VTF data and 5% for impedance tensor data, the joint inversion converged to the target misfit in 5 iterations. In the final iteration (Fig. 7) the two anomalies are recovered with essentially correct background resistivities. In fact, in comparison with the inverse model obtained from inversion of just the impedance data (Fig. 6 of Siripunvaraporn et al., 2005), there is little difference. Clearly, the relatively simple structures in this synthetic example are well enough constrained already by the array of 40 MT sites that addition of the VTF data can add little. In any event, this example demonstrates the consistency of the two datasets, as both can be fit simultaneously with the same inverse solution.

Other synthetic examples demonstrate the potential benefit of joint inversion a bit more clearly. We performed three inversion tests on the second test case, with data generated for the synthetic model of Fig. 3b, as described above. Error floors were set at 10% and 5% for the VTF and the impedance data, respectively. Initial models for all runs are $50\,\Omega$ m half space. The first inversion was performed using just the VTF data, the second with just the impedance tensor, and the last with both data types. All inversion reaches the target misfit of 1 RMS. Fig. 8 displays cross-sectional plots at $X=0\,\mathrm{km}$.

In all cases the conductor is recovered, although for the VTF case the burial depth is greater than what it should be (Fig. 8a). This again

shows that the VTF data can primarily constrain the location of the conductor in the horizontal, but not the vertical. Inversion of the impedance tensor alone recovers the anomalous volume quite well (Fig. 8b), but the conductivity is noticeably above the correct value of 1 Ω m (Fig. 8b). The best results are obtained by the joint inversion, where the resistivity, shape, size and depth of the conductor are close to correct. It is not clear why this example demonstrates a benefit of including VTF data, and the other does not; possibly different results would be obtained if the experiment was repeated with different realizations of random noise added to the data, or if the locations of the MT sites were perturbed, or different initial or prior models were used. Clearly the need to satisfy additional data constraints reduces the effects of noise in the data, and is likely to improve the fidelity of the inverse solution. For more complex structure the value of additional constraints provided by the VTF inversion are even clearer, as we show next by consideration of an example with real data.

5. Numerical experiments on real data

We applied the VTF inversion to the EXTECH dataset (Tuncer et al., 2006), consisting of tensor audio-magnetotelluric (AMT) soundings for 131 stations around the McArthur River mine, Saskatchewan, Canada. The goal in this survey was to use electromagnetic data to detect and map low resistivity graphite which is indicative of unconformity-type uranium deposits. A full description of the survey, and an interpretation of this dataset based on 2-D and 3-D analysis (including inversion with WSINV3D), is given in Tuncer et al. (2006). Further efforts at 3-D interpretation are given in and recently Farquharson and Craven (2008).

Here, we invert VTF and impedance data from 16 periods (from 8000 Hz to 5 Hz) at 131 sites (Fig. 2 of Tuncer et al., 2006), comparing results obtained with the two sorts of responses, separately and in combination. We use a 1000 Ω m half-space as an initial and prior model for all runs, as previous inversion of the impedance tensor suggests that this is a reasonable average background, and should thus produce sensible results when inverting the VTF alone. For inversion of the VTF (T_{zx} and T_{zy}) only, minimum error bars were set at 15% of $(|T_{zx}|^2 + |T_{zy}|^2)^{1/2}$. The inversion required about 8 iterations

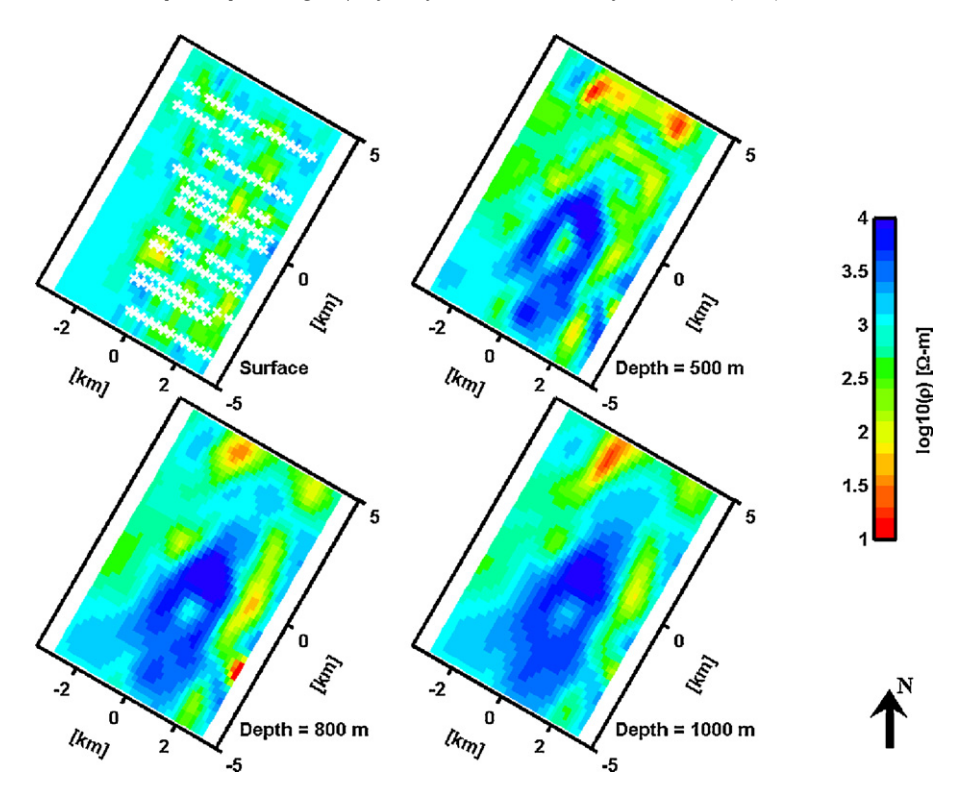


Fig. 9. The inverse solution at various depths from fitting the vertical magnetic transfer functions of the EXTECH dataset. The cross-symbols indicate the location of stations.

to converge to a minimum RMS of 1.2. Results for this inversion are given in Fig. 9.

For the second run we inverted the impedance tensor alone. In previous results using WSINV3D, reported in Tuncer et al. (2006) only the off-diagonal components (Z_{xy} and Z_{yx}) of the impedance were inverted. Here, we used all components including Z_{xx} and Z_{yy}

also. The minimum error bar for this run was set at 5% of $|Z_{xy}^{1/2}Z_{yx}^{1/2}|$ for off-diagonal and 50% for diagonal terms. When the same error floors were tried for off-diagonal and diagonal terms, the misfit could not be reduced below 3 RMS. With the modified error floors, the inversion required 4 iterations to converge to the target level of 1 RMS. The resulting model is shown in Fig. 10. The last run was a joint

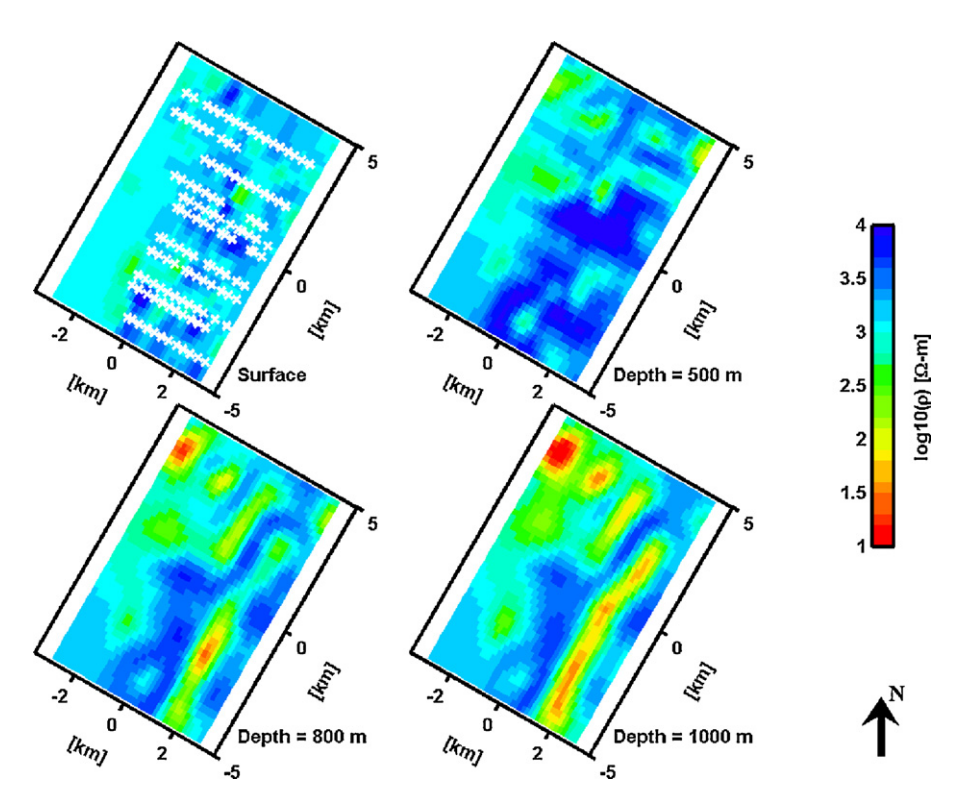


Fig. 10. The inverse solution at various depths from fitting all components of the impedance tensors of the EXTECH dataset.

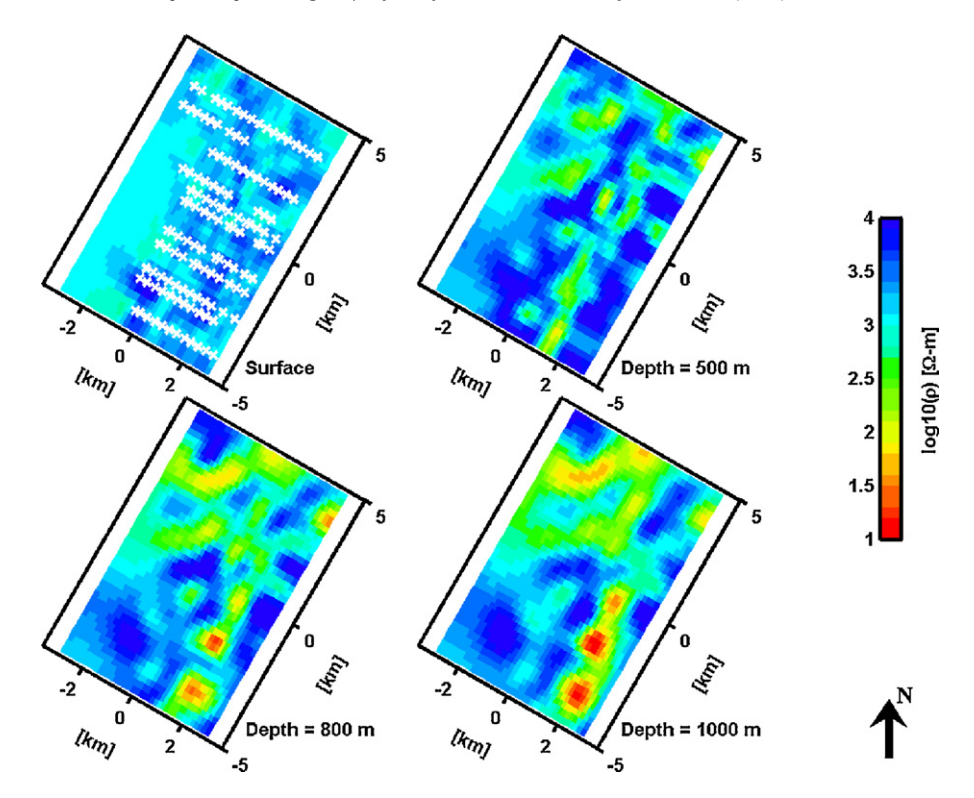


Fig. 11. The inverse solution at various depths from fitting both VTF and the impedance tensors of the EXTECH dataset.

inversion of the full impedance tensor and the vertical magnetic transfer function, with error floors set as in the first two runs. The inversion reduced the RMS misfit to 1.3 in 5 iterations. The model from the joint inversion is shown in Fig. 11.

Inverting just the impedance tensor (Fig. 10) reveals two main zones of high conductivity at 1000 m depth—an elongated feature of about $100\,\Omega\,m$ running perpendicular to the profiles on the east side of the model domain, and an area of variable (but

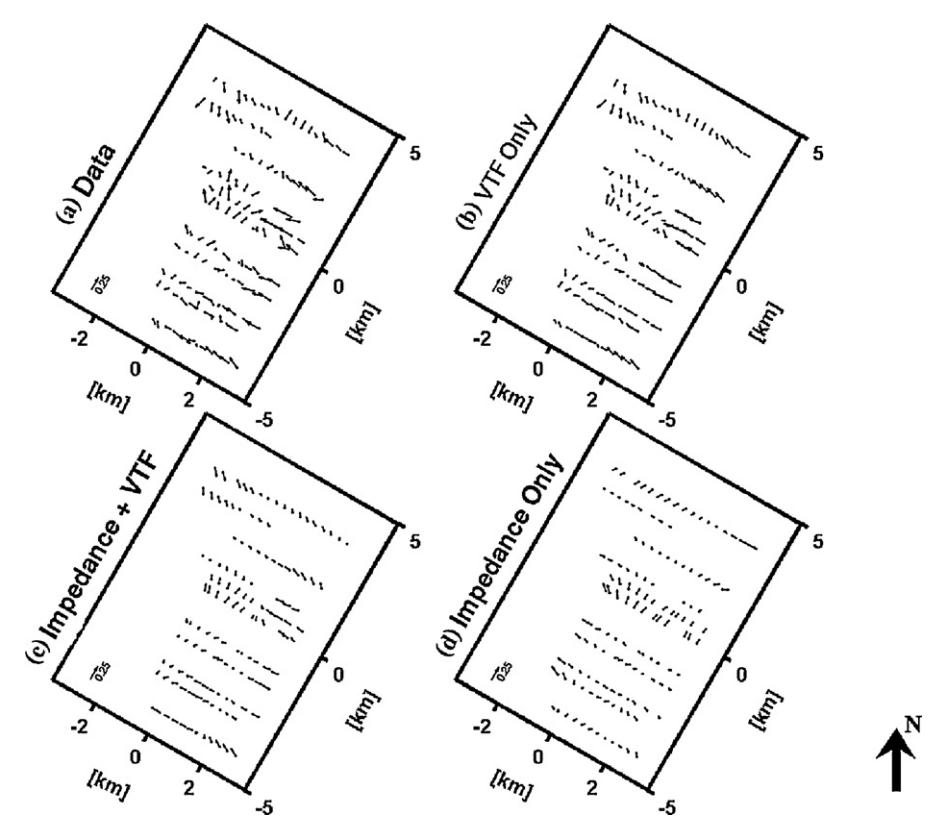


Fig. 12. The induction vectors at 100 Hz generated from (a) the observed VTF data, (b) the VTF inversion alone of Fig. 9, (c) the joint inversion of both impedance tensor and VTF data of Fig. 11, and (d) the impedance tensor inversion alone of Fig. 10. Notice that the calculated induction vectors in (d) fit the observed induction vectors more poorly.

generally higher) conductivity located in the northwest. The same features are evident, but somewhat weaker, in the 800 m layer. Similar features were obtained by inverting only the VTF data (Fig. 9). However, depth resolution appears poorer, as the inversion spreads the conductive features to shallower depths, particularly in the north, beyond the area covered by the MT profiles. The independent inversions of each data type confirm the lateral locations of the conductors. However, based on our experiments with synthetic data, the vertical position and extents of the conductive zones are almost certainly better constrained by the impedance tensor.

Results from joint inversion (Fig. 11) show increased conductivity in the same two general areas at 1000 m depth. However, the elongated conductor to the east now appears to be broken into segments, with patches of resistivity as low as $10\,\Omega$ m, separated by areas with resistivities of several hundred Ω m. In contrast, inverting impedances alone results in a more uniform (approximately $100\,\Omega$ m) continuous feature. Apparently, the VTFs cannot be fit by such a simple uniform conductor, but rather require significant along-strike variability (see Fig. 12). The feature to the north is also substantially modified by inclusion of both data types. Compared to the VTF only inversion, the depth of this feature is now clearly localized at around 1000 m, constrained by the impedance tensor. Inclusion of the VTF data also reduces peak conductivities in this area, and results in more linear conductive features which strike approximately east—west.

It is instructive to consider fits of the inverse solutions of Figs. 9-11 to the VTF data. Real induction vectors (with the Parkinson convention, so that arrows point toward conductors) are plotted in Fig. 12 for a frequency of 100 Hz, along with computed responses for the VTF only, impedance only, and joint inversions. The induction vectors are consistent with the presence of conductive features in the southeastern and northern parts of the array—e.g., note the clear reversal of vectors on most lines as they cross the elongated conductive feature at 1000 m depth (clearest in Fig. 10), and the reversal from South to North pointing vectors in the Northern corner of the study area. However, as noted by Tuncer et al. (2006) patterns in the observations are much more complex than can be reproduced by simple 3-D models. The VTF only inversion reproduces almost all of the complexity seen in the data (Figs. 12a and b). The joint inversion results in a smoother VTF response, and a slightly poorer fit to the data (Fig. 12; this is consistent with the larger error floor assumed in this case), but again, significant features in the data are reproduced in the fitted response. In contrast, the solution obtained from fitting the impedance tensor data alone (Fig. 12c) fits the VTF observations considerably less well, suggesting that the result from the joint inversion (Fig. 11) is more reliable than that from the impedance tensor alone (Fig. 10). A more detailed interpretation of this dataset is beyond the scope of this paper. See Tuncer et al. (2006) and Farquharson and Craven (2008) for further interpretation and discussion of the EXTECH data, and Craven et al. (2006) for comparison of inversion techniques using this data.

6. Conclusions

Experiments on both synthetic and real data show that inverting VTFs alone can recover anomalous structures, particularly if the prior model is close to the correct background or host value. In general, the qualities of the inverse solution obtained from VTF data alone are inferior to those obtained from inverting the impedance tensor alone. Vertical magnetic fields are generated whenever lateral conductivity gradients align with the normal inducing field. Thus, VTFs are sensitive to horizontal structures, and to some extent to resistivity contrasts, but not to depths or absolute values of resistivity. If some constraint on host resistivity can be provided, either *a priori*, or through inversion of impedances, the VTF data

can result in accurate 3-D imaging of the anomalous structures. Joint inversion of VTFs and the impedance tensor can help constrain subsurface structures, as shown in both synthetic and real data examples. In cases with very simple structures which are already well resolved by the impedance data VTFs add little to the inverse solution. However, with more realistic levels of complexity, as exemplified by the EXTECH data, inclusion of VTF data results in significant modifications to the inverse solution. Because the joint inversion model fits both datasets, it is likely to be more reliable.

One issue that deserves further investigation is the inability of the inversion to fit synthetic VTF data to within the tolerance implied by the noise level, which of course is well known in synthetic tests. We speculate that the VTF data can only be fit perfectly when the background resistivity is correct—implying at least a weak sensitivity of this sort of data to the background, as the analysis of Berdichevsky et al. (2003) in fact showed. In the case of using the wrong background resistivity (for which the data have little sensitivity) no nearby model parameters can provide a better fit, perhaps after adjusting conductivities of the anomalous bodies to roughly fit the VTFs, the Occam inversion is stuck in a local minimum of the penalty functional, and cannot escape from. It would be useful to compare other search algorithms (e.g., NLCG) to see if they suffered from similar problems.

A significant drawback with WSINV3DMT has been the large amount of memory required to store the sensitivity matrix, and the extensive computational time required for forward and sensitivity solutions. These drawbacks can be ameliorated by adapting the code to run with MPI to on parallel systems. We have parallelized the computations over frequencies, requiring no significant changes to our forward modeling routine. This approach is probably most appropriate for small cluster type machines. To make efficient use of a cluster or supercomputer with more than a few tens of processors would require different approaches, such as decomposing the modeling domain for the forward solver. We have also parallelized computation of cross products, sharing rows of the sensitivity computed on separate nodes to compute blocks of the coefficient matrix needed for the Gauss-Newton normal equations. The resulting dense system of normal equations can be solved on the master node, or using a parallel solver based on iterative methods. The optimal choice here depends on the size of the data space, with the iterative parallel solver only efficient for large datasets. The speedup of the code on a test dataset with 16 periods is nearly linear (with a coefficient of roughly 0.5) for up to 8 processors, but rolls over for a further increase to 16 processors. Even so, the parallelization should make use of the code on realistic 3-D datasets significantly more practi-

Acknowledgments

This research has been supported by a grant from the Thailand Research Fund (RMU5080025) to W.S., and by grant DE-FG02-06ER15819 from the U.S. Dept. of Energy to G.E. Other partial supports for this work to W.S. are from Thai National Grid Center, Thailand and EMpulse, Canada. The authors would like to thank Jim Carven for allowing us to use EXTECH data sets, and Collin Farquharson, George Helffrich, and an anonymous reviewer for comments that improved the manuscript.

References

Bedrosian, P.A., Unsworth, M.J., Egbert, G.D., Thurber, C.H., 2004. Geophysical images of the creeping segment of the San Andreas fault: implications for the role of crustal fluids in the earthquake process. Tectonophysics 385, 137–158.

Berdichevsky, M.N., Dmitriev, V.I., Golubtsova, N.S., Mershchikova, N.A., Pushkarev, P.Yu., 2003. Magnetovariational sounding: new possibilities, Izvestiya. Physics of the Solid Earth 39, 701–727.

- Choi, J., Moon, S., 1997. A parallel Cholesky factorization routine with a new version of PB-BLAS. In: International Conference on Parallel and Distributed Systems (ICPADS'97), pp. 52–58.
- Constable, C.S., Parker, R.L., Constable, C.G., 1987. Occam's inversion: a practical algorithm for generating smooth models from electromagnetic sounding data. Geophysics 52, 289–300.
- Craven, J.A., Farquharson, C., Mackie, R., Siripunvaraporn, W., Tuncer, V., Unsworth, M., 2006. A comparison of one-, two- and three-dimensional modeling of audiomagnetotellurics data collected at the world's richest uranium mine, Saskatchewan, Canada. In: 18th International Workshop on Electromagnetic Induction in the Earth, El Vendrell, Spain, 17–23 September.
- deGroot-Hedlin, C., Constable, S., 1990. Occam's inversion to generate smooth, twodimensional models from magnetotelluric data. Geophysics 55, 1613–1624.
- Farquharson, C.G., Craven, J.A., 2008. Three-dimensional inversion of Magnetotelluric data for mineral exploration: an example from the McArthur River uranium deposit, Saskatchewan, Canada. J. Appl. Geophys., doi:10.1016/j.jappgeo.2008.02.002.
- Heise, W., Caldwell, T.G., Bibby, H.M., Bannister, S.C., 2008. Three-dimensional modeling of magnetotelluric data from the Rotokawa geothermal field, Taupo volcanic zone, New Zealand. Geophys. J. Int. 173, 740–750.
- Newman, G.A., Alumbaugh, D.L., 2000. Three-dimensional magnetotelluric inversion using non-linear conjugate gradients. Geophys. J. Int. 140, 410–424.
- Oskooi, B., Perdersen, L.B., 2005. Comparison between VLF and RMT methods. A combined tool for mapping conductivity changes in the sedimentary cover. J. Appl. Geophys. 57, 227–241.
- Parker, R.L., 1994. Geophysical Inverse Theory. Princeton University Press.
- Parkinson, W.D., 1959. Directions of rapid geomagnetic variations. Geophys. J. Roy. Astronom. Soc. 2, 1–14.
- Patro, Egbert, G., 2008. Regional conductivity structure of Cascadia: preliminary results from 3D inversion of USArray transportable array magnetotelluric data. Geophys. Res. Lett. 35, L20311, doi:10.1029/2008GL035326.
- Pous, J., Heise, W., Schnegg, P., Munoz, G., Marti, J., Soriano, C., 2002. Magnetotelluric study of the Las Canadas caldera (Tenerife, Canary Islands): structural and hydrogeological implications. Earth Planet. Sci. Lett. 204, 249–263.
- Rodi, W.L., 1976. A technique for improving the accuracy of finite element solutions for Magnetotelluric data. Geophys. J. Roy. Astr. Soc. 44, 483–506.

- Rodi, W.L., Mackie, R.L., 2001. Nonlinear Conjugate Gradients Algorithm for 2-D magnetotelluric inversion. Geophysics 66, 174–187.
- Siripunvaraporn, W., Egbert, G., 2000. An efficient data-subspace inversion method for 2-D magnetotelluric data. Geophysics 65. 791–803.
- for 2-D magnetotelluric data. Geophysics 65, 791–803.

 Siripunvaraporn, W., Egbert, G., Lenbury, Y., 2002. Numerical accuracy of magnetotelluric modeling: a comparison of finite difference approximations. Earth Planets Space 54, 721–725.
- Siripunvaraporn, W., Egbert, G., Lenbury, Y., Uyeshima, M., 2005. Three-dimensional magnetotelluric inversion: data-space method. Phys. Earth Planet. Interiors 150, 3–14.
- Siripunvaraporn, W., Egbert, G., 2007. Data space conjugate gradient inversion for 2-D magnetotelluric data. Geophys. J. Int. 170, 986–994.
- Toh, H., Baba, K., Ichiki, M., Motobayashi, T., Ogawa, Y., Mishina, M., Takahashi, I., 2006. Two-dimensional electrical section beneath the eastern margin of Japan sea. Geophys. Res. Lett. 33, L22309.
- Tuncer, V., Unsworth, M.J., Siripunvaraporn, W., Craven, J.A., 2006. Exploration for unconformity-type uranium deposits with audiomagnetotelluric data: a case study from the McArthur River mine, Saskatchewan, Canada. Geophysics 71, B201–B209.
- Unsworth, M., Bedrosian, P., Eisel, M., Egbert, G., Siripunvaraporn, W., 2000. Along strike variations in the electrical structure of the San Andreas Fault at Parkfield, California. Geophys. Res. Lett. 27 (18), 3021–3024.
- Uyeshima, M., Ogawa, Y., Honkura, Y., Koyama, S., Ujihara, N., Mogi, T., Yamaya, Y., Harada, M., Yamaguchi, S., Shiozaki, I., Noguchi, T., Kuwaba, Y., Tanaka, Y., Mochido, Y., Manabe, N., Nishihara, M., Saka, M., Serizawa, M., 2005. Resistivity imaging across the source region of the 2004 Mid-Niigata Prefecture earthquake (M6.8), central Japan. Earth Planets Space 57, 441–446.
- Wannamaker, P.E., Booker, J.R., Jones, A.G., Chave, A.D., Filloux, J.H., Waff, H.S., Law, L.K., 1989. Resistivity cross section through the Juan de Fuca subduction system and its tectonic implications. J. Geophy. Res. 94 (B10), 14,114–14,127.
- Wannamaer, P.E., Hasterok, D.P., Johnston, J.M., Stodt, J.A., Hall, D.B., Sodergren, T.L., Pellerin, L., Maris, V., Doerner, W.M., Groenewold, K.A., Unsworth, M.J., 2008. Lithospheric dismemberment and magmatic processes of the Great Basin-Colorado Plateau transition, Utah, implied from magnetotellurics. Geochem. Geophys. Geosyst. 9 (5), doi:10.1029/2007GC001886, Q05019.

ภาคผนวก จ. Reprint

Boonchaisuk, S., Vachiratienchai, C., Siripunvaraporn, W., 2008, Two-dimensional direct current (DC) resistivity inversion: Data space Occam's approach, *Physics of the Earth and Planetary Interiors* 168 (3-4), pp. 204-211



Contents lists available at ScienceDirect

Physics of the Earth and Planetary Interiors

journal homepage: www.elsevier.com/locate/pepi



Two-dimensional direct current (DC) resistivity inversion: Data space Occam's approach

Songkhun Boonchaisuk, Chatchai Vachiratienchai, Weerachai Siripunvaraporn*

Department of Physics, Faculty of Science, Mahidol University, Rama VI Road, Rachatawee, Bangkok 10400, Thailand

ARTICLE INFO

Article history:
Received 3 October 2007
Received in revised form 25 May 2008
Accepted 30 June 2008

Keywords: Occam's inversion DC resistivity Data-space method

ABSTRACT

A data space Occam's inversion algorithm for 2D DC resistivity data has been developed to seek the smoothest structure subject to an appropriate fit to the data. For traditional model space Gauss–Newton (GN) type inversion, the system of equations has the dimensions of $M \times M$, where M is the number of model parameter, resulting in extensive computing time and memory storage. However, the system of equations can be mathematically transformed to the data space, resulting in a dramatic drop in its dimensions to $N \times N$, where N is the number of data parameter, which is usually less than M. The transformation has helped to significantly reduce both computing time and memory storage. Numerical experiments with synthetic data and field data show that applying the data space technique to 2D DC resistivity data for various configurations is robust and accurate when compared with the results from the model space method and the commercial software RES2DINV.

© 2008 Elsevier B.V. All rights reserved.

1. Introduction

The direct current (DC) resistivity method has been used for various applications in hydrogeological, mining, and geotechnical investigations and environmental surveys (e.g., Ward, 1990; Daily et al., 1992, 1995; Ramirez et al., 1993, 1996; LaBrecque and Ward, 1990; among many others). The measured voltages caused by injected current bring out information on the earth's structure. The inversion program is then applied to interpret the measured voltages to obtain the Earth's resistivity structure.

The development of DC resistivity inversions has progressed successfully. Various techniques have been proposed for the two-dimensional (2D) and three-dimensional (3D) DC resistivity inversion (e.g., Pelton et al., 1978; Tripp et al., 1984; Nariida and Vozoff, 1984; Tong and Yang, 1990; Park and Van, 1991; Ellis and Oldenburg, 1994; Li and Oldenburg, 1994; Sasaki, 1994; Loke and Barker, 1995; Zhang et al., 1995; Loke and Dahlin, 1997, 2002; Tsourlos et al., 1998; Jackson et al., 2001; Pain et al., 2002; Loke et al., 2003; Günther et al., 2006; Pidlisecky et al., 2007; among many others). The most direct approach is the Gauss–Newton (GN) and its variant methods (e.g., Sasaki, 1994; Li and Oldenburg, 1994; Loke and Dahlin, 1997). Other limited memory optimization algorithms are the Quasi–Newton (QN) method (Loke and Barker, 1996; Loke and Dahlin, 1997, 2002; Tsourlos et al., 1998),

the conjugate gradient (CG) type inversion (Zhang et al., 1995) and the non-linear conjugate gradient (NLCG) (Ellis and Oldenburg, 1994). These are the schemes that require the gradient of the function. The derivative-free methods are neural networks (El-Qady and Ushijima, 2001) and genetic algorithms (Schwarzbach et al., 2005).

One of the main disadvantages of the GN-type inversion is that it requires solving a large and dense $M \times M$ system of equations, where M is the number of model parameters. Another disadvantage is the formation of the full $N \times M$ Jacobian or sensitivity matrix. Calculation of the full Jacobian requires a numerical solution of many forward problems. Both disadvantages, consequently, result in extensive computing time and memory storage. For example, in the 3D inversion, the synthetic model of a burial mound and data used by Günther et al. (2006) has 23,109 parameter cells (M = 23,109) which is a lot more than the number of data parameters (N = 3439). Inverting the 23,109 \times 23,109 matrix and forming the Jacobian would require about 4–5 GBytes of RAM and many hours of CPU time.

The problem for the 3D DC resistivity inversion is quite similar to (though not as severe as) that for the 3D magnetotelluric (MT) survey, where the model parameter (*M*) is significantly greater than the data parameter (*N*). Siripunvaraporn and Egbert (2000) and Siripunvaraporn et al. (2005) could overcome this difficulty by transforming the model space inverse problem into the data space problem for their 2D and 3D Magnetotelluric data, respectively. With the transformation, the computational time and memory storage are greatly reduced by a factor of several (Siripunvaraporn and

^{*} Corresponding author. Tel.: +66 2 201 5764; fax: +66 2 354 7159. E-mail address: scwsp@mahidol.ac.th (W. Siripunvaraporn).

Egbert, 2000; Siripunvaraporn et al., 2005). However, formation of the Jacobian matrix is still a requirement.

For the limited memory optimization schemes such as QN, the full Jacobian or sensitivity matrix and the large and dense coefficient matrix of the system of equations are not necessarily constructed. Instead, a multiplication of the Jacobian with any vector can be calculated by solving the forward problem. These methods therefore never require a large memory storage as in GN-type inversions. Another advantage of QN-type inversions over the model space GN-type is their speed. However, their stability may be questionable (Loke and Dahlin, 2002). Though GN-type inversions may use extensive computing time, their main advantages are stability and robustness. They require fewer iterations to converge to the solution than limited memory methods (Loke and Dahlin, 2002; Siripunvaraporn and Egbert, 2007).

Because of their stability, we still have confidence in GN-type inversion techniques, especially Occam's method as first introduced by Constable et al. (1987). Siripunvaraporn and Egbert (2007) showed that for 2D MT data, the computing time of a GN-type inversion in the data space is actually comparable to that of the CG or NLCG inversion. For all of these reasons, here we propose to solve the multi-dimensional DC resistivity inverse problem using one variant GN-technique, Occam's inversion. However, instead of solving the problem in model space as others have (e.g., Constable et al., 1987; Sasaki, 1994), we propose to solve the DC resistivity inverse problem in data space as in Siripunvaraporn and Egbert (2000) and Siripunvaraporn et al. (2004, 2005). In order to test the feasibility and practicality of the data space approach for 3D DC resistivity data, we developed the 2D DC resistivity inversion based on the data space approach of Siripunvaraporn et al. (2005), which will be extended to 3D in the future.

We first start the paper by briefly reviewing the basic idea of Occam's inversion in the usual model space formulation, and then from a data space perspective. We then describe the implementation of the data space technique to a 2D DC resistivity data set. Numerical experiments of both synthetic and real field data in comparison with the commercial software RES2DINV version 3.55 (Loke and Barker, 1996) are shown at the end.

2. Occam's inversion: model space approach versus data space approach

Constable et al. (1987) introduced the Occam method for 1D MT and Schlumberger sounding data. Since then it has become one of the "classic" inversion techniques for various geophysical data (e.g., deGroot-Hedlin and Constable, 1990, 2004; deGroot-Hedlin, 1995; LaBrecque et al., 1996; Siripunvaraporn and Egbert, 2000; Huang et al., 2003; Siripunvaraporn et al., 2005; Greenhalgh et al., 2006; among others). For more general and detailed discussions of the Occam approach, see Constable et al. (1987), deGroot-Hedlin and Constable (1990), Siripunvaraporn and Egbert (2000) and Siripunvaraporn et al. (2004, 2005).

The philosophy of the Occam approach is to seek for the "smoothest" or "minimum" structure model subject to a constraint on the misfit (Constable et al., 1987), which can be mathematically translated into a problem of minimization of an unconstrained functional $U(\mathbf{m}, \lambda)$,

$$\begin{split} U(\mathbf{m}, \lambda) &= (\mathbf{m} - \mathbf{m_0})^T \mathbf{C_m^{-1}} (\mathbf{m} - \mathbf{m_0}) \\ &+ \lambda^{-1} \{ (\mathbf{d} - \mathbf{F}[\mathbf{m}])^T \mathbf{C_d^{-1}} (\mathbf{d} - \mathbf{F}[\mathbf{m}]) - X^{*2} \}. \end{split} \tag{1}$$

Here \mathbf{m} is a resistivity or conductivity model of dimension M, $\mathbf{m_0}$ a base or prior model, $\mathbf{C_m}$ a model covariance matrix which defines the model norm, \mathbf{d} the observed data with dimension N, $\mathbf{F[m]}$ the forward model response, $\mathbf{C_d}$ a data covariance matrix, X^* the desired

level of misfit, and λ^{-1} a Lagrange multiplier. In the 2D DC resistivity case, the data **d** are the apparent resistivities from different configurations. The model response **F**[**m**] is computed by solving the DC resistivity forward problem, which we will describe later.

Instead of directly minimizing (1), Constable et al. (1987) consider the penalty functional $W_{\lambda}(\mathbf{m})$,

$$W_{\lambda}(\mathbf{m}) = (\mathbf{m} - \mathbf{m_0})^{\mathrm{T}} \mathbf{C_m^{-1}} (\mathbf{m} - \mathbf{m_0})$$
$$+ \lambda^{-1} \{ (\mathbf{d} - \mathbf{F}[\mathbf{m}])^{\mathrm{T}} \mathbf{C_d^{-1}} (\mathbf{d} - \mathbf{F}[\mathbf{m}]) \}. \tag{2}$$

When λ is fixed, $\partial U/\partial m$ and $\partial W_{\lambda}/\partial m$ yield the same result. Therefore, minimizing W_{λ} with a series of λ values, and choosing λ for which the smallest minimum is achieved, is equivalent to minimizing the original functional U of (1).

Because of the non-linearity of the inverse problem, the Occam's inversion starts with the linearization of the response function $\mathbf{F}[\mathbf{m}]$ based on the Taylor series expansion, $\mathbf{F}[\mathbf{m}_{k+1}] = \mathbf{F}[\mathbf{m}_k] + \mathbf{J}_k(\mathbf{m}_{k+1} - \mathbf{m}_k)$. Inserting the series expansion in (2), and then solving for the stationary points, a series of iterative approximate solutions is then obtained,

$$\mathbf{m}_{k+1}(\lambda) - \mathbf{m_0} = [\lambda \mathbf{C_m^{-1}} + \mathbf{J_k^T} \mathbf{C_d^{-1}} \mathbf{J_k}]^{-1} \mathbf{J_k^T} \mathbf{C_d^{-1}} \mathbf{d_k}, \tag{3}$$

where $\mathbf{d} = \mathbf{d} - \mathbf{F}[\mathbf{m}_k] + \mathbf{J}_k(\mathbf{m}_k - \mathbf{m}_0)$, the subscript k denotes the iteration number, and $\mathbf{J}_k = (\partial \mathbf{F}/\partial \mathbf{m})_k$ is the $N \times M$ sensitivity or Jacobian matrix calculated at \mathbf{m}_k . Note that the system of Eq. (3) has dimensions of $M \times M$. We therefore called this technique the "model space" Occam's inversion.

Parker (1994) showed that the solution to (3) for iteration k can be transformed to

$$\mathbf{m}_{k+1} - \mathbf{m_0} = \mathbf{C_m} \mathbf{J}_k^{\mathrm{T}} \boldsymbol{\beta}_{k+1}, \tag{4}$$

where β_{k+1} is an unknown expansion coefficient vector. The derivation of (4) from (3) is also given in Siripunvaraporn et al. (2005). Searching for the stationary points with the transformation (4), a series of iterative solutions is again obtained,

$$\mathbf{\beta}_{k+1} = \left[\lambda \mathbf{C_d} + \mathbf{J}_k \mathbf{C_m} \mathbf{J}_k^{\mathrm{T}}\right]^{-1} \mathbf{d}_k. \tag{5}$$

Note that the system of Eq. (5) has dimensions $N \times N$, rather than $M \times M$ as in (3). Here is the main difference between (3) and (5). Because we transform the computation from model space to data space, we therefore called this technique after the transformation the "data space" Occam's inversion. If all the same parameters are used the solutions from both approaches will be identical (Siripunvaraporn and Egbert, 2000; Siripunvaraporn et al., 2005). For MT data, the number of model parameters M is usually much larger than the number of data values N. Both the calculation time and memory are significantly decreased with the transformation to data space (Siripunvaraporn and Egbert, 2000; Siripunvaraporn et al., 2005). Here, we apply this method to DC resistivity data and we expect to gain the same benefits.

The beauty of Occam's inversion is here, which makes it different from other regularized inverse problems. In either the model space or data space approach, the goal is to search for the minimization of (1). This can be performed by two stages. The first stage (Phase I) is to bring the misfit down to the target level by varying λ values in (3) and (5) for each iteration. Once the target misfit is achieved, Phase II keeps the misfit at the desired level and searches for the minimum norm model by again varying λ values in each iteration. The addition of Phase II is to guarantee that the model structure does not contain unwanted or spurious structures (Siripunvaraporn et al., 2004, 2005).

3. Implementations for 2D DC resistivity data

As stated earlier, the goal of this paper is to test the feasibility and practicality of the data space approach to fit general DC resistivity data by using 2D DC resistivity data as an example. To develop the codes, major implementations are the 2D DC resistivity forward modeling and the sensitivity calculation routines. Other parts closely followed Siripunvaraporn and Egbert (2000) and Siripunvaraporn et al. (2005).

3.1. Two-dimensional DC resistivity forward modeling

A first and important step is to develop a 2D DC resistivity forward modeling routine. A good and efficient forward modeling routine helps make the inversion effective because it is the basis of most processes of the inversion. There are many techniques for solving the 2D resistivity forward problem, such as the transmission surface method (Swift, 1971; Madden, 1971; Pelton et al., 1978), the finite difference method (Dey and Morrison, 1979; Mufti, 1976; Mundry, 1984; Lowry et al., 1989) and the finite element method (Coggon, 1971; Rijo, 1977; Pelton et al., 1978; Pridmore et al., 1980, 1981; Uchida and Murakami, 1990; Queralt et al., 1991).

One of the advantages of the finite difference and finite element methods over the other methods is their well-known ability to quickly approximate the solutions for any arbitrary and complex structure models. Finite difference method is relatively fast compared with finite element method. However, to include a general topography, the finite element method becomes a better selection. The DC resistivity survey is usually applied for shallow studies in which the topography must be accounted for. Here, we therefore choose the finite element method for our 2D DC resistivity problem. A brief review of our implementation is stated next. For specific details, readers are encouraged to consult Coggon (1971), Rijo (1977), Queralt et al. (1991), Xu et al. (2000) and Boonchaisuk (2007).

In the 2D DC resistivity forward problem, the governing equation for the electrical potential must be transformed into Fourier space (Pelton et al., 1978; Dey and Morrison, 1979; Uchida and Murakami, 1990; Queralt et al., 1991) to remove the strike direction variable, i.e., from $\phi_{\rm C}$ (x, y, z) into $\varphi_{\rm f}$ (x, $k_{\rm y}$, z), where y is the strike direction, $k_{\rm y}$ is the wave number, and $\phi_{\rm c}$ and $\varphi_{\rm f}$ are the electrical potential in Cartesian coordinates and in Fourier space, respectively. The finite element method, closely following Rijo (1977) and Oueralt et al. (1991), is then applied by using triangular elements for the model discretization. However, the mixed boundary conditions of Queralt et al. (1991) and Dey and Morrison (1979) are imposed at all grid boundaries. These conditions help produce better solutions than the classical ones (Dirichlet or Neumann) (Queralt et al., 1991). For each k_v wave number, the global system of equations $\mathbf{K}\boldsymbol{\varphi}_{\mathbf{f}} = \mathbf{F}$ is then obtained, where \mathbf{K} is the discretized differential operator, $\varphi_{\mathbf{f}}$ is the unknown potential vector in Fourier space and F is the imposed boundary condition. The Cholesky decomposition method is later applied to solve the system of equations to obtain $\varphi_{\mathbf{f}}$.

The final step for the forward modeling routine is to convert the potential vector $\varphi_{\mathbf{f}}$ in Fourier space back to the potential vector $\varphi_{\mathbf{c}}$ in Cartesian coordinates. This process can be done by directly applying the inverse Fourier transform to the Fourier potential. However, in order to obtain an accurate result, a direct computation would require many Fourier potential solutions from various wave numbers k_y (more than 10; Boonchaisuk, 2007). Thus, the number of times required to solve the system of equations $\mathbf{K}\varphi_{\mathbf{f}} = \mathbf{F}$ would be equal to the number of wave numbers n_k used. Xu et al. (2000) proposed an optimization technique that requires at least four wave numbers to generate an accurate solution. Hence we closely fol-

lowed the method of Xu et al. (2000) but slightly adapted it so that the number of wave numbers used is around 8–10.

Once the inverse Fourier transform is performed using the solutions $\varphi_{\mathbf{f}}$ from various k_y , the electrical potentials at the surface can be obtained and are then used to compute the apparent resistivities for any array configuration. Extensive tests on simple to complex models were conducted to guarantee the accuracy of the forward modeling routine. By comparing the results to the analytic solutions (where applicable) and to other existing codes such as the RES2DMOD program version 2.2 (Loke and Barker, 1996), the RMS misfit is about 1% or less. We therefore conclude that our finite element code is accurate and comparable to other existing codes (Boonchaisuk, 2007). Note that our codes are developed only with MATLAB scripts.

3.2. Sensitivity calculation

The sensitivity term $\mathbf{J}_k = (\partial \mathbf{F}/\partial \mathbf{m})_k$ arises inevitably in every nonlinear inversion process. A single sensitivity value denotes the change of the forward response with respect to a change of the model parameter. In general, there are three ways to compute the sensitivity for the DC resistivity (Spitzer, 1998): the perturbation method, the sensitivity forward calculation and the potential approximation. Here, to form the sensitivity matrix \mathbf{J} , we used the adjoint Green's function technique described in McGillivray and Oldenburg (1990). This technique requires a number of forward problem calls of only $n_k \times N$, in contrast with $n_k \times M$ when not using the adjoint method. For a given k_y , since the matrix \mathbf{K} has already been decomposed and stored, the system of equations can then be quickly solved.

3.3. Model covariance

For the data space approach, the model covariance $\mathbf{C}_{\mathbf{m}}$ is the same as that used in Siripunvaraporn et al. (2005). For the model space approach, a roughening matrix similar to those of deGroot-Hedlin and Constable (1990) was used as the inverse of the model covariance.

4. Numerical experiments

In this section, we will investigate the efficiency of our inversion codes for the 2D resistivity data. The first test is performed on synthetic data generated from the two blocks with a contrast resistivity model. Next, we test our codes from the field data collected in our geophysical test area. Our codes are written with MATLAB and run on a personal computer (PC: Pentium IV-3.0 GHz with 1 GB of RAM).

4.1. Examples with synthetic data: two blocks with contrast resistivity model

The synthetic data are generated from the two blocks with the contrast resistivity model shown in Fig. 1. The two $12.5\times20\,m^2$ blocks located next to each other are buried in the $10\,\Omega\,m$ halfspace at $2.5\,m$ from the ground surface. The left block has $100\,\Omega\,m$ and the right block has $1\,\Omega\,m$ (Fig. 1). The apparent resistivity data

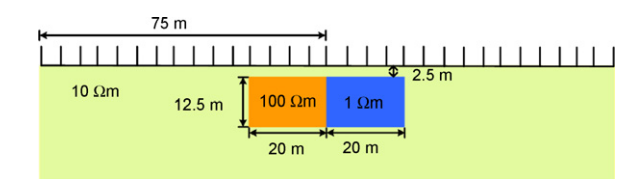


Fig. 1. Two blocks with contrast resistivity model. The solid marks above the surface indicate the measuring electrodes.

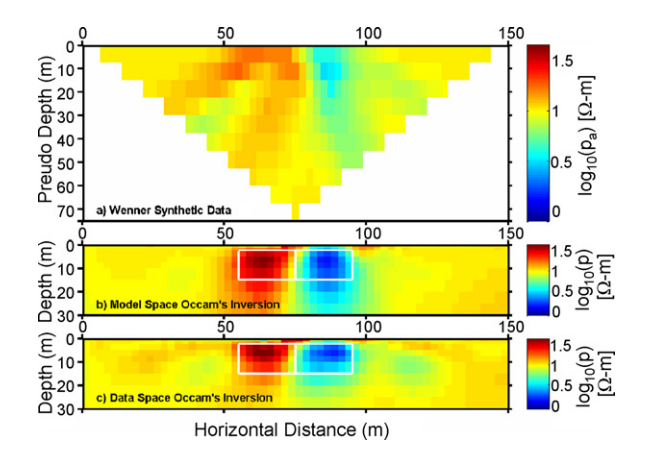


Fig. 2. The solution models from (b) the model space and (c) the data space Occam's program inverted from the synthetic Wenner array data shown in pseudosection (a). White lines indicate the two blocks of Fig. 1.

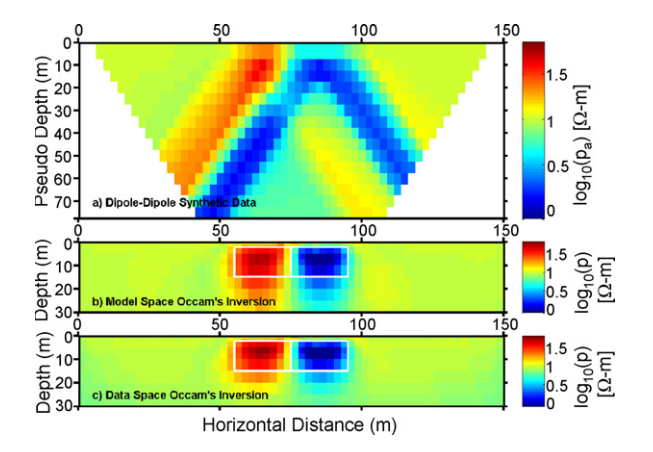


Fig. 3. The solution models from (b) the model space and (c) the data space Occam's program inverted from the synthetic Dipole–Dipole array data shown in pseudosection (a). White lines indicate the two blocks of Fig. 1.

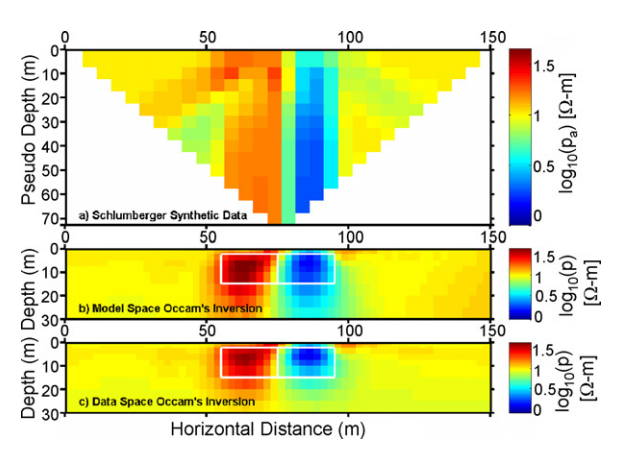


Fig. 4. The solution models from (b) the model space and (c) the data space Occam's program inverted from the synthetic Schlumberger array data shown in pseudosection (a). White lines indicate the two blocks of Fig. 1.

sets for the Wenner, Dipole–Dipole and Schlumberger arrays are obtained from using 31 electrodes with an electrode distance of 5 m and a separation factor of n=1-10 for Wenner (Fig. 2a), n=1-15 for Dipole–Dipole (Fig. 3a) and n=1-14 for Schlumberger arrays (Fig. 4a). These results have N=145 for the Wenner array, 315 for the Dipole–Dipole array and 210 for the Schlumberger array. The finite element mesh used to generate the data is 150×32 in the horizontal and vertical directions, respectively. However, the 80×25 model mesh (M=2000) is used for the inversion. Five percent Gaussian noises were added to the synthetic data. The data variance is set at 5%, calculating from the apparent resistivity to accommodate the discretization errors from using different meshs for the inversion and the forward modeling and the 5% Gaussian noises.

The starting model for the inversion is set to be the same as the base model $(\textbf{m_0})$ which is a homogeneous half-space, with its resistivity value (ρ_{avg}) determined from the geometric mean of the apparent resistivity data $(\rho_a),\,\rho_{avg}=\sqrt[N]{\rho_a^1\cdot\rho_a^2\cdot\dots\cdot\rho_a^N},$. Thus, the geometric mean of apparent resistivity is about 9.22 Ω m for the

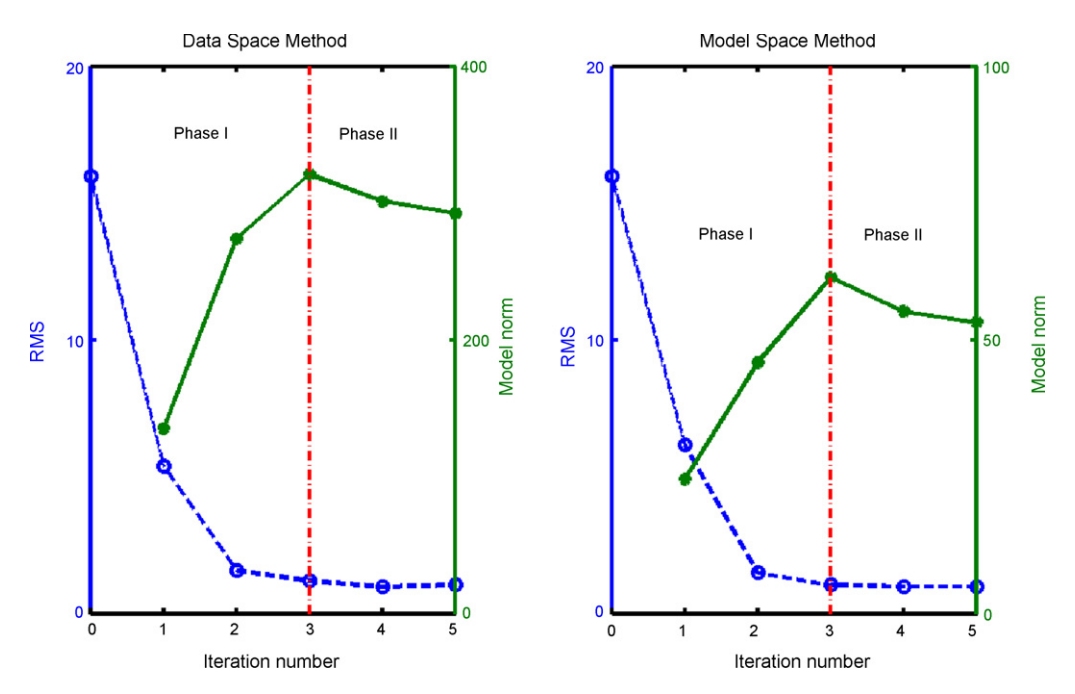


Fig. 5. The RMS misfit (dashed line; left *y*-axis) and model norm (solid line; right *y*-axis) versus the iteration number of the model space (right) and the data space (left) Occam's inversions for the synthetic Dipole–Dipole data (Fig. 3a) generated from two blocks with a contrast resistivity model (Fig. 1).

Wenner data (Fig. 2a), 7.03 Ω m for Dipole–Dipole data (Fig. 3a) and 8.18 Ω m for Schlumberger data (Fig. 4a). The initial RMS is about 6.13 for Wenner, 15.97 for Dipole–Dipole and 12.64 for Schlumberger. The target misfit set for the inversion is equal to 1, implying that the data are being fitted within their error levels of 5%. For Wenner and Schlumberger arrays, both approaches require 3 iterations to complete the minimization of U. For Dipole–Dipole data, the model space method requires 4 iterations, while the data–space method requires 5 iterations (Fig. 5).

Fig. 2b and c displays the final inverted models obtained at the target misfit with the minimum norm after 3 iterations for the Wenner configuration array with the model space and data space Occam's inversion, respectively. Similarly, Fig. 3b and c are for the Dipole–Dipole configuration, and Fig. 4b and c are for the Schlumberger configuration. In all figures, both model and data space approaches can recover both resistivity blocks quite well; however, the qualities may be different. The white line indicates the block boundaries. The top surfaces of the two blocks are clearly seen at a depth around 2.5 m for both methods. However, the bottom boundaries are resolved better with the data space approach. This is probably due to the different model covariance used for both methods.

Fig. 5a and b displays the convergence plot versus iteration number for the model space and data space algorithms, respectively, for Dipole–Dipole configurations. Both inversions requires about 3 iterations to reach the target misfit (Phase I), but require another one or two iterations to complete Phase II for the model or data-space method, respectively. Both programs are terminated in Phase II if the model norm of the next iteration increases or changes only slightly. The right *y*-axis of both figures shows that the model norm is being minimized. Note that the model covariance of the model space and data-space methods is different, resulting in different levels of model norms. Other convergence plots for the Wenner and Schlumberger arrays are similar, and are therefore not shown here.

Computational times for the model space and the data space approaches are not significantly different since the problem is 2D where the model domain is still small. However, in the process of solving the system of equations of the inversion, the model space method must spend more computing time than the data-space method. That is because the inverted matrix has a size of 2000×2000 compared with 315×315 for the data-space method. The time difference would be higher if the model domain were larger as in the case of the 3D problem. In addition, the memory required to store the system of equations is about a factor of 40 times greater in the model space than is required by the data-space method, as expected from the theory (Siripunvaraporn and Egbert, 2000; Siripunvaraporn et al., 2004, 2005).

We have also performed various tests on other synthetic data generated from different models, both simple and complex. We found that our inversion codes in both model space and data-space

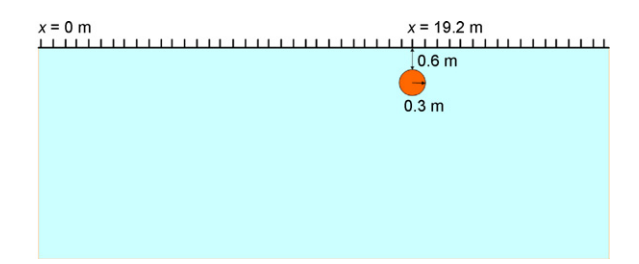


Fig. 6. Location of the drainpipe known a priori from the map of the Faculty of Science, Mahidol University. The solid marks above the surface indicate the electrodes with a spacing of 0.6 m.

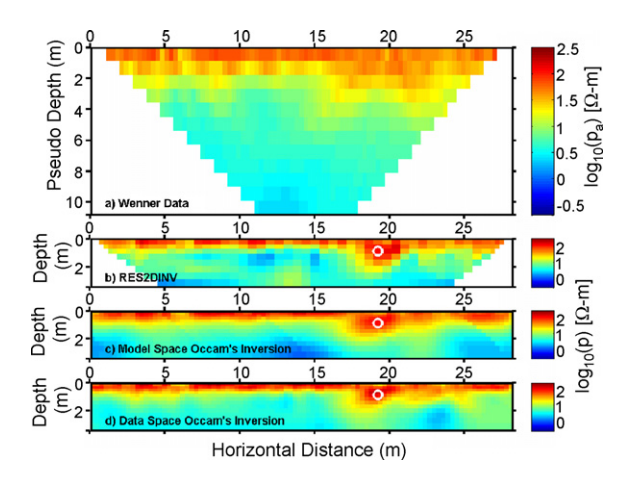


Fig. 7. The solution models from (b) RES2DINV, (c) our model space, and (d) our data space programs inverted from the observed Wenner array data shown in pseudosection (a). The white circle indicates the circular drainpipe in Fig. 6.

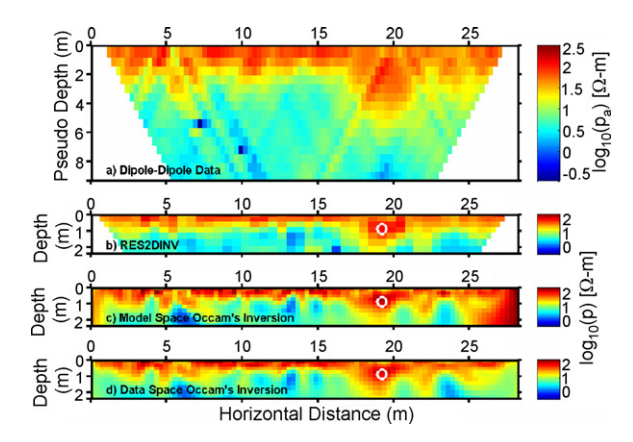


Fig. 8. The solution models from (b) RES2DINV, (c) our model space, and (d) our data space programs inverted from the observed Dipole–Dipole array data shown in pseudosection (a). The white circle indicates the circular drainpipe in Fig. 6.

methods are capable of recovering the anomalies buried inside and background structures of the model (Boonchaisuk, 2007).

4.2. Example with field data

In the previous section, we have shown that our inversion codes work reasonably well with synthetic data. In this section we show

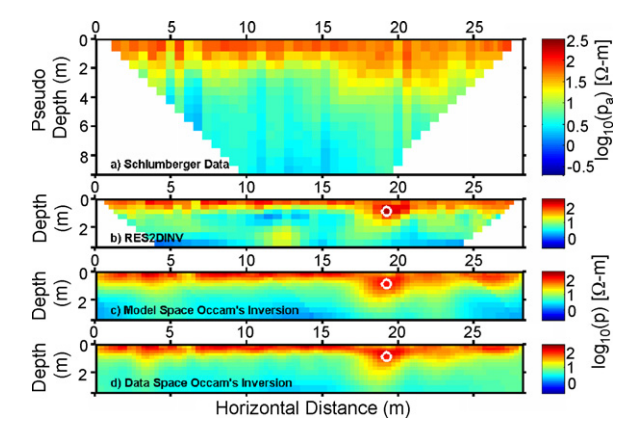


Fig. 9. The solution models from (b) RES2DINV, (c) our model space, and (d) our data space programs inverted from the observed Schlumberger array data shown in pseudosection (a). The white circle indicates the circular drainpipe in Fig. 6.

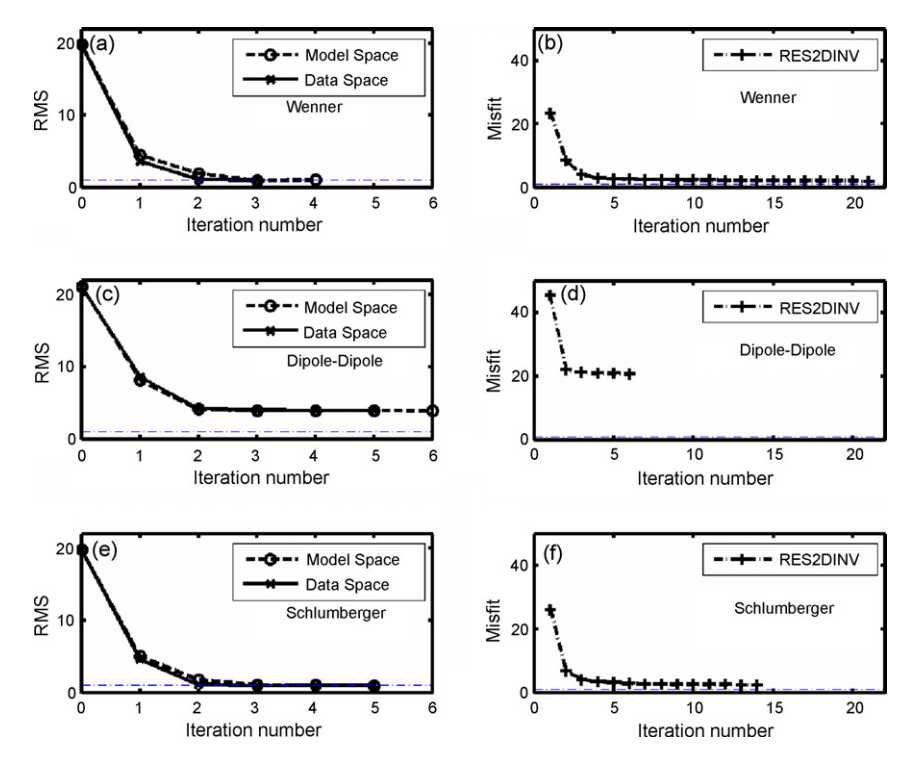


Fig. 10. (a, c, e) The RMS misfits versus the iteration numbers of the model (dashed line) and data space (solid line) methods. (b, d, f) The calculated misfits versus the iteration numbers from the RES2DINV program. Top row is for Wenner data, middle row is for Dipole–Dipole data and bottom row is for Schlumberger data. Note that the RES2DINV program uses a different formula from our RMS misfit to calculate its own misfit.

the flexibility, robustness and accuracy of our codes to the real observed data, which usually contains noise from many sources.

The DC resistivity data were collected at the geophysical test area inside the Faculty of Science, Mahidol University to detect the buried drainpipe; for which the position and depth was known a priori. The circular drainpipe is 0.3 m in radius and is buried at a depth of 0.9 m (from the surface to the center) as shown in Fig. 6. A SYSCAL R1 PLUS Switch-48 instrument was used to collect the observed data. A profile array of 48 electrodes with an electrode spacing of 0.6 m was applied perpendicular to the course of the drainpipe to obtain the 2D data.

Figs. 7a, 8a and 9a display the 335, 555 and 452 observed data values constituted from the Wenner, Dipole–Dipole and Schlumberger configurations, respectively, by using separation factors of 1–12, 1–15 and 1–15, respectively. The 114×21 model mesh is used for the inversions. The data variance is set to 5% of the apparent resistivity to account for the noise from measurement and other sources. The total number of model parameters is therefore 2394 (114×21), and the data parameters are 335, 555 and 452 for Wenner, Dipole–Dipole and Schlumberger configurations, respectively.

Both model space and data space Occam's inversion methods were applied to our field data set, along with the commercial software, RES2DINV version 3.55 (Loke and Barker, 1996), using default parameters of the program in order to provide a reference to our inverted models and to show the accuracy and robustness of our developed codes. The final inverse solutions for Wenner, Dipole–Dipole and Schlumberger data sets are shown in Figs. 7b, 8b and 9b for the RES2DINV program, Figs. 7c, 8c and 9c for our model space code, and Figs. 7d, 8d and 9d for our data space inversion, respectively. All inverted models from our codes and the commercial code show that there are two layers beneath the surface and a high-resistivity portion indicating the drainpipe. The high-resistivity (100 Ω m) top layer is about 1 m in depth lying on top

of the conductive (10 Ω m) layer. The high-resistivity layer is interpreted as the top soil filled on top of the clay conductive layer. The drainpipe is located directly in the high-resistivity zone matching the location plotted in the map.

Fig. 10 shows the misfit plots versus iteration numbers. The RES2DINV misfit is calculated differently from our RMS misfit, so we plot them on separate figures. The left column shows the RMS misfits calculated from our model and data space Occam's inversions (Fig. 10a, c and e). The right column shows the misfits generated from the RES2DINV code (Fig. 10b, d and f). For only the Dipole–Dipole configuration data, the RMS misfit did not converge to the desired misfit of 1 for the model and data-space methods. This also happened for the RES2DINV code, where a high RES2DINV misfit is still shown. In all cases, the RES2DINV code requires more iterations than both types of Occam's inversion.

5. Discussion and conclusions

The data-space method has been widely used in many fields including geophysics (Parker, 1994; Egbert et al., 1994; Chua and Bennett, 2001). It was recently used for MT data by Siripunvaraporn and Egbert (2000) for their 2D code and later applied to a 3D code (Siripunvaraporn et al., 2004, 2005). Here, we have shown that the same technique can be also used for 2D DC resistivity data. In the two examples presented here, we show that our developed 2D data space code is robust and accurate, and comparable to the commercial software RES2DINV program.

For any configuration, N is always less than M by a large factor. This fact helps enhance the benefit of using the data-space method, especially for the GN-type inversions. Since the size of the system of equations is significantly dropped to $N \times N$ from the original $M \times M$ in traditional model space, both the computing time and memory storage of the data-space method become a fraction of those in the model space method. Applying the data-space method to 3D

data would definitely yield an advantage, because in 3D, N/M is much smaller than in the 2D case. However, in the case where M is greater *N* (if occurred), the data space approach would not yield any advantages. In this case, we can select to run our code in the model space. Alternatively, a subset data space inversion, similar to REBOCC code (Siripunvaraporn and Egbert, 2000), can be applied in order to further reduce the computational costs.

Both the model and data space Occam's inversion methods require the full sensitivity matrix. This process consumes extensive computing time and large memory storage. Directly extending our 2D code to a 3D code would still yield an impractical 3D code. However, Siripunvaraporn and Egbert (2007) showed that we can avoid constructing the full sensitivity matrix by applying the conjugate gradient technique. This would help significantly in reducing the size of memory storage; however, the computing time may not necessarily decrease (Siripunvaraporn and Egbert, 2007).

In order to speed up the codes, an approximate sensitivity matrix is another option to consider. The Quasi-Newton method has been used to estimate the sensitivity (Loke and Barker, 1996). It was then used in combination with the GN method in order to maintain the accuracy of the GN method along with the speed of QN method (Loke and Dahlin, 2002). A hybrid method combining the advantages of the data-space method, GN, QN and other techniques is possible and should be explored for the 3D cases.

Acknowledgments

This research has been supported by a Development and Promotion of Science and Technology Talents Project (DPST) scholarship to SB, partially by Thai Center of Excellence for Physics (ThEP) funding to CV and by Thailand Research Fund (TRF: RMU5080025) funding to WS. The authors would like to thank the Faculty of Science, Mahidol University for their support for geophysics instruments. The authors would also like to thank two anonymous reviewers and the editor for their comments to help improve the manuscript.

References

- Boonchaisuk, S., 2007. Two-dimensional direct current resistivity inversion: finite element method. M.Sc. Thesis. Mahidol University.
- Chua, B.S., Bennett, A.F., 2001. An inverse ocean modeling system. Ocean Model. 3, 137-165.
- Coggon, J.H., 1971. Electromagnetic and electrical modeling by the finite element method, Geophysics 36, 132-155.
- Constable, C.S., Parker, R.L., Constable, C.G., 1987. Occam's inversion: a practical algorithm for generating smooth models from electromagnetic sounding data. Geophysics 52, 289-300.
- Daily, W.D., Ramirez, A.L., LaBrecque, D.J., Nitao, J., 1992. Electrical resistivity tomography of vadose water movement. Water Resources 28, 1429-1442.
- Daily, W.D., Ramirez, A.L., LaBrecque, 1995. Electrical resistance tomography during in-situ trichloroethylene remediation at the Savannah River Site. J. Appl. Geophys. 33, 239-249.
- deGroot-Hedlin, C., 1995. Inversion for regional 2-D resistivity structure in the presence of galvanic scatterers. Geophys. J. Int. 122, 877-888.
- deGroot-Hedlin, C., Constable, S., 1990, Occam's inversion to generate smooth, twodimensional models from magnetotelluric data. Geophysics 55, 1613–1624. deGroot-Hedlin, C., Constable, S., 2004. Inversion of magnetotelluric data for 2D
- structure with sharp resistivity contrasts. Geophysics 69, 78-86.
- Dey, A., Morrison, H.F., 1979. Resistivity modeling for arbitrarily shaped twodimensional structures. Geophys. Prosp. 27, 106–136.
- Egbert, G.D., Bennett, A.F., Foreman, M.G., 1994. TOPEX/POSEIDON tides estimated using a global inverse model. J. Geophys. Res. 99, 24821–24852.
- El-Qady, G., Ushijima, K., 2001. Inversion of DC resistivity data using neural networks. Geophys. Prosp. 49, 417–430.
- Ellis, R.G., Oldenburg, D.W., 1994. The pole-pole 3-D DC-resistivity inverse problem: a conjugate-gradient approach. Geophys. J. Int. 119, 187-194.
- Greenhalgh, S.A., Bing, Z., Green, A., 2006. Solutions, algorithms and inter-relations
- for local minimization search geophysical inversion. J. Geophys. Eng. 3, 101–113. Günther, T., Rucker, C., Spitzer, K., 2006. Three-dimensional modeling and inversion of dc resistivity data incorporating topography-II. Inversion. Geophys. J. Int. 166,
- Huang, Z.X., Su, W., Peng, Y.J., Zheng, Y.J., Li, H.Y., 2003. Rayleigh wave tomography of China and adjacent regions. J. Geophys. Res. 108 (B2), ARTN 2073.

- Jackson, P.D., Earland, S.J., Reece, G.J., 2001. 3D resistivity inversion using 2D measurements of the electric field. Geophys. Prosp. 49, 26-39.
- LaBrecque, D.J., Ward, S.H., 1990. Two-dimensional cross-borehole resistivity model fitting. In: S. Ward (Ed.), Geotechnical and Environmental Geophysics, vol. 1, pp. 51-57.
- LaBrecque, D.J., Miletto, M., Daily, W., Ramirez, A., Owen, E., 1996. The effect of noise on Occan's inversion of resistivity tomography data. Geophysics 61,
- Li, Y., Oldenburg, D.W., 1994. Inversion of 3-D DC resistivity data using an approximate inverse mapping. Geophys. J. Int. 116, 527-537.
- Loke, M.H., Barker, R.D., 1995. Least-squares deconvolution of apparent resistivity pseudosections. Geophysics 60, 1682–1690.
- Loke, M.H., Barker, R.D., 1996. Rapid least-squares inversion of apparent resistivity pseudosections by a Quasi-Newton method. Geophys. Prosp. 44,
- Loke, M.H., Dahlin, T., 1997. A combined Gauss-Newton and Quasi-Newton inversion method for the interpretation of apparent resistivity pseudosections. In: Proc. 3rd Meeting of the European Association for Environmental and Engineering Geophysics, 8–11 Sept. 1997, Aarhus, Denmark, pp. 139–142.
- Loke, M.H., Dahlin, T., 2002. A comparison of Gauss-Newton and Quasi-Newton inversion method in resistivity imaging inversion. J. Appl. Geophys. 49, 149-162.
- Loke, M.H., Acworth, I., Dahlin, T., 2003. A comparison of smooth and blocky inversion methods in 2D electrical imaging surveys. Explor. Geophys. 34, 182–187. Lowry, T., Allen, M.B., Shive, P.N., 1989. Singularity removal: a refinement of modeling
- techniques. Geophysics 54, 766-774.
- Madden, T.R., 1971. The resolving power of geoelectric measurements for delineating resistive zones within the crust. In: J.G. Heacock (Ed.), The Structure and Physical Properties of the Earth's Crust: AGU Geophys. Monogr. Srt., vol. 14, 95-105
- McGillivray, Oldenburg, 1990. Methods for calculating Frechet derivatives and sensitivities for the non-linear inverse problem: a comparative study. Geophys. Prosp. 38, 499-524.
- Mufti, I.R., 1976. Finite-difference resistivity modeling for arbitrary shaped twodimensional structures. Geophysics 41, 62-78.
- Mundry, E., 1984. Geoelectrical model calculations for two-dimensional resistivity distribution, Geophys, Prosp. 32, 124-131.
- Nariida, C.S., Vozoff, K., 1984. Two-dimensional DC resistivity inversion for dipoledipole data. IEEE Trans. Geosci. Remote Sens. GE-22, 21-28.
- Pain, C.C., Herwanger, J.V., Worthington, M.H., de Oliveira, C.R.E., 2002. Effective multidimensional resistivity inversion using finite-element techniques. Geophys. J.
- Int. 151, 710–728.
 Park, S.K., Van, G.P., 1991. Inversion of pole-pole data for 3-D resistivity structure beneath arrays of electrodes. Geophysics 56, 951-960.
- Parker, R.L., 1994. Geophysics Inversion Theory. Princeton University Press.
- Pelton, W.H., Rijo, L., Swift, C.M.J.R., 1978. Inversion of two-dimensional resistivity and induced-polarization data. Geophysics 43, 788-803.
- Pidlisecky, A., Haber, E., Knight, R., 2007. RESINVM3D: a 3D resistivity inversion package. Geophysics 72, H1-H10.
- Pridmore, D.F., Hohmann, G.W., Ward, S.H., Sill, W.R., 1980. An investigation of finiteelement modeling for electrical and electromagnetical data in three dimensions. Geophysics 46, 1009-1024.
- Pridmore, D.F., Hohmann, G.W., Ward, S.H., Sill, W.R., 1981. An investigation of finiteelement modeling for electrical and electromagnetic data in three dimensions. Geophysics 46, 1009-1024.
- Queralt, P., Pous, J., Marcuello, A., 1991. 2-D resistivity modeling: an approach to arrays parallel to the strike direction. Geophysics 56, 941-950.
- Ramirez, A.L., Daily, W.D., LaBrecque, D.J., Owen, E., Chesnut, D., 1993. Monitoring an underground steam injection process using electrical resistance tomography. Water Resource Res. 29, 73-87.
- Ramirez, A.L., Daily, W.D., Binley, A.M., LaBrecque, Roelant, D., 1996. Detection of leaks in underground storage tanks using electrical resistance methods. J. Environ. Eng. Geophys. 1, 189-203.
- Rijo, L., 1977, Modeling of electric and electromagnetic data. Ph.D. thesis. University of Utah.
- Sasaki, Y., 1994. 3-D resistivity inversion using the finite element method. Geophysics 55, 1839-1848.
- Schwarzbach, C., Borner, R., Spizer, K., 2005. Two-dimensional inversion of direct current resistivity data using a parallel, multi-objective genetic algorithm. Geophys.
- Siripunvaraporn, W., Uyeshima, M., Egbert, G., 2004. Three-dimensional inversion for Network-Magnetotelluric data. Earth Planets Space 56, 893-902.
- Siripunvaraporn, W., Egbert, G., 2000. An efficient data-subspace inversion method for 2-D magnetotelluric data. Geophysics 65, 791-803.
- Siripunvaraporn, W., Egbert, G., 2007. Data space conjugate gradient inversion for 2-D magnetotelluric data. Geophys. J. Int. 170, 986-994.
- Siripunvaraporn, W., Egbert, G., Lenbury, Y., Uyeshima, M., 2005. Three-dimensional magnetotelluric inversion: data-space method. Phys. Earth Planetary Interiors 150. 3-14.
- Spitzer, K., 1998. The three-dimensional dc sensitivity for surface and subsurface sources. Geophys. J. Int. 134, 736-746.
- Swift Jr., C.M., 1971. Theoretical magnetotelluric and turam response from twodimensional inhomogeneities. Geophysics 36, 38-52.
- Tong, L., Yang, C., 1990. Incorporation of topography into two-dimensional resistivity inversion. Geophysics 55, 354-361.

- Tripp, A.C., Hohmann, G.W., Swift, C.M., 1984. Two-dimensional resistivity inversion. Geophysics 49, 1708–1717.
- Tsourlos, P.I., Szymanski, J.E., Tsokas, G.N., 1998. A smoothness constrained algorithm for the fast 2-D inversion of DC resistivity and induced polarization data. J. Balkan Geophys. Soc. 1, 3–13.
- Uchida, T., Murakami, Y., 1990. Development of Fortran code for the Two-Dimensional Schlumberger Inversion: Geological Survey of Japan Open-File Report No. 150, pp. 1–12.
- Ward, S.H., 1990. Geotechnical and environmental geophysics. Investigat. Geophys. 5, 147–189
- Xu, S., Duan, B., Zhang, D., 2000. Selection of the wavenumber k using an optimization method for the inverse Fourier transform in 2.5D electrical modelling. Geophys. Prosp. 48, 789–796.
- Zhang, J., Mackie, R.L., Madden, T.R., 1995. 3-D resistivity forward modeling and inversion using conjugate gradients. Geophysics 60, 1313–1325.

ภาคผนวกง. Reprint

Kalscheuer, T., Pedersen, L.B., Siripunvaraporn, W., 2008, Radiomagnetotelluric two-dimensional forward and inverse modelling accounting for displacement currents, Geophysical Journal International 175 (2), pp. 486-514

Radiomagnetotelluric two-dimensional forward and inverse modelling accounting for displacement currents

Thomas Kalscheuer, Laust B. Pedersen and Weerachai Siripunvaraporn 2

 $^1Department\ of\ Earth\ Sciences,\ Uppsala\ University,\ Villav\"{a}gen\ 16,75236\ Uppsala,\ Sweden.\ E-mail:\ Thomas. Kalscheuer@geo.uu.se$

Accepted 2008 June 30. Received 2008 June 17; in original form 2007 October 30

SUMMARY

Electromagnetic surface measurements with the radiomagnetotelluric (RMT) method in the frequency range between 10 and 300 kHz are typically interpreted in the quasi-static approximation, that is, assuming displacement currents are negligible. In this paper, the dielectric effect of displacement currents on RMT responses over resistive subsurface models is studied with a 2-D forward and inverse scheme that can operate both in the quasi-static approximation and including displacement currents.

Forward computations of simple models exemplify how responses that allow for displacement currents deviate from responses computed in the quasi-static approximation. The differences become most obvious for highly resistive subsurface models of about $3000\,\Omega\,m$ and more and at high frequencies. For such cases, the apparent resistivities and phases of the transverse magnetic (TM) and transverse electric (TE) modes are significantly smaller than in the quasi-static approximation. Along profiles traversing 2-D subsurface models, sign reversals in the real part of the vertical magnetic transfer function (VMT) are often more pronounced than in the quasi-static approximation. On both sides of such sign reversals, the responses computed including displacement currents are larger than typical measurement errors.

The 2-D inversion of synthetic data computed including displacement currents demonstrates that serious misinterpretations in the form of artefacts in inverse models can be made if displacement currents are neglected during the inversion. Hence, the inclusion of the dielectric effect is a crucial improvement over existing quasi-static 2-D inverse schemes. Synthetic data from a 2-D model with constant dielectric permittivity and a conductive block buried in a highly resistive layer, which in turn is underlain by a conductive layer, are inverted. In the quasi-static inverse model, the depth to the conductive structures is overestimated, artefactual resistors appear on both sides of the conductive block and a spurious conductive layer is imaged at the surface.

High-frequency RMT field data from Ävrö, Sweden, are re-interpreted using the newly developed 2-D inversion scheme that includes displacement currents. In contrast to previous quasi-static modelling, the new inverse models have electrical resistivity values comparable to a normal-resistivity borehole log and boundaries between resistive and conductive structures, which correlate with the positions of seismic reflectors.

Key words: Numerical solutions; Inverse theory; Electrical properties; Electromagnetic theory; Magnetotelluric.

1 INTRODUCTION

Since many electromagnetic (EM) methods utilize frequencies below 10 kHz, the quasi-static assumption that displacement currents are much smaller than conduction currents (i.e. $\omega\epsilon\ll\sigma$ with angular frequency $\omega=2\pi\,f$, dielectric permittivity $\epsilon=\epsilon_r\epsilon_0$, free air permittivity ϵ_0 and electrical conductivity σ) is stipulated and displacement currents are neglected during the data interpretation. For the radiomagnetotelluric (RMT) method, which uses EM fields in the VLF (3–30 kHz) and LF (30–300 kHz) frequency ranges, the validity of the quasi-static assumption is questionable. For a typical relative dielectric permittivity $\epsilon_r=5$ (e.g. mildly fractured crystalline bedrock), displacement currents are equally strong as conduction currents for, for example, an electrical resistivity $\rho=1/\sigma=10\,000\,\Omega$ m and a frequency $f=360\,\mathrm{kHz}$. This means that the dielectric effect is non-negligible even at a combination of lower frequencies and/or resistivities. In fact, it can be argued that the

²Department of Physics, Faculty of Science, Mahidol University, Rama VI Rd., Rachatawee, Bangkok 10400, Thailand

dielectric effect should be accounted for as soon as the perturbation it causes is roughly equal to the measurement errors of the data. For a typical error level of, say, 2 per cent on the impedance tensor elements, vertically incident plane waves and a relative dielectric permittivity $\epsilon_r = 5$, it is shown in Section 3.1 that the effect of displacement currents on the impedance phase is above the error level at, for example, $f = 15 \, \text{kHz}$ and $\rho = 10\,000\,\Omega$ m or $f = 170\,\text{kHz}$ and $\rho = 10000\,\Omega$ m.

In the following subsections, the existing knowledge of the dielectric effect on plane-wave and controlled-source frequency-domain electromagnetic (FDEM) responses is reviewed. With respect to the RMT method, the plane-wave FDEM responses are of special importance. After that, the resolvability of anomalous dielectric permittivities and previous attempts of quasi-static interpretation of high-frequency RMT data are discussed. In the last part of the introduction, we give an outlook at our 2-D inverse scheme for RMT data that allows for displacement currents and summarize the assumptions we make. Note that for the treatment of the FDEM theory, we choose an $\exp +i\omega t$ time dependence throughout this paper.

1.1 Dielectric effect on frequency-domain EM responses

Several publications describe the effect of displacement currents on plane-wave and controlled-source FDEM responses in the VLF and LF frequency ranges, based on analytic solutions by Wait (1953, 1970) and Wait & Nabulsi (1996) for a 1-D layered Earth.

In plane-wave FDEM methods like the RMT method, EM fields generated by powerful radio transmitters operating in the VLF and LF frequency ranges are used as primary signals. The aerials employed with the remote radio transmitters are vertical electric dipoles. At distances beyond several free-air wavelengths from the transmitter, that is, in the so-called far-field zone, the EM field essentially resembles that of a plane wave, which is obliquely incident on the Earth's surface (McNeill & Labson 1991). An excellent summary of the theory of plane-wave FDEM impedance, VMT and wave tilt measurements that covers both the quasi-static approximation and the general case with displacement currents, as well as the nature of the radio transmitter source field, is given by Crossley (1981).

For plane-wave EM fields, Sinha (1977) investigates the influence of displacement currents on the wave tilt, that is, the ratio of the horizontal to vertical electric field. On the surface of a homogeneous half-space, both amplitude and phase approach the values of the quasi-static approximation at low frequencies, although they become significantly smaller than the quasi-static responses with increasing frequency.

The dielectric effect on apparent resistivities and phases of radiomagnetotelluric surface impedances is deduced in Crossley (1981), Zacher (1992) and Persson & Pedersen (2002) from 1-D forward computations. On the surface of a homogeneous half-space, both apparent resistivity and phase are smaller than their constant counterparts in the quasi-static approximation. The differences become stronger with increasing frequency.

Wait (1953), Sinha (1977), Crossley (1981) and Song *et al.* (2002) emphasize the importance of the angle of incidence for wave tilt, surface impedance and VMT measurements conducted with plane-wave FDEM methods. The EM field is transmitted vertically into the Earth, independent of the angle of incidence, when the quasi-static approximation is valid. In the general case with displacement currents, however, the angles of incidence and transmission are related through Snell's law. As a consequence, the TM- and TE-mode impedances vary with the angle of incidence and differ at oblique incidence, even if measured on the surface of a layered half-space (Song *et al.* 2002).

For controlled source air-borne FDEM measurements, Fraser *et al.* (1990), Huang & Fraser (2002) and Yin & Hodges (2005) simulate responses due to a pair of horizontal coplanar transmitting–receiving coils, operating in the frequency range of 0.4 to 100 kHz. The ratio of secondary magnetic field intensity to primary magnetic field intensity is split into an in-phase component (real part) and a quadrature component (imaginary part). According to Fraser *et al.* (1990) and Huang & Fraser (2002), displacement currents in the Earth lead to a decrease of the in-phase component and an increase of the quadrature component, compared with the quasi-static case for which both components are positive. The influence of displacement currents in the air (an increase of both components) is rather small compared with that in the Earth (Yin & Hodges 2005).

1.2 Resolvability of permittivity anomalies

The resolvability of the relative dielectric permittivity from both plane-wave and controlled-source FDEM measurements is assessed by Nabulsi & Wait (1996), Stewart *et al.* (1994), Huang & Fraser (2002) and Persson & Pedersen (2002) with 1-D simulations.

Using obliquely incident plane waves in the VHF range (30–300 MHz), Nabulsi & Wait (1996) illustrate that a dielectric layer embedded in a highly resistive host is detectable if its thickness and relative permittivity are sufficiently high.

For a controlled source coil–coil FDEM method which operates in the MF (0.3–3 MHz) and HF (3–30 MHz) frequency ranges, Stewart *et al.* (1994) show that the anomalous response of both a resistive and conductive thin layer is significantly enlarged by the dielectric effect even if there is no contrast of dielectric permittivity between the layers of the model. Stewart *et al.* (1994) present two field examples, where tilt angle and ellipticity data of the magnetic field polarization ellipse have been successfully inverted for both electric resistivity and dielectric permittivity, with a 1-D inverse scheme.

At frequencies lower than those employed by Nabulsi & Wait (1996) and Stewart *et al.* (1994), displacement currents become weaker and the resolvability of permittivity anomalies within a limited range of possible relative permittivity values deteriorates. Huang & Fraser (2002) (see Section 1.1) estimate a single value of relative permittivity at their highest frequency of 100 kHz, as it is a badly resolved parameter at lower frequencies.

Persson & Pedersen (2002) invert RMT data with frequencies up to $250\,\text{kHz}$ for dielectric permittivity, using 1-D models. The differences of inverse models are found to be negligible if the relative dielectric permittivities are limited to the range between 4 and 10, typical of bedrock, and if the resistivities are not larger than $20\,000\,\Omega$ m (Persson & Pedersen 2002). Relative dielectric permittivities larger than 10 are typical of water bearing sedimentary rocks and soils (Reynolds 1997). Due to the high water content, such formations have relatively low resistivities (typically up to about $500\,\Omega$ m), which reduce the importance of displacement currents at VLF and LF frequencies. It is therefore sufficient, in many practical cases of RMT data interpretation, to account for displacement currents by selecting a dielectric permittivity representative of high-resistivity structures in the subsurface.

1.3 Quasi-static interpretation of high-frequency RMT data

The difficulties of the interpretation of high-frequency RMT field data in the quasi-static approximation are discussed by Persson & Pedersen (2002) and Linde & Pedersen (2004). For synthetic 1-D RMT impedance responses computed with displacement currents, Persson & Pedersen (2002) compare 1-D inversion results from inverse schemes that utilize both the quasi-static approximation and displacement currents. For a homogeneous half-space model, neglecting displacement currents during the inversion leads to an inverse model with a conductor close to the surface, followed by alternating layers of high and low resistivity at depth (Persson & Pedersen 2002). Similarly, Linde & Pedersen (2004) observe for quasi-static 1-D inversions of RMT field data from the island Ävrö, Sweden, that a conductive surface layer is modelled more conductive and the underlying unfractured bedrock is modelled more resistive than in the 1-D inversions with displacement currents. The models, due to inversion with displacement currents, are supported by logging data of Gentzschein *et al.* (1987).

In fact, the work presented by Linde & Pedersen (2004) is a typical example of the interpretation strategies chosen until now, in cases where the dielectric effect in RMT data is to be accounted for. In the absence of a 2-D inversion program that allows for displacement currents, the data interpretation has, so far, been restricted to 1-D inversions with modified analytic forward and Frechet derivative routines, the exclusion of the higher frequency data in 2-D inversions and 3-D forward modelling with the integral equation code X3D by Avdeev *et al.* (2002).

1.4 2-D inversion of RMT data allowing for displacement currents

For the first time, we take displacement currents in a 2-D forward and inverse modelling scheme for RMT data into account by selecting a value of dielectric permittivity that is typical of the subsurface and assuming vertically incident plane waves. As the EM field from remote VLF transmitters can be expected to be incident at an angle closer to 90° (grazing incidence), it is shown in Section 2.2 that the presence of a moderately resistive surface layer reduces the influence of the angle of incidence considerably. We investigate the effect of displacement currents on 2-D forward responses in the TM-mode, the TE-mode and the VMT and compare our results with the responses computed by the integral equation code X3D by Avdeev *et al.* (2002), which, at the time of writing, was the only forward code known to us that operates in two or three dimensions and includes displacement currents. Especially, the effect on VMT responses was not considered in the past (*cf.* Avdeev *et al.* 2002; Persson & Pedersen 2002). Possible misinterpretations, in the form of artefacts with excessively extreme resistivities in models from quasi-static inverse schemes, are highlighted. The RMT data from Ävrö (Linde & Pedersen 2004) are re-interpreted with the inverse scheme that allows for displacement currents. The resulting inverse models are compared with the borehole data of Gentzschein *et al.* (1987) and the seismic reflection model of Juhlin & Palm (1999).

We have added our forward and sensitivity routines, which allow for displacement currents, to the popular 2-D magnetotelluric inverse code REBOCC by Siripunvaraporn & Egbert (2000).

2 THEORY

2.1 Electromagnetic equations

Assuming a volume of conductivity σ , dielectric permittivity ϵ and vacuum permeability μ_0 , Maxwell's equations are written in the frequency domain as

$$\nabla \times \mathbf{E} = -(i\omega\mu_0)\mathbf{H} = -\hat{\mathbf{z}}\mathbf{H} \qquad \text{Faraday's law} \tag{1}$$

$$\nabla \times \mathbf{H} = (\sigma + i\omega\epsilon)\mathbf{E} = \hat{\mathbf{y}}\mathbf{E} \qquad \text{Ampere's law}$$
 (2)

$$\nabla \cdot (\epsilon \mathbf{E}) = q \qquad \qquad \text{Gauss' law} \tag{3}$$

$$\nabla \cdot \mathbf{H} = 0 \tag{4}$$

where $\mathbf{E}^{\mathrm{i}\omega t}$ and $\mathbf{H}^{\mathrm{i}\omega t}$ are the electric and magnetic field vectors, varying in time t, with angular frequency ω (e.g. Ward & Hohmann 1987) and q is the charge density. On the right-hand sides of eqs (1) and (2), the definitions of the impedivity $\hat{z} = \mathrm{i}\omega\mu_o$ and admittivity $\hat{y} = \sigma + \mathrm{i}\omega\epsilon$ are used. The quantities $\mathbf{j}_{\mathrm{cond}} = \sigma \mathbf{E}$, $\mathbf{j}_{\mathrm{disp}} = \mathrm{i}\omega\epsilon\mathbf{E}$, and $\mathbf{j} = \hat{y}\mathbf{E}$ are the conduction, displacement and total current densities, respectively. The

displacement current density $i\omega\epsilon E$ describes the dielectric effect due to electronic, atomic, molecular and space charge derived polarization of matter with dielectric permittivity ϵ in the presence of a time-varying electric field (Keller 1987). In the case that conduction currents dominate over displacement currents (i.e. $\sigma \gg \omega\epsilon$), displacement currents may be neglected in eq. (2). This simplification is known as the quasi-static approximation.

In the following, it is assumed that plane waves are obliquely incident on the Earth's surface in the y-z plane and that the x-direction is the geoelectrical strike direction. Therefore, the admittivity \hat{y} and the EM field components vary only in y and z direction. This choice leads to the definition of the transverse electric (TE) and transverse magnetic (TM) modes for which the vertical electrical and vertical magnetic field components, respectively, vanish. The sets of equations for the TE- and TM-modes are

(1) TE-mode:

$$\frac{\partial H_z}{\partial y} - \frac{\partial H_y}{\partial z} = \hat{y} E_x,\tag{5}$$

$$\frac{\partial E_x}{\partial z} = -\hat{z}H_y,\tag{6}$$

$$\frac{\partial E_x}{\partial y} = \hat{z}H_z. \tag{7}$$

(2) TM-mode:

$$\frac{\partial E_z}{\partial y} - \frac{\partial E_y}{\partial z} = -\hat{z}H_x,\tag{8}$$

$$\frac{\partial H_x}{\partial z} = \hat{y} E_y,\tag{9}$$

$$\frac{\partial H_x}{\partial y} = -\hat{y}E_z. \tag{10}$$

An illustration of the EM field components of the TM-mode and a 2-D subsurface with a cylindrical structure of anomalous electrical properties and infinite extension along the *x*-axis, that is, the strike direction, is given in Fig. 1. The EM field is obliquely incident at an angle θ_0 , thereby having a wavenumber vector $\mathbf{k}_0 = (0, k_{0y}, k_{0z})$. According to the definition of the TM-mode, the incident, reflected and transmitted magnetic fields $\mathbf{H}_i = (H_{ix}, 0, 0)$, $\mathbf{H}_r = (H_{rx}, 0, 0)$, and $\mathbf{H}_t = (H_{tx}, 0, 0)$, respectively, are all directed along the strike direction whereas the incident, reflected and transmitted electric fields $\mathbf{E}_i = (0, E_{iy}, E_{iz})$, $\mathbf{E}_r = (0, E_{ry}, E_{rz})$, and $\mathbf{E}_t = (0, E_{ty}, E_{tz})$, respectively, are all directed perpendicularly to the strike direction.

In the quasi-static approximation of the TM-mode, $\mathbf{j} = (0, \sigma E_y, \sigma E_z)$ vanishes in the air half-space (Brewitt-Taylor & Weaver 1976) where $\sigma_{air} = 0$ is assumed. As a consequence of eqs (9) and (10), H_x is then constant in the air half-space, and an inclusion of the air half-space in the modelling domain can be omitted. If displacement currents are accounted for, the magnetic field in the air is no longer independent of the resistivity distribution in the Earth, as the vertical component of the current density is continuous at the air–Earth interface

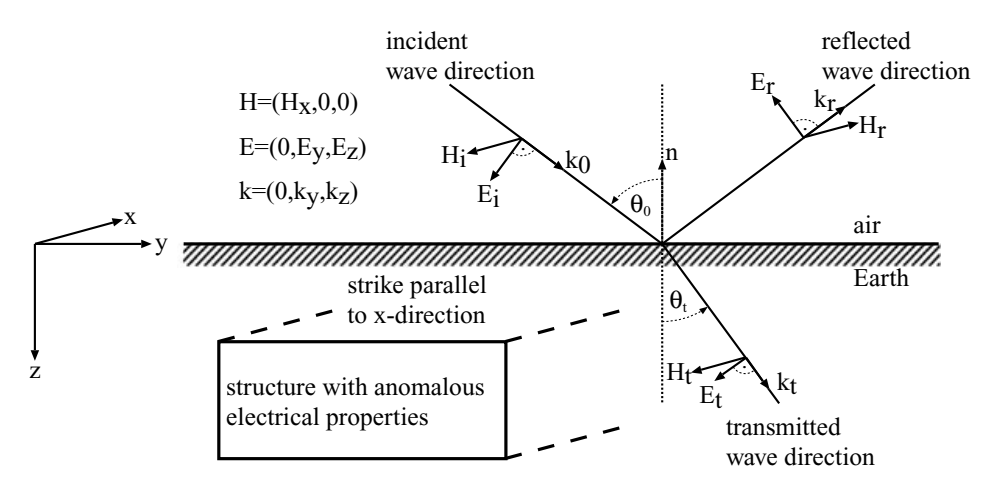


Figure 1. EM field components of the TM-mode on a 2-D earth model. The model consists of a structure with anomalous electrical properties that has its strike direction parallel to the *x*-axis. The EM field is obliquely incident at an angle θ_0 , thereby having a wavenumber vector $\mathbf{k}_0 = (0, k_{0y}, k_{0z}) = (0, k_0 \sin \theta_0, k_0 \cos \theta_0)$. The incident, reflected and transmitted magnetic fields $\mathbf{H}_i = (H_{ix}, 0, 0)$, $\mathbf{H}_r = (H_{rx}, 0, 0)$ and $\mathbf{H}_t = (H_{tx}, 0, 0)$, respectively, are all directed and transmitted electric fields $\mathbf{E}_i = (0, E_{iy}, E_{iz})$, $\mathbf{E}_r = (0, E_{ry}, E_{rz})$, and $\mathbf{E}_t = (0, E_{ty}, E_{tz})$, respectively, are all directed perpendicular to the strike direction. On top of a conductive subsurface, the electromagnetic field is refracted towards the normal, that is, $\theta_t < \theta_0$.

and in the air,

$$j_{y} = \hat{y}E_{y} = i\omega\epsilon_{0}E_{y} = \frac{\partial H_{x}}{\partial z},\tag{11}$$

$$j_z = \hat{y}E_z = i\omega\epsilon_0 E_z = -\frac{\partial H_x}{\partial y} \tag{12}$$

differ from zero (cmp. eqs 9 and 10). Hence, the air half-space must be included in the simulation of the TM-mode.

The electric and magnetic field components E_x and H_x of the TE- and TM-modes, respectively, fulfil the Helmholtz equations (cf. eqs. 1 and 2)

$$-(\nabla \times \nabla \times \mathbf{E})_{x} = -[\nabla(\nabla \cdot \mathbf{E})]_{x} + (\nabla^{2}\mathbf{E})_{x}$$

$$= \frac{\partial^{2} E_{x}}{\partial y^{2}} + \frac{\partial^{2} E_{x}}{\partial z^{2}}$$

$$= \hat{z}\hat{y}E_{x}$$
(13)

and

$$-\left(\nabla \times \frac{1}{\hat{y}} \nabla \times \mathbf{H}\right)_{x} = -\frac{1}{\hat{y}} \left[\nabla(\nabla \cdot \mathbf{H})\right]_{x} + \frac{1}{\hat{y}} \nabla^{2} H_{x} - \left[\left(\nabla \frac{1}{\hat{y}}\right) \times \nabla \times \mathbf{H}\right]_{x}$$

$$= \frac{1}{\hat{y}} \left(\frac{\partial^{2} H_{x}}{\partial y^{2}} + \frac{\partial^{2} H_{x}}{\partial z^{2}}\right) + \frac{\partial}{\partial y} \left(\frac{1}{\hat{y}}\right) \cdot \frac{\partial H_{x}}{\partial y} + \frac{\partial}{\partial z} \left(\frac{1}{\hat{y}}\right) \cdot \frac{\partial H_{x}}{\partial z}$$

$$= \hat{z} H_{x}, \tag{14}$$

where the 2-D assumption $\partial/\partial x = 0$ and eq. (4) were used.

In a homogeneous volume, for instance, the general solution of the scalar Helmholtz equations (eqs 13 and 14) is given by

$$\{E, H\}_{x} = \left(\{E, H\}_{x}^{++} e^{-ik_{z}z} + \{E, H\}_{x}^{-+} e^{ik_{z}z}\right) e^{-ik_{y}y} + \left(\{E, H\}_{x}^{+-} e^{-ik_{z}z} + \{E, H\}_{x}^{--} e^{ik_{z}z}\right) e^{+ik_{y}y}.$$

$$(15)$$

Here, k_y and k_z are the horizontal and vertical components of the wavenumber vector \mathbf{k} (see above). The substitution of eq. (15) into eq. (13) yields

$$k^2 = k_y^2 + k_z^2 = -\hat{z}\hat{v} \tag{16}$$

where $k_y = k \sin \theta$ and $k_z = k \cos \theta$. The complex wavenumber can be split as $k = \alpha - i\beta$ where the real numbers α and β represent propagation and attenuation, respectively, and

$$\alpha = \omega \sqrt{\frac{\mu_0 \epsilon}{2} \left[\sqrt{1 + \frac{\sigma^2}{\epsilon^2 \omega^2} + 1} \right]},\tag{17}$$

$$\beta = \omega \sqrt{\frac{\mu_0 \epsilon}{2} \left[\sqrt{1 + \frac{\sigma^2}{\epsilon^2 \omega^2} - 1} \right]}. \tag{18}$$

The inverse of the imaginary part gives the skin depth $\delta = \frac{1}{\beta}$ over which the amplitude of the EM field is reduced by a factor 1/e. In the quasi-static approximation, the real and imaginary parts are equal, that is, $\alpha = \beta = \sqrt{\frac{\omega \mu_0 \sigma}{2}}$.

The reflection and refraction of plane EM waves at the Earth's surface are governed by Snell's law and the Fresnel equations (Ward & Hohmann 1987). Hence, the EM field measured on the Earth's surface depends on the angle of incidence (see Fig. 1). Three cases of the angle of incidence θ_0 are distinguished. The cases $\theta_0 = 0^\circ$ and $\theta_0 = \pm 90^\circ$ are known as normal (or vertical) incidence and grazing (or parallel) incidence, respectively. The cases $90^\circ > \theta_0 > 0^\circ$ and $0^\circ > \theta_0 > -90^\circ$ are called oblique incidence. The refraction of obliquely incident EM waves into the subsurface is conveniently demonstrated for a layered half-space. As a consequence of the boundary conditions for the EM field components at layer interfaces, the horizontal component of the wavenumber vector is constant (Ward & Hohmann 1987), that is,

$$k_{y,j} = k_0 \sin \theta_0 = k_j \sin \theta_j. \tag{19}$$

Here, $k_0 = \sqrt{\omega^2 \mu_0 \epsilon_0}$ is the wavenumber of the air and θ_0 is the angle of incidence. Similarly, k_j and θ_j are the wavenumber and angle of transmission of the *j*th layer, respectively. According to eqs (16) and (19) the vertical wavenumber of the *j*th layer has the form

$$k_{z,j} = k_j \cos \theta_j = k_j \sqrt{1 - \sin^2 \theta_j}$$

$$= k_j \sqrt{1 - \frac{k_0^2}{k_j^2} \sin^2 \theta_0}.$$
(20)

At sufficiently low frequencies, that is, when the quasi-static approximation is valid, $k_0^2/k_j^2 = \omega^2 \mu_0 \epsilon_0/(\omega^2 \mu_0 \epsilon_j - i\omega \mu_0 \sigma_j) \rightarrow 0$ as $\omega \rightarrow 0$ and $k_{z,j} \cong k_j$. Hence, it is only in the quasi-static approximation or at vertical incidence that the EM field is transmitted vertically into the Earth. At high frequencies and oblique incidence, the angle of transmission generally deviates from 0°.

After solving the Helmholtz equations (eqs 13 and 14) for E_x or H_x of a 2-D conductivity distribution, the auxiliary fields H_y and H_z or E_{ν} and E_{z} can be computed with eqs (6) and (7) or eqs (9) and (10), respectively.

The off-diagonal elements of the complex 2-D impedance tensor relate the horizontal magnetic fields to the horizontal electric fields of the TE- and TM-mode as

$$\begin{bmatrix} E_x \\ E_y \end{bmatrix} = \begin{bmatrix} 0 & Z_{xy} \\ Z_{yx} & 0 \end{bmatrix} \begin{bmatrix} H_x \\ H_y \end{bmatrix}$$
and yield the responses commonly used in radiomagnetotellurics, that is, the apparent resistivities

$$\begin{bmatrix} 1 & 1 & 1 & 1 & 1 \\ 1 & 1 & 1 & 1 \end{bmatrix}$$
(21)

$$\rho_a^{xy} = \frac{1}{\omega \mu_0} |Z_{xy}|^2 \quad \text{and} \quad \rho_a^{yx} = \frac{1}{\omega \mu_0} |Z_{yx}|^2$$
(22)

$$\phi^{xy} = \arg(Z_{xy}) \quad \text{and} \quad \phi^{yx} = \arg(Z_{yx}). \tag{23}$$

Ward et al. (1968) establish a more direct link to the electrical properties of the subsurface, in the general case with displacement currents, by defining an apparent conductivity and an apparent dielectric permittivity.

Due to the dependence of the EM field on the angle of incidence, the amplitude and phase of the impedances of the TM- and TE-mode differ even if measured on the surface of a layered Earth. Only if the quasi-static approximation is valid or if the EM field is vertically incident, the TE- and TM-mode impedances of a layered half-space satisfy the relationship $Z_{xy} = -Z_{yx}$.

For plane waves vertically incident on the surface of a homogeneous half-space with impedivity \hat{z} and admittivity \hat{y} , the TM-mode impedance has the form $Z_{yx} = \sqrt{\hat{z}/\hat{y}}$ (Wait 1970; Ward & Hohmann 1987). In the quasi-static approximation, the latter expression simplifies to $Z_{yx} = \sqrt{i\omega\mu_0/\sigma}$, and only in this case, the apparent resistivities and phases measured on a homogeneous half-space equal the resistivity of the half-space and 45°, respectively.

In the TE-mode, the vertical magnetic field H_z is related to the horizontal magnetic field H_y through the complex 2-D VMT B:

$$H_z = B H_v. (24)$$

For plane waves obliquely incident on a layered Earth, the VMT generally differs from zero. However, for vertically incident plane waves or in the quasi-static approximation, a VMT that differs from zero is only observed if the admittivity \hat{y} varies laterally (see eqs 5–7).

2.2 Normal and oblique incidence

In the case of grazing or oblique incidence, both the incident electric and the incident magnetic fields can have vertical components (see Fig. 1). Already for a 1-D earth model, the TE- and TM-mode are then defined, by demanding that either the electric or the magnetic field be perpendicular to the plane of incidence (Wait 1970; Ward & Hohmann 1987), and the impedance tensor and VMT measured on the Earth's surface depend on the angle of incidence (see Section 2.1). It is therefore important to appraise the error made by assuming vertical incidence during the modelling process. For a layered earth model, the deviations of the TE- and TM-mode impedance amplitudes and phases at an arbitrary angle of incidence from those at normal incidence can be estimated with well-known recurrence formulae (see e.g. Wait 1953, 1970; Crossley 1981; Ward & Hohmann 1987; Song et al. 2002).

For the half-space model shown in Fig. 2(a), consisting of two layers with resistivities of 600 and 30 000 Ω m and layer thicknesses of 25 and 75 m, a confining half-space with a resistivity of 600Ω m and a constant relative permittivity $\epsilon_r = 6$, the deviations of the amplitude and phase of the TM- and TE-mode impedances from their respective values at normal incidence are shown in Fig. 2. The maximal deviations of 1.5 per cent and 1° for the amplitude and phase, respectively, occurring at parallel incidence, are of the order of typically expected error levels. A similar model that consists of the uppermost layer underlain by a confining half-space of 30 000 Ω m shows maximal deviations of 1.0 per cent and 0.25°, respectively, indicating that a considerable part of the distortion in the first case is due to the reflection of the EM energy on the top of the confining half-space.

The angle of incidence can be estimated with the scheme by Song et al. (2002), which requires that the horizontal EM field components are measured simultaneously at adjacent receiver sites. In a typical RMT field campaign, however, a single receiver is moved along the profile. The interpretation is further complicated, as the EM fields of different transmitters, with frequencies close to a nominal frequency, are used to estimate the TM- and TE-mode impedances (Bastani & Pedersen 2001). Generally, the transmitters are off the profile or strike direction and have different angles of incidence; but the angle of incidence, normally, is close to 90° (grazing incidence) at the site of investigation (Crossley 1981).

As the aerials employed by the remote radio transmitters, typically, are vertical electric dipoles, the incident EM field is that of a TM-mode. Hence, the definitions of TE- and TM-mode based on the geoelectrical structure of the subsurface and on the nature of the incident field are conciliable only for the TM-mode, given that the direction to the remote radio transmitter coincides with the profile direction (as in Fig. 1 for instance). If the transmitter was located off the profile direction, the wavenumber vector **k** would have an x-component, which, in the general case, would persist within the Earth and invalidate the 2-D assumption $\partial/\partial x = 0$. However, even this problem is amended if a

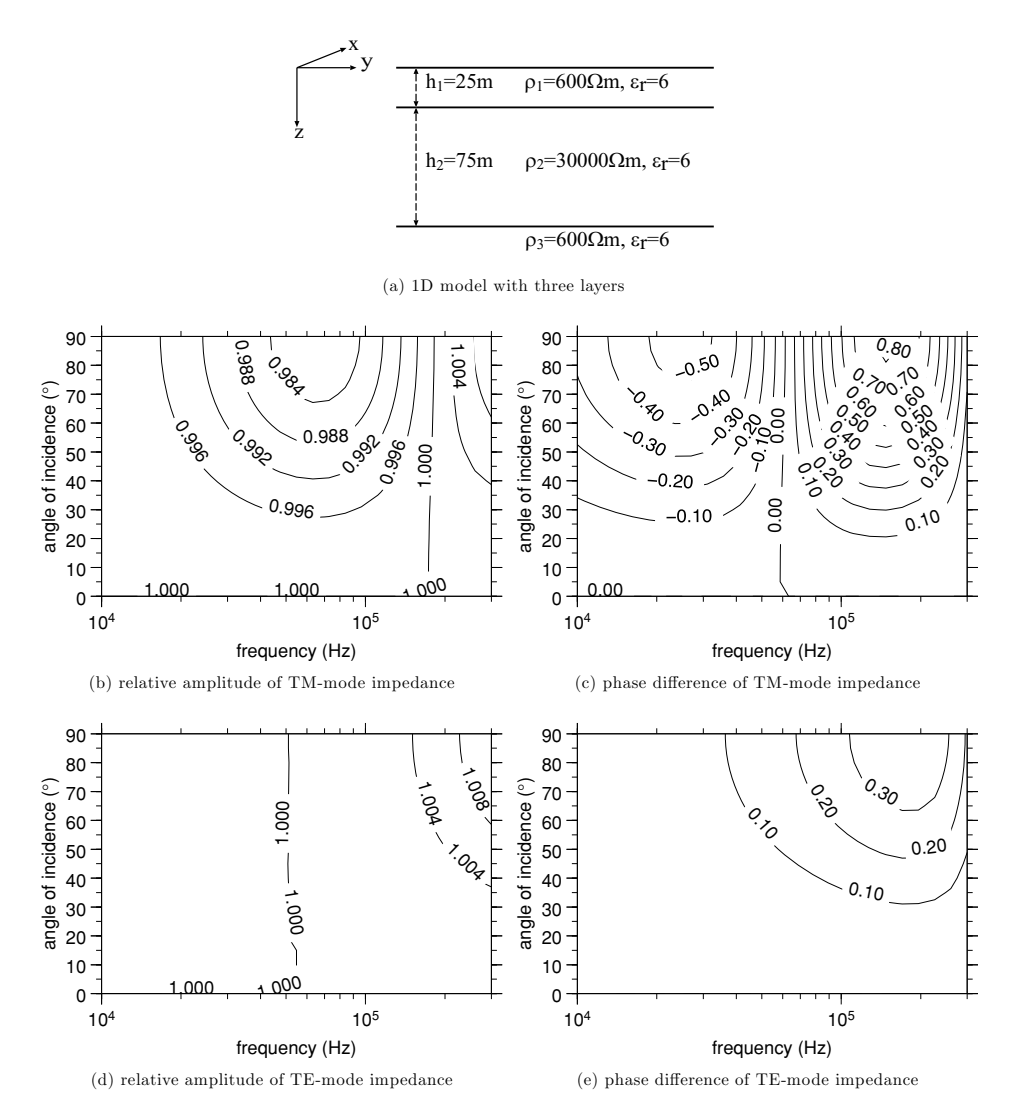


Figure 2. Relative amplitude and phase difference for the TM- and TE-mode impedances with respect to the case of normal incidence for angles of incidence between 0° (normal incidence) and 90° (grazing incidence) and at frequencies between 10 and 300 kHz (panels b–e). The earth is assumed to consist of two layers with resistivities of 600 and $30\,000\,\Omega$ m and layer thicknesses of 25 and 75 m, respectively, a confining half-space with a resistivity of $600\,\Omega$ m and a constant relative permittivity $\epsilon_{\rm r}=6$ (panel a). The deviations from the impedance values at normal incidence are largest at grazing incidence.

moderately resistive or conductive surface layer is present, as the EM field is then transmitted almost vertically into the subsurface, and the definition of different modes can be based on the geoelectrical structure.

We consider only vertically incident plane-wave fields. As the above example shows, the presence of a moderately resistive or conductive near-surface layer reduces the importance of the angle of incidence, and deviations of the responses for different angles of incidence are then rather small.

2.3 Computation of forward responses and sensitivities

The forward problem, that is, the computation of responses for a given model, is solved by discretizing the modelling domain with the finite-difference approximation (FDA), following Hohmann (1987) and Aprea *et al.* (1997). The derivations of the FDAs for the TE- and TM-modes can be found in Appendix A. Both direct and iterative solvers for the system of linear equations, arising from the FDA of the forward problem, are discussed in Appendix B. As we have not yet managed to implement an appropriate iterative solver, we rely on the LU-decomposition (also known as Gaussian elimination) by Anderson *et al.* (1999).

The sensitivity matrix $\mathbf{J} \in \mathbb{R}^{N*M}$ describes the perturbations ensuing for N forward responses $\mathbf{F}[\mathbf{m}] \in \mathbb{R}^N$ due to perturbations of M model parameters $\mathbf{m} \in \mathbb{R}^M$. The entry of the sensitivity matrix for the kth datum with respect to the lth model parameter is then calculated as a partial derivative:

$$J^{kl}(\mathbf{m}) = \frac{\partial \mathbf{F}^k[\mathbf{m}]}{\partial m^l}.$$
 (25)

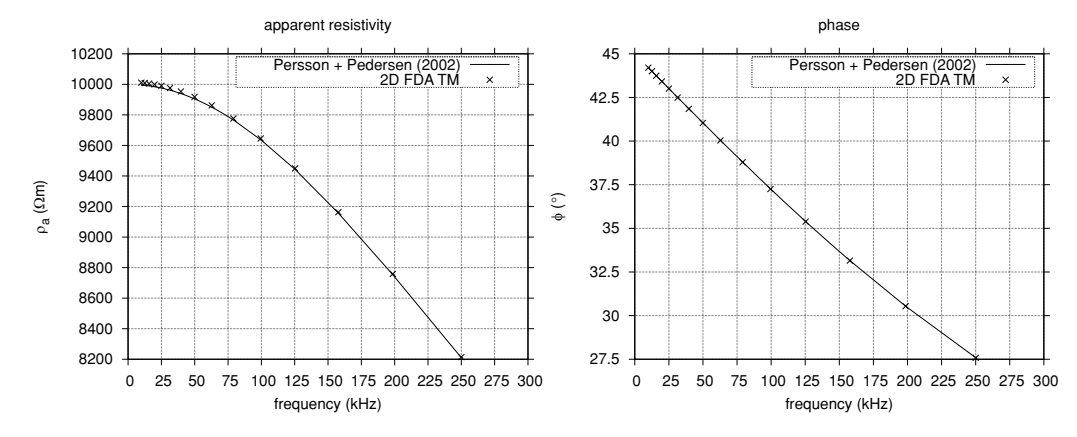


Figure 3. Analytic 1-D solutions by Persson & Pedersen (2002) and 2-D FDA solutions of apparent resistivity ρ_a and phase ϕ for the TM-mode on the surface of a homogeneous half-space with $\rho=10\,000\,\Omega$ m and $\epsilon_r=5$. The responses were computed for frequencies between 10 and 250 kHz and under the assumption of normal incidence. At high frequencies, ρ_a and ϕ are both significantly smaller than their quasi-static values of 10 000 Ω m and 45 °, respectively. With decreasing frequency, ρ_a and ϕ approach their quasi-static values asymptotically.

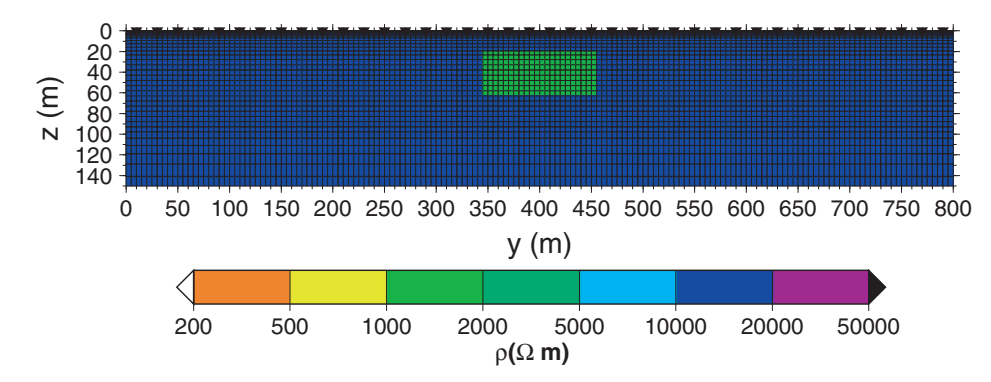


Figure 4. Simple 2-D model with a conductive block of $\rho = 1000 \,\Omega$ m in a half-space with a resistivity of $\rho = 10\,000 \,\Omega$ m and constant relative dielectric permittivity $\epsilon_{\rm r} = 5$. Receiver positions are indicated by black triangles. The TM-mode, TE-mode and VMT responses of this model are shown in Fig. 5.

The entries of the sensitivity matrix are typically given for the logarithms of the apparent resistivities and the phases of the impedance tensor elements and the real and imaginary parts of the VMT with respect to the logarithms of the cell resistivities. The logarithms are typically chosen relative to the base 10. The sensitivity matrix is computed with the scheme by Rodi (1976) and depends on the FDA of the forward problem. Further information on this algorithm is given in Appendix C. An example of sensitivity matrix entries is given at the end of Section 3.2.

2.4 Mesh design

To obtain accurate modelling results, the total extent of the modelling domain (i.e. the finite-difference mesh) and the sizes of individual cells of the finite-difference mesh need to be well adapted to the settings of the experiment, that is, the length of the profile on which measurements were conducted, the lowest and highest frequencies of the measurements and the distributions of electrical conductivity and dielectric permittivity present in the model.

The horizontal and, below the air–Earth interface, the vertical extents of the finite difference mesh must be larger than those used in the quasi-static approximation, as the skin depth $\delta = \frac{1}{\beta}$ computed with displacement currents (see eq. 18) is larger than its quasi-static counterpart.

Furthermore, the node spacing must be small compared with the scale lengths across which the EM fields vary, that is, the inverse real and imaginary parts of the complex wavenumber k. In the quasi-static approximation, this leads to the well-known requirement that the node spacing must be small compared with the local skin depth (Aprea *et al.* 1997). In the general case, $1/\alpha < 1/\beta$ and the local node spacing must be considerably smaller than $1/\alpha$.

A small vertical node spacing is essentially important for the air half-space since the vertically incident plane wavefield propagates undamped (assuming $\sigma_{air} = 0 \text{ S m}^{-1}$). In the air, the largest vertical mesh cell dimension must be smaller than $1/\alpha$ of the highest frequency. This results in the following comparison. In the REBOCC inverse scheme (Siripunvaraporn & Egbert 2000), the conductivity of the air half-space is assumed to be $\sigma_{air} = 10^{-10} \text{ S m}^{-1}$, and the quasi-static skin depth at a frequency of 300 kHz is 92 km. In the general case with displacement currents, $\sigma_{air} = 0 \text{ S m}^{-1}$ and the inverse real part of the wavenumber is $1/\alpha = 159 \text{ m}$ for f = 300 kHz. In the former case, the

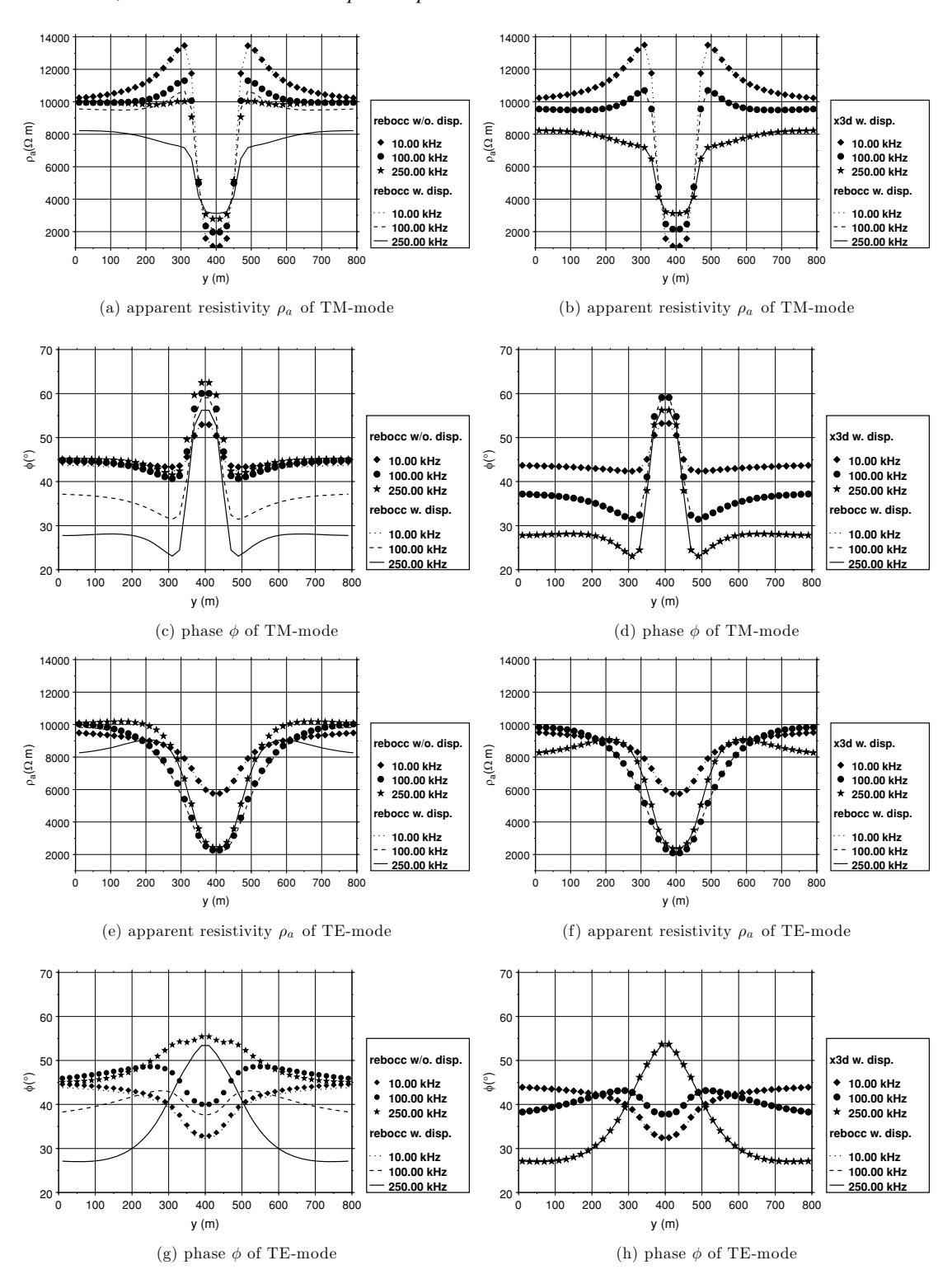


Figure 5. Comparison of 2-D FDA forward responses of the block model shown in Fig. 4 computed with displacement currents (shown as lines in both the left- and right-hand columns) with 2-D FDA solutions computed in the quasi-static approximation (shown as symbols in the left-hand column) and 3-D integral equation solutions computed with displacement currents (shown as symbols in the right-hand column). Panels (a)—(d) show the responses for the TM-mode apparent resistivity and phase, respectively. Panels (i)—(l) show the responses for the TE-mode apparent resistivity and phase, respectively. Panels (i)—(l) show the responses for the real and imaginary part of the VMT, respectively. The TM-mode and TE-mode responses computed with displacement are generally smaller than those computed in the quasi-static approximation, especially to the sides of the conductive block. The real part of the VMT response computed with displacement currents shows distinct sign reversals [marked by labels (2) and (6) in panel i] to the sides of the conductive block. The corresponding maximum and minimum are marked by labels (1) and (7), respectively, in panel (i). The 2-D FDA and integral equation solutions are in good agreement (right-hand column).

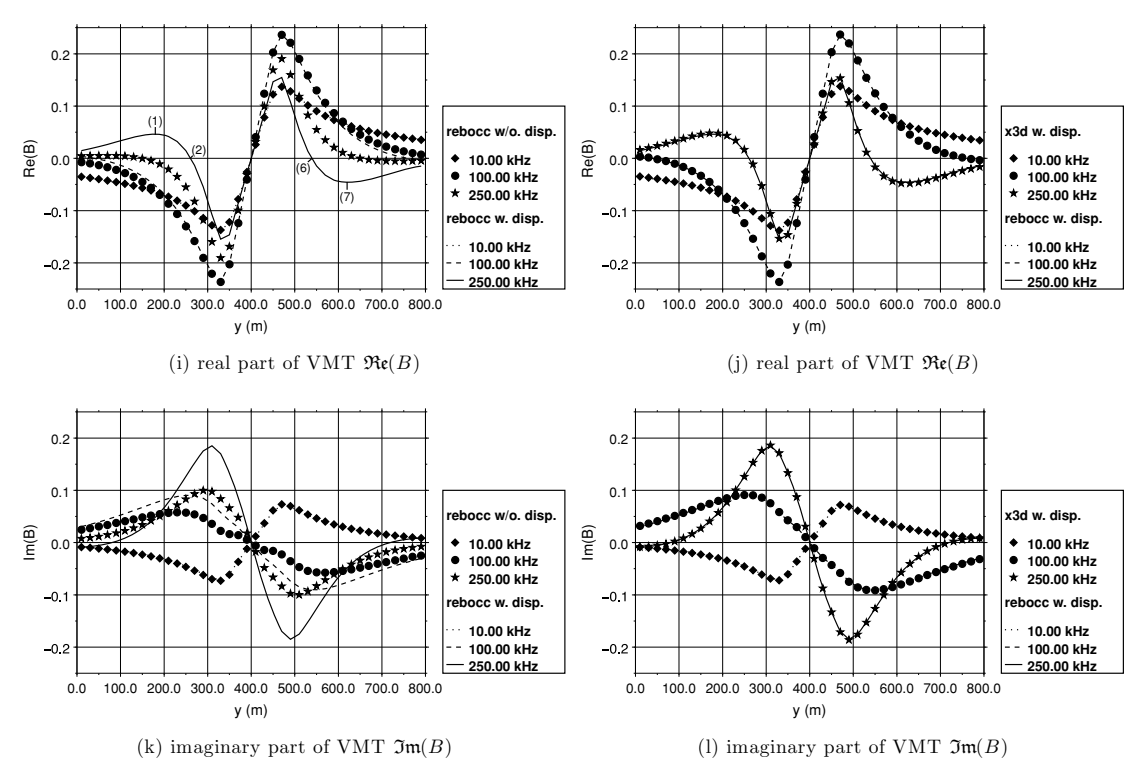


Figure 5. (Continued.)

skin depth exceeds the size of the modelling domain by far, and it is therefore appropriate to address the primary field of the quasi-static case as a uniform inducing field rather than a plane wave incident on the Earth's surface.

3 SYNTHETIC EXAMPLES

3.1 Forward modelling examples

We consider a forward modelling example for a homogeneous half-space, with a resistivity of $10\,000\,\Omega$ m and a relative permittivity $\epsilon_r = 5$. Assuming vertically incident plane waves, analytic 1-D solutions with the algorithm by Persson & Pedersen (2002) and 2-D FDA solutions were computed for the apparent resistivities and phases of the TM- (Fig. 3) and TE-mode (not shown) at frequencies between 10 and 250 kHz. The comparison of the analytic 1-D solution (marked by a solid line) and the 2-D FDA solution (marked by crosses) shows excellent agreement. At high frequencies, the effect of displacement currents is to decrease the apparent resistivity and phase below the apparent resistivity of $10\,000\,\Omega$ m and phase of 45° , respectively, typical of the quasi-static approximation. For a typical error level of 2 per cent on the impedance, the deviations from the quasi-static values are as large as the given errors at $105\,\text{kHz}$ for the apparent resistivity and $15\,\text{kHz}$ for the phase.

For the simple 2-D model with a block of $\rho=1000\,\Omega$ m in a half-space, with a resistivity of $\rho=10\,000\,\Omega$ m and $\epsilon_{\rm r}=5$ throughout, shown in Fig. 4, 2-D FDA forward responses with displacement currents are compared with both 2-D FDA forward responses for the quasi-static approximation and the 3-D integral equation solution by Avdeev *et al.* (2002). Responses were computed for the TM-mode impedance, the TE-mode impedance and the VMT. Fig. 5 shows the 2-D FDA forward responses, computed with and without displacement currents in the left-hand column, and the comparison of 2-D FDA forward responses, computed with displacement currents, and 3-D integral equation solutions, with displacement currents, in the right-hand column. The latter comparison indicates that the finite-difference forward scheme is rather accurate. For the given mesh discretization, the relative deviations between the impedance responses of the FDA and integral equation solutions are below 3.0 per cent. The absolute deviations between the VMT responses of the FDA and integral equation solutions are below 0.003. As errors in the computation of two field components might cancel when taking their ratio, a further comparison was done for the 2-D FDA and 3-D integral equation solutions of individual field components (not shown). After an appropriate normalization, the scaled complex field components of the TE-mode deviate by less than 0.7 per cent, whereas the field components of the TM-mode differ by as much as 3.0 per cent. As we do not have insight into the code by Avdeev *et al.* (2002), it is difficult to give an explanation for the discordance in the latter case.

For the lowest frequency of about 10 kHz, the responses computed with (dotted lines in left-hand column of Fig. 5) and without displacement currents (diamond symbols in left-hand column of Fig. 5) are very similar. At 100 kHz (dashed lines and filled circle symbols)

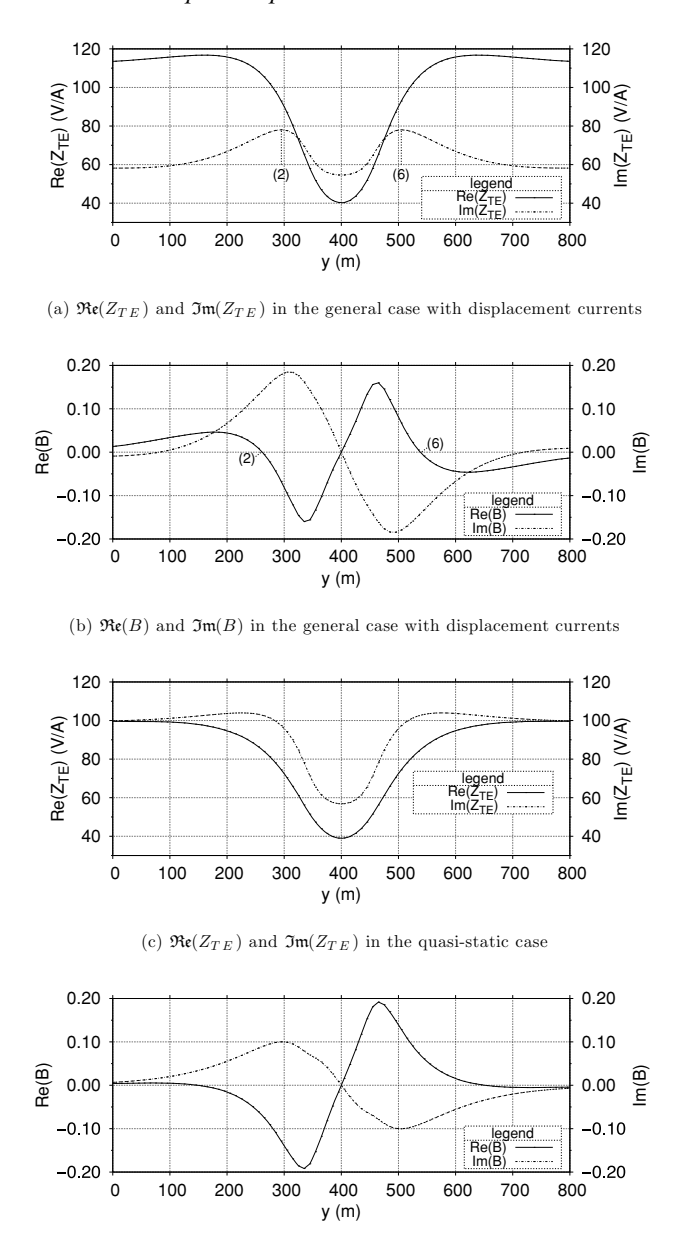


Figure 6. The TE-mode impedance Z_{TE} and the VMT B for the model shown in Fig. 4 at $f=250\,\text{kHz}$, in the general case with displacement currents (panels a and b) and the quasi-static case (panels c and d). The VMT and the TE-mode impedance roughly follow the relations $\Re e(\frac{H_z}{H_y}) \propto \Im m(\frac{\partial Z_{xy}}{\partial y})$ and $\Im m(\frac{H_z}{H_y}) \propto -\Re e(\frac{\partial Z_{xy}}{\partial y})$. Hence, for instance, zero transitions of the real part of the VMT are observed at approximately the same positions where the imaginary part of the impedance has minima or maxima. The labels (2) and (6) mark two such pairs of zero transitions in the real part of the VMT and maxima of the imaginary part of the impedance.

(d) $\mathfrak{Re}(B)$ and $\mathfrak{Im}(B)$ in the quasi-static case

and 250 kHz (solid lines and star symbols), the influence of displacement currents is considerable, given the chosen resistivity distribution and relative dielectric permittivity.

For stations located on the sides of the conductive block, the effect of displacement currents on TE- and TM-mode impedances is most obvious. Towards the left- and right-hand edges of the mesh, the apparent resistivities and phases approach those of the corresponding homogeneous half-space (see Fig. 3). Also at sites above the conductive block, apparent resistivity and phase are generally smaller than in the quasi-static approximation.

An important effect of displacement currents on the real and imaginary parts of the VMT at high frequencies is the occurrence of lateral sign reversals, located symmetrically around the conductive block. For $f = 250 \,\text{kHz}$, lateral sign reversals are shown at 260 and 540 m along the profile in the real part of the VMT [marked by labels (2) and (6), respectively, on the solid line in Fig. 5i] and at 75 and 725 m along

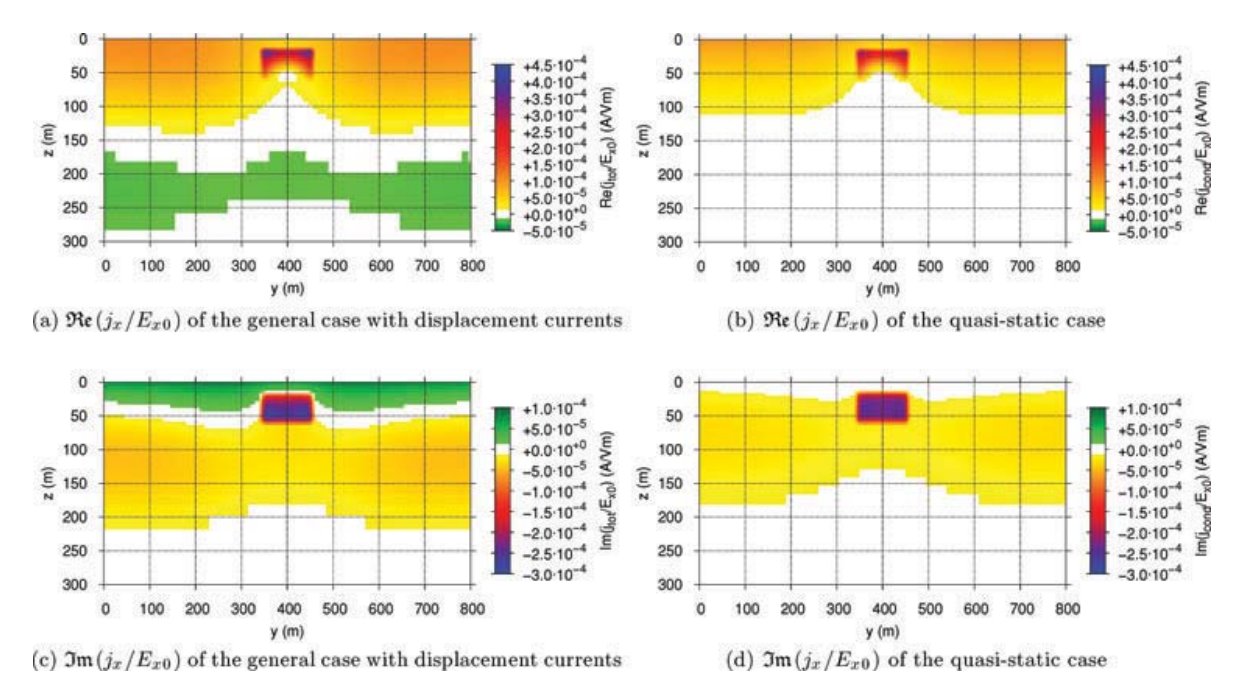


Figure 7. Real (upper row) and imaginary (lower row) parts of the normalized current density j_x/E_{x0} at $f=250\,\mathrm{kHz}$ of the TE-mode for the general case with displacement currents (left-hand column) and the quasi-static case (right-hand column) for the model shown in Fig. 4. Normalized current densities, which are close to $0\,\mathrm{A\,V^{-1}\,m^{-1}}$, are plotted in white. Different colourscales were used for the real and imaginary parts. In the general case with displacement currents, the current system penetrates deeper into the subsurface than in the quasi-static case.

the profile in the imaginary part of the VMT (solid line in Fig. 5k). In addition to the lateral sign reversals, the real part of the VMT has a maximum at y = 180 m [marked by label (1) in Fig. 5i] and a minimum at y = 620 m [marked by label (7) in Fig. 5i]. The responses at the maximum and minimum are $|\Re e(B)| = 0.05$. Sign reversals to the sides of the conductive block can also be observed in the real part of the quasi-static response at y = 150 m and y = 650 m (star symbols in Fig. 5i). However, the quasi-static response is comparatively small at sites further away from the block (no larger than $|\Re e(B)| = 0.006$) and would most likely be masked by noise effects (a typical absolute error is e.g. $\Delta \Re e(B) \approx 0.01$) if measured in the field. In the general case with displacement currents, the deduction of the horizontal centre of conductive structures from the positions of zero transitions of the VMT B becomes intricate in more complex geological settings. Artefacts might be introduced to inverse models in a quasi-static interpretation.

It is instructive to relate the lateral sign reversals of the VMT to the gradient of the TE-mode impedance Z_{xy} by considering eqs (7) and (21):

$$\hat{z}H_z = \frac{\partial E_x}{\partial y} = \frac{\partial}{\partial y}(Z_{xy}H_y).$$

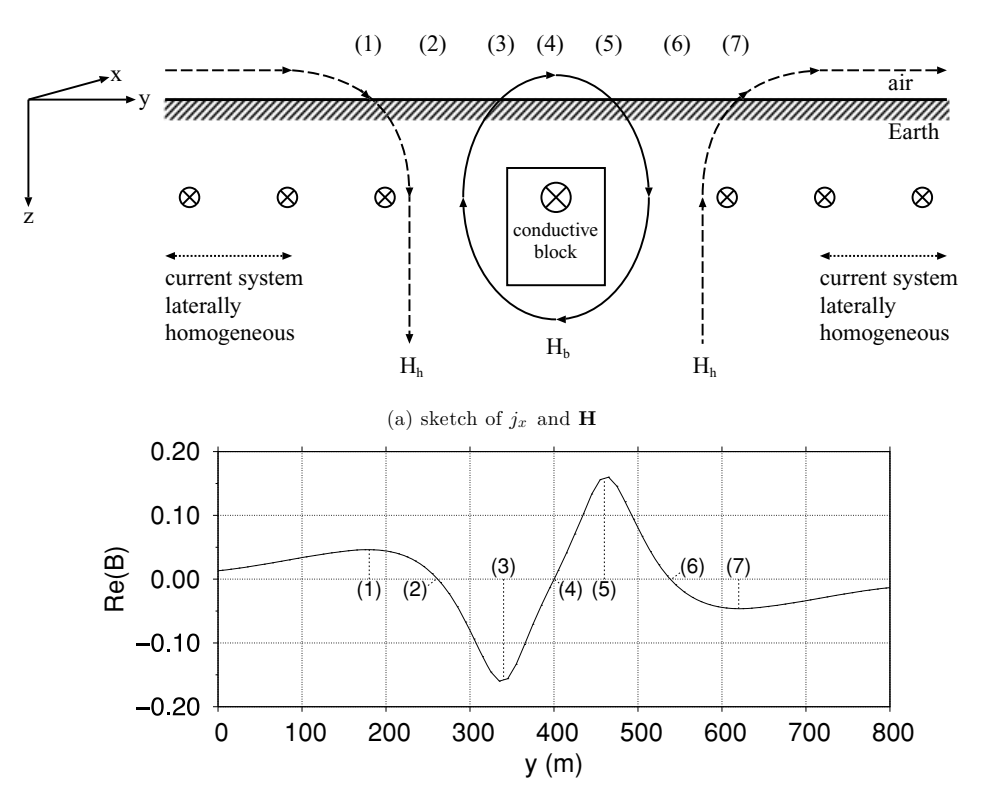
For small deviations of H_y from its normal field component H_y^n , that is, the H_y -component of the corresponding 1-D model without the conductive block, this yields

$$\frac{H_z}{H_y} \approx \frac{H_z}{H_y^n} = \frac{1}{\hat{z}} \frac{\partial Z_{xy}}{\partial y} = -\frac{i}{\omega \mu_0} \frac{\partial Z_{xy}}{\partial y},\tag{26}$$

which corresponds to the following relationships for the real and imaginary parts of the VMT

$$\begin{split} \Re e\left(\frac{H_z}{H_y}\right) & \propto -\mathbf{i}\cdot\mathbf{i}\cdot\Im m\left(\frac{\partial Z_{xy}}{\partial y}\right) = \Im m\left(\frac{\partial Z_{xy}}{\partial y}\right).\\ \Im m\left(\frac{H_z}{H_y}\right) & \propto -\Re e\left(\frac{\partial Z_{xy}}{\partial y}\right). \end{split}$$

In the synthetic example for $f = 250 \, \text{kHz}$, the variation of H_y away from its approximate 1-D values at the beginning and end of the profile is less than 22 per cent in the quasi-static case (not shown) and less than 12 per cent in the general case (not shown). The real and imaginary parts of the VMT are in good agreement with the expected variation with the lateral derivative of the TE-mode impedance Z_{xy} for the quasi-static (Figs 6c and d) and general cases (Figs 6a and b). For the general case, the positions of the lateral sign reversals in the real part of the VMT and the corresponding maxima in the imaginary part of the impedance are marked with the labels (2) and (6) in Figs 6(b) and (a), respectively. The zero transitions of the VMT are somewhat shifted from their predicted positions, where impedance maxima are less distinct. This disagreement is related to the fact that the assumption of small deviations of H_y from its normal component is slightly violated.



(b) $\mathfrak{Re}(B)$ of the general case with displacement currents

Figure 8. A sketch of the real part of the current density j_x in the subsurface with the emerging real part of the magnetic field \mathbf{H} (panel a) and the real part of the VMT response for the model shown in Fig. 4, at $f=250\,\mathrm{kHz}$ in the general case with displacement currents (panel b). At positions (1) and (7), the magnetic field \mathbf{H}_b due to currents in the resistive host is larger than the magnetic field \mathbf{H}_b due to currents in the conductive block, leading to a maximum and a minimum of the real part of the VMT at (1) and (7), respectively. In the vicinity of the conductive block, the magnetic field is dominated by \mathbf{H}_b resulting in a minimum and a maximum of the real part of the VMT at (3) and (5), respectively. At positions (2) and (6), the vertical components of \mathbf{H}_b and \mathbf{H}_b are equal in magnitude but opposite in direction and, hence, the VMT B is zero. The lateral position of the sign reversal at (4) coincides with the centre of the conductive block.

A more quantitative explanation for the lateral zero transitions can be arrived at by investigating eq. (5). As the curl operator treats the real and imaginary parts of **H** separately,

$$\frac{\partial \Re e(H_z)}{\partial y} - \frac{\partial \Re e(H_y)}{\partial z} = \Re e(\hat{y}E_x) \quad \text{and} \quad \\ \frac{\partial \Im m(H_z)}{\partial y} - \frac{\partial \Im m(H_y)}{\partial z} = \Im m(\hat{y}E_x)$$

are directly related to the real and imaginary parts of the current density $j_x = \hat{y}E_x$ of the TE-mode. However, the current densities of the quasi-static and general cases in the subsurface are not directly comparable. As the propagation of the electric field in the air is modelled differently (i.e. through conduction currents in the quasi-static approximation with a conductivity $\sigma_{air} = 10^{-10} \text{ Sm}^{-1}$ and through displacement currents in the general case), there is a large difference in the scale lengths over which the electric field varies in the air (see Section 2.4). This leads to different phases and amplitudes of the electric fields of the two cases at the air–Earth interface, even if equal amplitudes and phases of the electric field are chosen as boundary conditions on the upper edge of the finite-difference mesh. In addition, different vertical node spacings were chosen in the air half-space for the quasi-static and general cases, according to the considerations in Section 2.4. To circumvent this problem, the electric field is scaled by its surface value at the left-hand edge of the mesh.

For the general case, the real and imaginary parts of the normalized current density at $f = 250 \,\mathrm{kHz}$ are shown in Figs 7(a) and (c), respectively. Similarly, for the quasi-static case, the real and imaginary parts of the normalized current density at $f = 250 \,\mathrm{kHz}$ are shown in Figs 7(b) and (d), respectively. The area of the highest normalized current density amplitude (up to $5.7 \times 10^{-4} \,\mathrm{A\,V^{-1}\,m^{-1}}$) coincides with the conductive block. To the sides of the block at $y < 340 \,\mathrm{m}$ and $y > 460 \,\mathrm{m}$, the normalized current density amplitude reaches $1.8 \times 10^{-4} \,\mathrm{A\,V^{-1}\,m^{-1}}$, with only small lateral changes of the real and imaginary parts at the beginning and end of the profile.

An important simplification ensues for the real part of the VMT of the general case, as $\Re(H_y)$ exceeds $\Im(H_y)$ by at least a factor 4.4 at all positions along the profile (not shown). Hence, the real part of the VMT can be approximated as $\Re(B) \approx \Re(H_z)/\Re(H_y)$ and is mostly determined by $\Re(j_x)$ in Fig. 7(a). We illustrate the sign reversals in the real part of the VMT for the general case with a sketch (Fig. 8a) that describes the real part of the current system in the subsurface and the emerging magnetic field. The real part of the magnetic

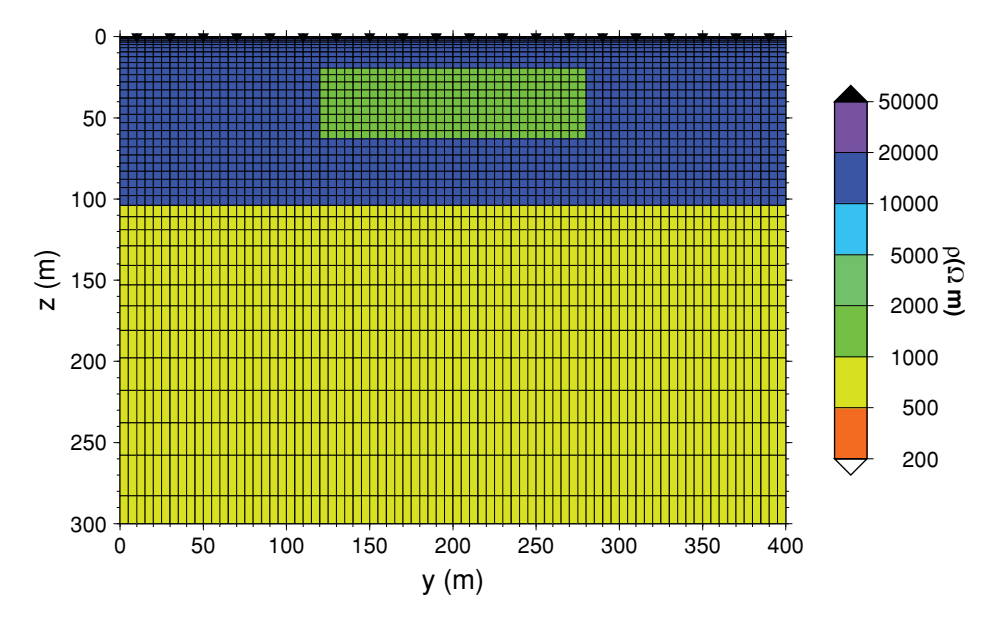


Figure 9. Simple 2-D model with a buried elongated block of a resistivity of $1000 \,\Omega$ m in a resistive layer of $10\,000 \,\Omega$ m and underlain by a half-space of $500 \,\Omega$ m. The relative dielectric permittivity is assumed to be $\epsilon_{\rm r} = 5$. Receiver positions are indicated by black triangles.

field due to currents in the resistive host is designated as \mathbf{H}_{h} and the part due to currents in the conductive block is designated as \mathbf{H}_{b} (Fig. 8a). To facilitate a simpler comparison, the real part of the VMT for the general case (solid line in Fig. 5i) is plotted in Fig. 8(b). At the beginning and end of the profile [i.e. to the left-hand side of position (1) and to the right-hand side of position (7) in Fig. 8], the lateral homogeneity of the current system generates a magnetic field with a very small H_z -component. At positions (1) and (7), that is, at y = 180 and 620 m, the magnetic field \mathbf{H}_h due to the resistive host is larger than the magnetic field \mathbf{H}_h due to the conductive block, leading to a maximum and a minimum of the real part of the VMT at (1) and (7), respectively. At positions (2) and (6) to the sides of the block, that is, at y =260 and 540 m, the H_z -components of \mathbf{H}_h and \mathbf{H}_b are equal in amplitude but point in opposite directions, leading to zero-transitions of the real part of the VMT. The minimum, zero transition and maximum of the real VMT response at positions (3), (4) and (5), respectively, are similar in both the quasi-static and general cases (see Fig. 5i). Though in magnitude smaller than the current system in the block, the lateral current system is strong enough to generate a commensurable maximum and minimum of the real part of the VMT at y = 180 and 620 m, respectively (Fig. 8b). Hence, the main effect of displacement currents on the real part of the VMT is to increase the response at the edges of the conductor. As noted before, there are no such distinct maxima or minima associated with the lateral sign reversals in the quasi-static VMT response at $f = 250 \,\text{kHz}$ (star symbols in Fig. 5i). The reason is most likely that the vertical extent of the current systems and the total current strengths to the sides of the block (Figs 7b and d) are smaller than in the general case with displacement currents (Figs 7a and c), whereas the current within the conductive block has a comparable amplitude in both cases. It should also be noted that the imaginary part of the VMT increases quite strongly in amplitude if displacement currents are included (Fig. 5k). An explanation with regard to the imaginary part of the current density (shown in Fig. 7c) does not appear to be possible as the imaginary part of H_z and the real part of H_y are involved.

3.2 Inverse modelling examples

Synthetic responses of a simple 2-D model (Fig. 9), with constant relative dielectric permittivity $\epsilon_r = 5$ and an elongated block with a resistivity of $1000\,\Omega$ m that is buried in a resistive layer of $10\,000\,\Omega$ m and underlain by a half-space of $500\,\Omega$ m, were computed for the TM-and the TE-mode. The responses were computed at 20 receiver sites for 15 frequencies, ranging from 10 to 250 kHz giving a total of 600 data points. Gaussian white noise, corresponding to 2.5 per cent of the modulus of the computed impedances, was added to the forward responses of both polarizations.

After that, two inversions of the synthetic data set were performed with the REBOCC inverse scheme (Siripunvaraporn & Egbert 2000). During the first inversion, displacement currents were allowed for, whereas they were neglected during the second inversion. In both inversions, the error floor was assumed to correspond to 2.5 per cent of the modulus of the impedances, and the starting model was a homogeneous half-space of $10\,000\,\Omega\,m$.

After six iterations with the inversion that allows for displacement currents, a model was obtained (Fig. 10), which fits the data to a rms misfit of 1.04. Additional iterations with REBOCC did not decrease the rms misfit further. The inverse model reproduces the edges of the block and the resistivities of the block and layered half-space rather accurately. The transition from the lower edge of the conductor into the resistive layer is, however, smeared out.

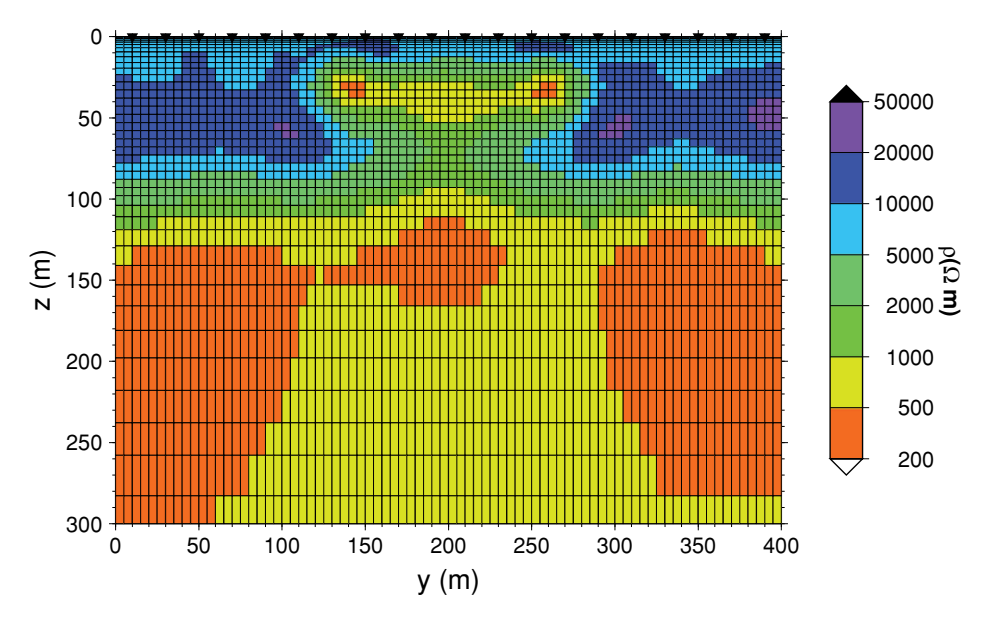


Figure 10. 2-D REBOCC inversion result of synthetic data from the 2-D block model in Fig. 9. Displacement currents were allowed for during the inversion. After six iterations, a rms misfit of 1.04 was reached. The inverse process has reconstructed the edges of the conductive block and the resistivities of the block and layered half-space rather accurately. The lower edge of the conductor is smeared out due to the damping of the electromagnetic field in the block.

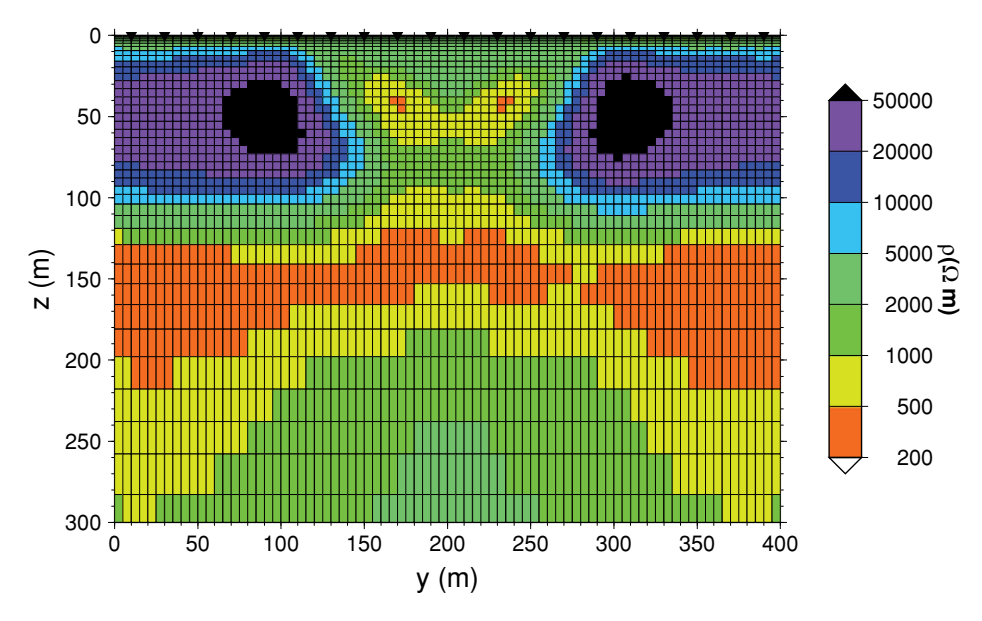


Figure 11. 2-D REBOCC inversion result of synthetic data from the 2-D block model in Fig. 9. Displacement currents were not allowed for during the inversion. After four iterations, the lowest rms misfit of 1.95 was reached. Artefactual structures in the form of a conductive near-surface layer, two resistors at the sides of the conductive block, a distorted shape of the block and a too large depth to the top of the confining half-space are consequences of the omission of displacement currents during the inversion.

Neglecting displacement currents results in convergence problems and an inverse model with many artefactual structures (Fig. 11). The lowest rms misfit of 1.95 was obtained after four iterations. Clearly, an artefactual thin conductive layer is visible at the surface (a similar conductive layer is also observed by Persson & Pedersen (2002) in 1-D inverse models, computed in the quasi-static approximation, for synthetic data of a homogeneous half-space). The lateral extent of the conductive block and the top of the central parts of the block are grossly in error. Two artefactual resistors with resistivities close to $100\,000\,\Omega$ m appear to the left- and right-hand side of the block. The depth to the top of the underlying conductive layer is shifted from 105 to 130 m. If the synthetic data were generated from a model without the underlying conductive layer, the artefactual resistors would be observed, both to the sides of and below the conductive block (not shown).

A comparison of the relative errors, that is, the differences between the synthetic data and the forward responses scaled by the data errors, generated by the two inverse schemes, is shown in Fig. 12. The relative errors from the inversion that accounts for displacement currents

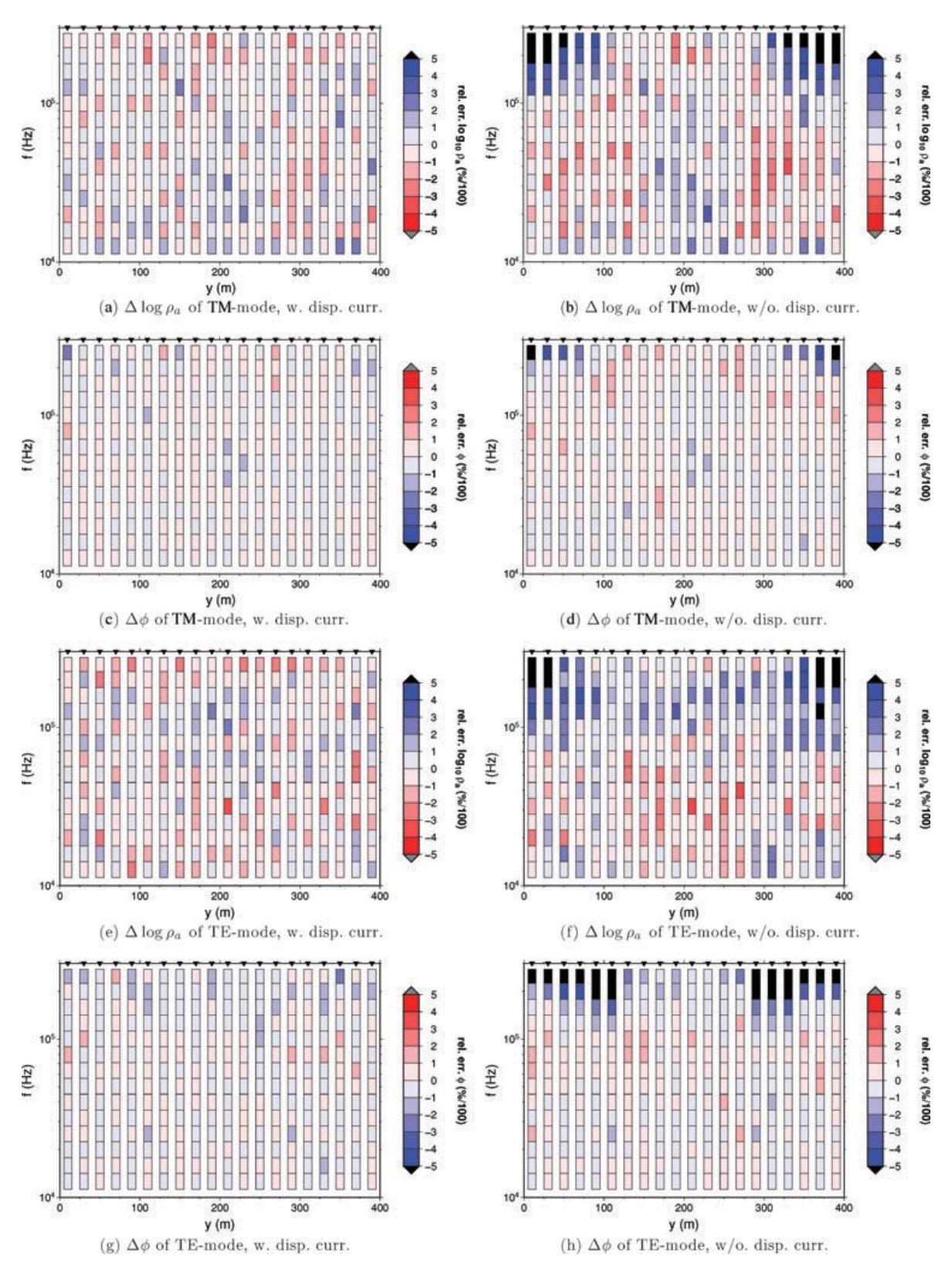
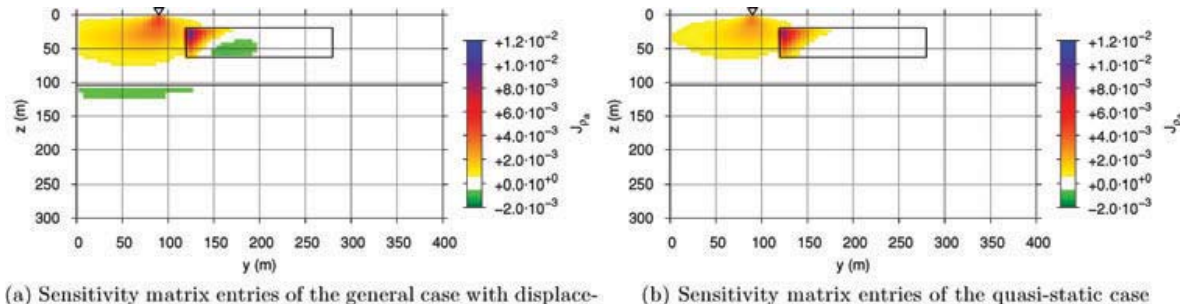


Figure 12. Relative errors obtained from the inversions of the synthetic data of the model shown in Fig. 9. The relative errors from inversions that account for displacement currents and that neglect displacement currents are shown in the left- and right-hand columns, respectively. The relative errors of $\log_{10} \rho_a$ and ϕ for the TM-mode are shown in panels (a)–(d), whereas the relative errors of $\log_{10} \rho_a$ and ϕ for the TE-mode are shown in panels (e)–(h). Systematic deviations from the synthetic data are mostly observed at high frequencies and stations to the sides of the conductive block for the model from the inverse scheme that does not allow for displacement currents (Fig. 11).



(b) Sensitivity matrix entries of the quasi-static case

ment currents

Figure 13. Sensitivity matrix entries for the block model in Fig. 9 and the TE-mode apparent resistivity at $f = 250 \, \text{kHz}$ and a receiver site at $y = 90 \, \text{m}$ (to the left-hand side of the conductive block). The receiver site is marked by a triangle. The edges of the conductive block and the interface between the upper layer and the confining half-space are depicted as solid black lines. Sensitivity values, which are close to 0, are plotted in white. As expected, sensitivities are largest at the left-hand upper edge of the conductive block and the sensitivity entries of the general case (panel a) encompass a larger volume with non-zero values (observe the negative sensitivity values marked in green) than those calculated in the quasi-static approximation (panel b).

(left-hand column of Fig. 12) show relatively random deviations of the forward data from the synthetic data. In contrast to this, the relative errors from the quasi-static inversion (right-hand column of Fig. 12) exhibit systematic deviations in the form of frequency ranges common to groups of neighbouring stations, with relative errors that have absolute values significantly larger than one and the same sign. The systematic deviations originate from the false assumption that displacement currents can be neglected during the inversion. As expected, the misfit is most severe at high frequencies and receiver sites to the sides of the conductive block.

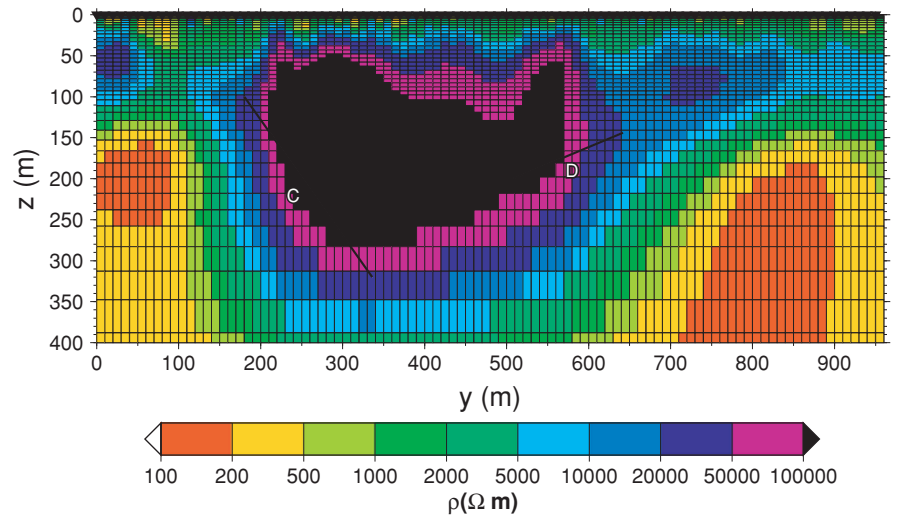
As an example, the row of the sensitivity matrix for the block model in Fig. 9 and the TE-mode apparent resistivity at $f = 250 \, \text{kHz}$ and a receiver site at y = 90 m (to the left-hand side of the conductive block) is shown in Fig. 13. Model parameters with sensitivities close to zero (shown in white colours in Fig. 13) have little influence on the considered data item. As expected, sensitivities, which were computed for the general case (Fig. 13a), encompass a larger volume with non-zero values than those computed in the quasi-static approximation (Fig. 13b). Especially, the depth extend for the non-zero sensitivity values of the general case is larger. This larger depth range is equivalent to a larger depth of investigation for the general case as already indicated in Section 2.4.

4 A FIELD DATA EXAMPLE

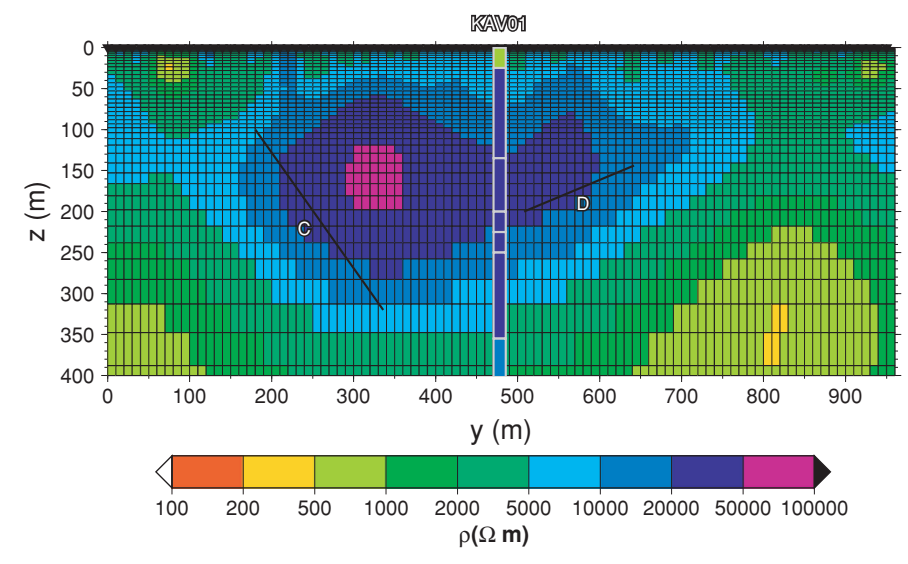
Linde & Pedersen (2004) investigate highly resistive granitic bedrock on the small island Ävrö, Sweden, with tensor RMT, in the frequency range of 14–226 kHz. RMT data were acquired on an east-west profile, with a total length of 960 m and a station spacing of 10 m. On Ävrö, the typical soil thickness is between 0 and 1 m. The bedrock consists mostly of granite. In some locations, aplitic and pegmatitic dykes are encountered (Gentzschein et al. 1987). Previous geophysical studies include borehole measurements by Gentzschein et al. (1987) and a seismic reflection study on the same profile by Juhlin & Palm (1999). A normal-resistivity log and a fracture frequency log of borehole KAV01, located in the central part of the profile, reveal an upper weathered layer, with a thickness of up to 30 m and a resistivity of about $600 \,\Omega$ m, followed by almost intact and highly resistive bedrock down to a depth of 200 m and with a resistivity between 32 000 and 40 000 Ω m (Gentzschein et al. 1987). Between 200 and 400 m depth, the resistivity slowly decreases to $10\,000\,\Omega$ m. At greater depth, the bedrock is more fractured and saline pore fluids decrease the electrical resistivity to a few thousand Ω m. Juhlin & Palm (1999) describe two major seismic reflectors (see Fig. 14d) for the depth range down to 400 m. Reflector C is located beneath the western part of the profile, at a depth between 100 and 320 m and dips approximately 60° to the east. Reflector D is located beneath the central part of the profile at a depth between 150 and 200 m and dips approximately 20° to the west.

To mitigate the effects of displacement currents, Linde & Pedersen (2004) restrict the data set used in quasi-static 2-D inversions with the REBOCC scheme (Siripunvaraporn & Egbert 2000) to frequencies up to 56 kHz. Linde & Pedersen (2004) perform inversions for the TE-mode, TM-mode, TE- and TM-modes together and the determinant of the impedance tensor. By computing synthetic TE-mode, TM-mode and determinant data for a 3-D model and comparing the corresponding 2-D inversions, Pedersen & Engels (2005) show that the inversion of determinant data is less prone to introducing artefacts from 3-D structures off the profile to 2-D inverse models. Furthermore, the inverse model of the determinant data, presented by Pedersen & Engels (2005) has a better data fit than their other models. For the inversion of the RMT data from Ävrö, this leads us to concentrate on the inversion of determinant data, as the data at both ends of the profile show a high degree of three-dimensionality (Linde & Pedersen 2004). At a few stations, the determinant data of the highest frequencies (160 and 226 kHz) have very small negative phases, which can be indicative of displacement currents (Song et al. 2002). As the rather irregular behaviour of the apparent resistivities at the same stations and frequencies hints at problems with measurement accuracy, we excluded such data points from the inversion.

In the following, we examine the effect of displacement currents, by first considering the inversion of the restricted set of frequencies and then for the full set of frequencies. For each data set, inversions were carried out in both the quasi-static approximation and with displacement



(a) model QL for the low-frequency data set and the quasi-static case



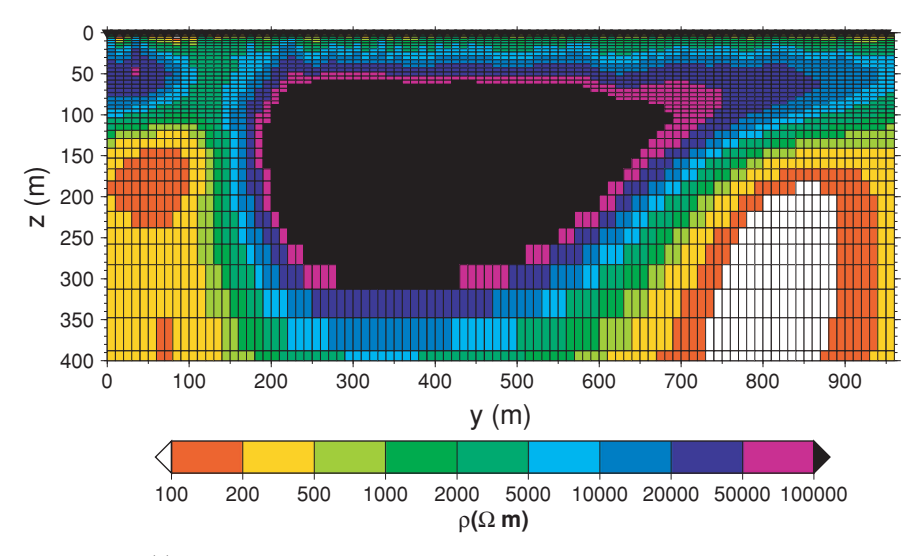
(b) model DL for the low-frequency data set and the general case with displacement currents

Figure 14. Models of the inversion of determinant data from Ävrö for (a) the low-frequency data set in the quasi-static approximation (model QL), (b) the low-frequency data set allowing for displacement currents (model DL), (c) the full set of frequencies in the quasi-static approximation (model QF) and (d) the full set of frequencies allowing for displacement currents (model DF). The lines marked by C and D indicate seismic reflectors from Juhlin & Palm (1999) (their fig. 8). The resistivity values of borehole KAV01 are taken from the normal-resistivity log presented in Gentzschein *et al.* (1987). In contrast to models QL and QF, models DL and DF have a more realistic range of resistivities if compared in terms of the range observed in the normal-resistivity log. Furthermore, the resistivity—depth section of model DF at borehole KAV01 is in good agreement with the normal-resistivity log down to a depth of 230 m, and the positions of the seismic reflectors are in good agreement with resistivity contrasts in model DF.

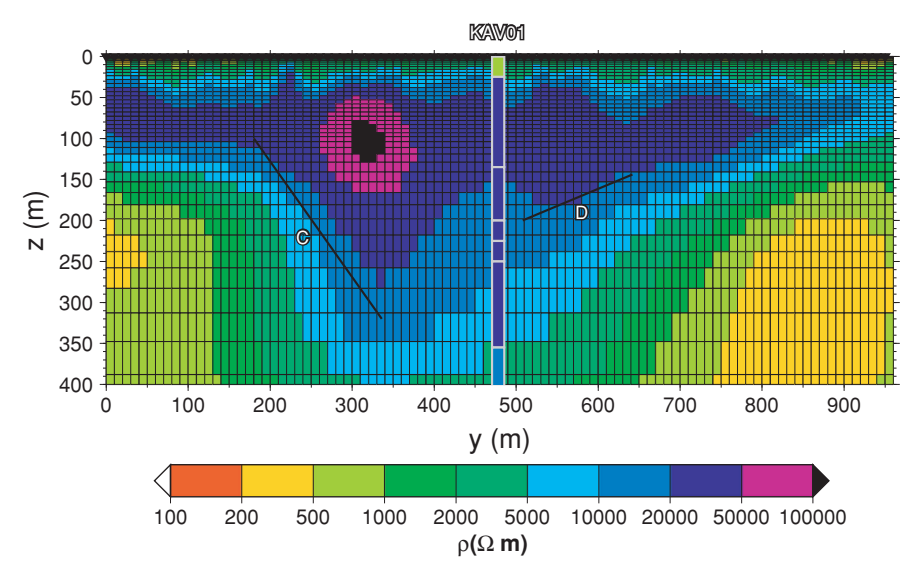
currents. We assumed the relative dielectric permittivity to be $\epsilon_r = 6$, which, for granite, is in the range between 5 and 8, given by Reynolds (1997). Variation of the permittivity in this range leads to only small differences of the resistivity models for the Ävrö data (not shown).

Our quasi-static determinant model for the lowest frequencies up to $56\,\mathrm{kHz}$ (model QL) in Fig. 14(a) resembles the corresponding model by Linde & Pedersen (2004) (their fig. 9d) strongly. We did not include the shallow sea (less than 10 m deep) to the east of Ävrö as *a priori* information, as this turned out to be of negligible importance. The central unfractured granite reaches resistivities up to $500\,000\,\Omega$ m. The conductor at the western end of the profile is interpreted by Linde & Pedersen (2004) as a 150 m wide wet fracture zone, assumed to be related to seismic reflector C of Juhlin & Palm (1999), although the positions of the conductor and reflector are not in very good agreement. The subhorizontal seismic reflector D does not appear to be related to any structure in the resistivity model. The rms misfit of model QL is 1.56.

The inversion with displacement currents for the low-frequency data set gives a model (model DL in Fig. 14b) with a significantly reduced range of resistivities from 300 to $100\,000\,\Omega$ m. The conductors at 50 and 850 m along the profile appear at greater depth and the



(c) model QF for the full set of frequencies and the quasi-static case



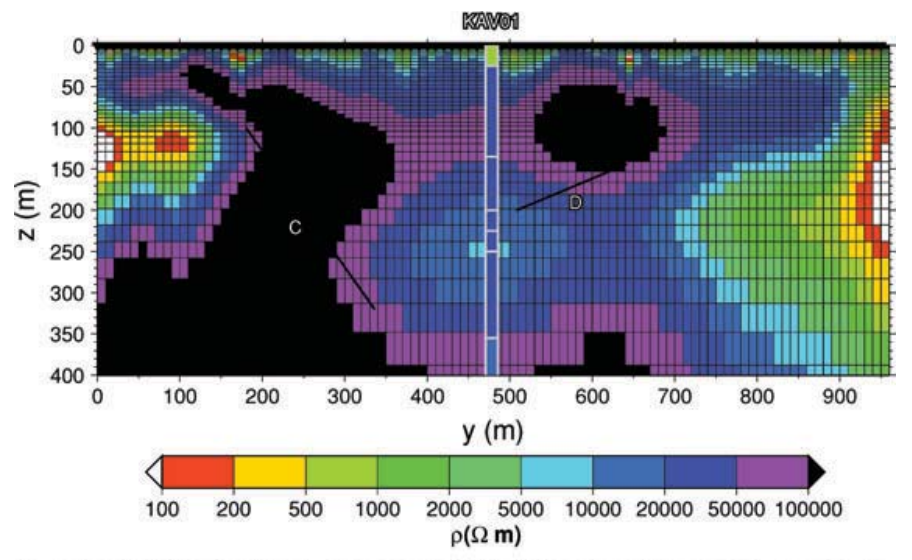
(d) model DF for the full set of frequencies and the general case with displacement currents

Figure 14. (Continued.)

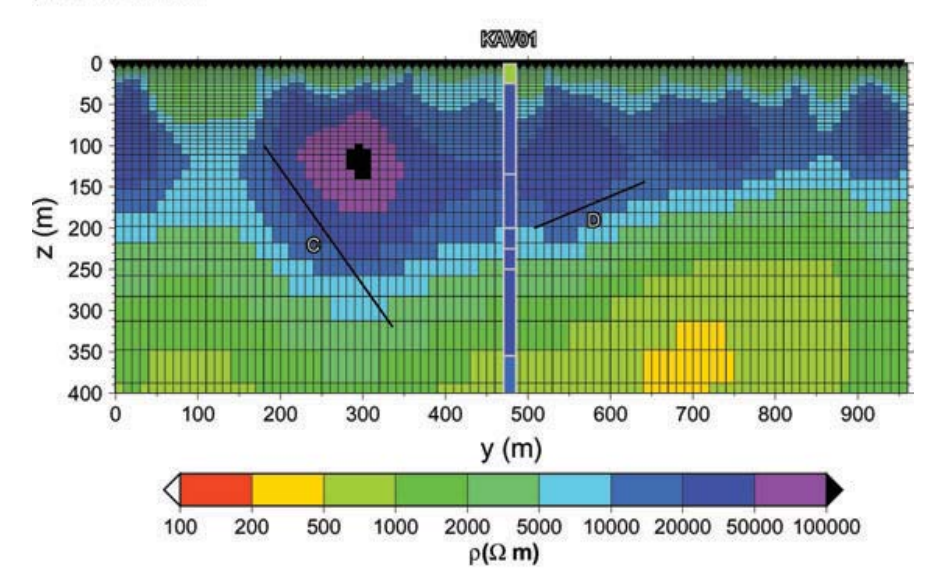
boundary between the central resistor and the western conductors is less steep than in the model QL (Fig. 14a). The rms misfit of model DL is 2.03.

The quasi-static inversion for the full set of frequencies (model QF in Fig. 14c) leads to a transition into the top of the central resistor that is sharper than in model QL (Fig. 14a). The resistivity of the central resistor is as high as $5 \times 10^6 \Omega$ m. The positions of the conductors at profile metres 50 and 850 is very similar to the positions in model QL. The rms misfit of model QF is 3.16.

In comparison to the quasi-static inversions, the inversion with displacement currents for all frequencies gives a model [model DF in Fig. 14(d) with an rms error of 2.60] that shows a less extreme range of resistivities, both at depth and close to the surface. The depth to the conductors at both ends of the profile is about 50 m larger than in the quasi-static models QL and QF in Figs 14(a) and (c), respectively. The model is also in better agreement with the positions of the seismic reflectors. The position of seismic reflector C conforms to an expected boundary between an unfractured resistive granite body and water saturated fractured bedrock. Therefore, we would expect reflector C to represent a boundary of rock units, with different grades of fracturing, rather than a 150 m wide fracture zone, as proposed by Linde & Pedersen (2004). Similarly, reflector D appears to coincide with a subhorizontal boundary of rock units. Furthermore, the model in Fig. 14(d) is in very good agreement with the resistivities of the normal-resistivity log of borehole KAV01 (Gentzschein *et al.* 1987), down to a depth of 230 m. At greater depth, the model might be more influenced by the smoothness constraint imposed during the inversion than the data. Compared with model DF, model DL (Fig. 14b) deviates from the normal-resistivity log at shallow depth down to 100 m and the positions of



(a) model TEDF for the full set of frequencies in the TE-mode and the general case with displacement currents



(b) model TMDF for the full set of frequencies in the TM-mode and the general case with displacement currents

Figure 15. Models of the inversion of (a) TE-mode data (model TEDF) and (b) TM-mode data (model TMDF) from Ävrö for the full set of frequencies allowing for displacement currents. The lines marked by C and D indicate seismic reflectors from Juhlin & Palm (1999). The resistivity values of borehole KAV01 are taken from the normal-resistivity log presented in Gentzschein *et al.* (1987). The resistivities of the central resistor in model TEDF are as high as $300\,000\,\Omega$ m. Compared with model DF (Fig. 14d), neither model TEDF nor model TMDF shows similarly good agreement with the positions of the seismic reflectors C and D or the normal-resistivity log.

the seismic reflectors are not as representative as bounds of different rock units. Hence, it appears that the inclusion of high-frequency data is of great importance during the modelling process.

As a verification that the 2-D inverse models of determinant data are less biased by 3-D structures off the profile, the inverse models of TE-mode data (model TEDF) and TM-mode data (model TMDF) are shown in Figs 15(a) and (b), respectively. In both inversions, the full set of frequencies was used and displacement currents were accounted for. The rms fits of 4.56 for the TE-mode model (reached after nine iterations) and 3.67 for the TM-mode model (reached after five iterations) are both significantly higher than that of model DF. The worst data fits of models TEDF and TMDF (not shown) are obtained at the western end of the profile, where strong 3-D effects in the VMT are observed by Linde & Pedersen (2004). In model TEDF, resistivities of the central resistor are as high as $300\,000\,\Omega$ m. Compared with model

DF (Fig. 14d), neither model TEDF nor model TMDF shows similarly good agreement with the positions of the seismic reflectors C and D of Juhlin & Palm (1999) or the normal-resistivity log by Gentzschein *et al.* (1987).

5 DISCUSSION AND CONCLUSIONS

We demonstrated the effect of displacement currents on 2-D TM-mode, TE-mode and VMT data, measured with the RMT method at frequencies between 10 and $300\,\mathrm{kHz}$. Forward modelling of subsurfaces with resistivities larger than $1000\,\Omega\,\mathrm{m}$ confirms that responses computed in the quasi-static approximation, that is, when displacement currents are neglected, become increasingly inaccurate, with rising frequency. For a homogeneous half-space, both apparent resistivity and phase, computed with displacement currents, decrease from their constant values in the quasi-static approximation, with increasing frequency. At high frequencies, the dielectric effect leads to the occurrence of distinct sign reversals in the real part of the VMT, which are not observed in the quasi-static approximation and might lead to artefactual 2-D or 3-D structures in an interpretation, based on the quasi-static approximation.

The interpretation of high-frequency RMT data with an inverse scheme that operates in the quasi-static approximation will inevitably lead to an inverse model with artefactual structures. As can be seen from the quasi-static interpretation of our synthetic data example in Fig. 11, the resistivities found in this inverse model vary over a larger range than those of the true model (Fig. 9). Typical artefactual structures include conductive near-surface layers, regions of excessively high resistivities next to conductors, as well as conductors that deviate strongly from their true shapes and positions. As only the resistivity distribution is inverted in the scheme presented here, a value for the dielectric permittivity must be chosen before the inversion. The relative dielectric permittivity of bedrock is typically in the range of 5 to 9 (e.g. Reynolds 1997, table 12.3), and a variation in this range does not lead to any important differences in the obtained resistivity models.

Typically, the primary EM field from remote radio transmitters has an angle of incidence that is close to grazing incidence at the measurement site. The assumption of vertically incident plane waves in the modelling code is a limitation, which is of minor importance in many practical situations. Often, a conductive surface layer consisting of, for instance, weathered bedrock or glacial till is present in the area of interest and refracts the incident field towards the vertical due to its relatively low resistivity.

For the Ävrö field data, the inversion that allows for displacement currents and includes high-frequency data produces a model that is in very good agreement with the results of other geophysical methods. The seismic reflectors C and D by Juhlin & Palm (1999) coincide with the boundaries between structures of different conductivity (Fig. 14d). The resistivity depth section of the model at borehole KAV01 matches the normal-resistivity log by Gentzschein *et al.* (1987) very well, down to a depth of 230 m below which the model might be strongly influenced by the smoothness constraint applied during the inversion. The inverse models computed in the quasi-static approximation (Figs 14a and c) contain artefactual structures, with unrealistically large resistivities, even if only the low-frequency data set is inverted (Fig. 14a).

ACKNOWLEDGMENTS

The original 2-D MT code by WS at Mahidol University is supported by a research grant from the Thailand Research Fund (TRF: RMU5080025). Nazli Ismail of Uppsala University computed the 3-D forward responses with the X3D code. Dmitry Avdeev, IZMIRAN, Russian Academy of Sciences, spent a large amount of money on the telephone, from Japan, to correct our X3D input files. A discussion with John Weaver, University of Victoria, clarified a few theoretical aspects. We would also like to thank Ute Weckmann, GFZ Potsdam and an anonymous reviewer for their comments, which helped to improve the manuscript.

REFERENCES

- Anderson, E. et al., 1999. LAPACK Users' Guide, 3rd edn, Society for Industrial and Applied Mathematics, Philadelphia, PA, USA.
- Aprea, C., Booker, J.R. & Smith, J.T., 1997. The forward problem of electromagnetic induction: accurate finite-difference approximations for two-dimensional discrete boundaries with arbitrary geometry, *Geophys. J. Int.*, 129, 29–40.
- Avdeev, D.B., Kuvshinov, A.V., Pankratov, O.G. & Newman, G.A., 2002. Three-dimensional induction logging problems, part 1: an integral equation solution and model comparisons, *Geophysics*, 67(2), 413–426.
- Bastani, M. & Pedersen, L.B., 2001. Estimation of magnetotelluric transfer functions from radio transmitters, *Geophysics*, 66(4), 1038–1051.
- Brewitt-Taylor, C.R. & Weaver, J.T., 1976. On the finite difference solution of two-dimensional induction problems, *Geophys. J. R. astr. Soc.*, **47**(2), 375–396.
- Crossley, D.J., 1981. The theory of EM surface wave impedance measurements, in *Geophysical Applications of Surface Wave Impedance Measurements*, Paper no. 81-15, pp. 1–17, eds Collet, L.S. & Jensen, O.G., Geological Survey of Canada.
- Fraser, D.C., Stodt, J.A. & Ward, S.H., 1990. The effect of displacement currents on the response of a high-frequency helicopter elec-

- tromagnetic system, in *Geotechnical and Environmental Geophysics*, Vol. 2, pp. 89–95, ed. Ward, S.H., SEG, Tulsa.
- Freund, R.W., 1992. Conjugate gradient-type methods for linear systems with complex symmetric coefficient matrices, SIAM J. Sci. Stat. Comput., 13(1), 425–448.
- Gentzschein, B., Nilsson, G. & Steinberg, L., 1987. Preliminary investigations of fracture zones at Ävrö results from investigations performed July 1986 May 1987, SKB Progress Report 25–87-16, SKB.
- Golub, G. & van Loan, C., 1996. *Matrix Computations*, Johns Hopkins Studies in the Mathematical Sciences, 3rd edn, Johns Hopkins University Press, Baltimore and London.
- Hohmann, G.W., 1987. Numerical modeling for electromagnetic methods in geophysics, in *Electromagnetic Methods in Applied Geophysics*, Vol. 1 (Theory), pp. 313–363, ed. Nabighian, M.N., SEG, Tulsa.
- Huang, H.P. & Fraser, D.C., 2002. Dielectric permittivity and resistivity mapping using high-frequency, helicopter-borne EM data, *Geophysics*, 67(3), 727–738.
- Juhlin, C. & Palm, H., 1999. 3-D structure below Ävrö island from highresolution reflection seismic studies, southeastern Sweden, *Geophysics*, 64, 662–667.
- Keller, G.V., 1987. Rock and mineral properties, in Electromagnetic

Methods in Applied Geophysics, Vol. 1 (Theory), pp. 12–51, ed. Nabighian, M.N., SEG, Tulsa.

Linde, N. & Pedersen, L.B., 2004. Characterization of a fractured granite using radio magnetotelluric (RMT) data, Geophysics, 69(5), 1155–1165.

McNeill, J.D. & Labson, V., 1991. Geological mapping using VLF radio fields, in *Electromagnetic Methods in Applied Geophysics*, Vol. 2 (Application), Parts A. & B, pp. 521–640, ed. Nabighian, M.N., SEG, Tulsa.

Nabulsi, K.A. & Wait, J.R., 1996. TM reflection from an insulating layer within a lossy half-space, J. Appl. Geophys., 34(4), 271–276.

Pedersen, L.B. & Engels, M., 2005. Routine 2D inversion of magnetotelluric data using the determinant of the impedance tensor, *Geophysics*, 70(2), G33–G41.

Persson, L. & Pedersen, L.B., 2002. The importance of displacement currents in RMT measurements in high resistivity environments, *J. Appl. Geophys.*, 51(1), 11–20.

Reynolds, J.M., 1997. An Introduction to Applied and Environmental Geophysics, John Wiley & Sons Ltd, Chichester, UK.

Rodi, W.L., 1976. A technique for improving the accuracy of finite element solutions for magnetotelluric data, *Geophys. J. R. astr. Soc.*, 44, 483–506.

Rodi, W. & Mackie, R.L., 2001. Nonlinear conjugate gradients algorithm for 2-D magnetotelluric inversion, *Geophysics*, **66**(1), 174–187.

Sinha, A.K., 1977. Influence of altitude and displacement currents on planewave EM fields. Geophysics, 42(1), 77–91.

Siripunvaraporn, W. & Egbert, G., 2000. An efficient data-subspace inversion method for 2-D magnetotelluric data, *Geophysics*, 65(3), 791–803.

Song, Y., Kim, H.J. & Lee, K.H., 2002. High-frequency electromagnetic impedance method for subsurface imaging, *Geophysics*, **67**(2), 501–510.

Stewart, D.C., Anderson, W.L., Grover, T.P. & Labson, V.F., 1994. Shallow subsurface mapping by electromagnetic sounding in the 300 kHz to

30 MHz range: model studies and prototype system assessment, *Geophysics*, **59**(8), 1201–1210.

Wait, J.R., 1953. Propagation of radio waves over a stratified ground, Geophysics, 18(2), 416–422.

Wait, J.R., 1970. Electromagnetic Waves in Stratified Media, Vol. 3: International series of monographs in electromagnetic waves, Pergamon Press, Oxford, New York.

Wait, J.R. & Nabulsi, K.A., 1996. Wave tilt of radio waves propagating over a layered ground, *Geophysics*, 61(6), 1647–1652.

Ward, S.H. & Hohmann, D.W., 1987. Electromagnetic theory for geophysical applications, in *Electromagnetic Methods in Applied Geophysics*, Vol. 1 (Theory), pp. 131–311, ed. Nabighian, M.N., SEG, Tulsa.

Ward, S.H., Jiracek, G.R. & Linlor, W.I., 1968. Electromagnetic reflection from a plane-layered lunar model. *J. Geophys. Res.*, 73(4), 1355–1372.

Weaver, J.T., LeQuang, B.V. & Fischer, G., 1985. A comparison of analytical and numerical results for a two-dimensional control model in electromagnetic induction, I: B-polarization calculations, *Geophys. J. R. astr. Soc.*, 82, 263–277.

Weaver, J.T., Le Quang, B.V. & Fischer, G., 1986. A comparison of analytical and numerical results for a two-dimensional control model in electromagnetic induction, II: E-polarization calculations, *Geophys. J. R. astr. Soc.*, 87, 917–948.

Yin, C. & Hodges, G., 2005. Influence of displacement currents on the response of helicopter electromagnetic systems, *Geophysics*, 70(4), G95–G100.

Zacher, G., 1992. Hochfrequente Elektromagnetik auf Altlasten, in *Protokoll über das 14. Kolloquium Elektromagnetische Tiefenforschung, Borkheide*, pp. 357–363, eds Haak, V. & Rodemann, H., Dt. Geophys. Gesellschaft, GFZ Potsdam.

APPENDIX A: FINITE-DIFFERENCE APPROXIMATION

The derivation of the finite-difference approximation (FDA) with the integration method following Hohmann (1987) and Aprea *et al.* (1997) is particularly instructive. In a finite-difference mesh, a node (i, j) is a corner point of four finite-difference cells, with admittivities $\hat{y}_{i-1/2,j-1/2}$, $\hat{y}_{i+1/2,j-1/2}$, $\hat{y}_{i-1/2,j+1/2}$, and $\hat{y}_{i+1/2,j+1/2}$ (Fig. A1). The cells have widths $\Delta y_{i-1/2}$ and $\Delta y_{i+1/2}$ and heights $\Delta z_{j-1/2}$ and $\Delta z_{j+1/2}$. The rectangle A has the centres of the cells as its corner points (Fig. A1). It is assumed that the horizontal electric field component of the TE-mode and the horizontal magnetic field component of the TM-mode at node (i, j) are $E_x^{i,j}$ and $H_x^{i,j}$, respectively, and that the magnetic permeability is equal to its vacuum value μ_0 . Nodes along the boundary of the finite-difference mesh are called boundary nodes. All other nodes are called inner nodes. Finite-difference equations for the TM- and TE-mode are obtained by integrating eqs 14 and 13, respectively, over the surface of A. This surface integral is then transformed to a contour integral around the perimeter ∂A of the surface A with Gauss' Theorem.

Hence, for the TE-mode,

$$\int_{A} (\hat{z}\hat{y}E_{x}) \, \mathrm{d}A = \int_{A} (\nabla \cdot \nabla E_{x}) \, \mathrm{d}A = \int_{\partial A} (\mathbf{n} \cdot \nabla E_{x}) \, \mathrm{d}l, \tag{A1}$$

where \mathbf{n} is an outward unit normal vector on the edges of A.

The part of A, for instance, which is entirely situated to the upper left-hand side of node (i, j), contributes to the surface integral in eq. (A1) with

$$\int_{4}^{ul} (\hat{z}\hat{y}E_x) dA \approx \hat{z}\hat{y}_{i-1/2,j-1/2}E_x^{i,j} \frac{\Delta y_{i-1/2}}{2} \frac{\Delta z_{j-1/2}}{2}.$$
(A2)

For the upper edge of the rectangle A, for instance, the integral around the perimeter ∂A can be approximated as

$$\int_{\partial A}^{u} (\mathbf{n} \cdot \nabla E_x) \, \mathrm{d}l \approx \left[-\frac{E_x^{i,j} - E_x^{i,j-1}}{\Delta z_{j-1/2}} \right] \frac{\Delta y_{i+1/2} + \Delta y_{i-1/2}}{2},\tag{A3}$$

where $(\Delta y_{i+1/2} + \Delta y_{i-1/2})/2$ is the length of the perimeter ∂A on the upper edge of A and \mathbf{n} , which equals (0, 0, -1) on the upper edge of A, collects the vertical component of ∇E_x , that is, $(\nabla E_x)_z \approx (E_x^{i,j} - E_x^{i,j-1})/\Delta z_{j-1/2}$, multiplied by -1.

In total, this leads to the following approximations (cf. Aprea et al. 1997):

$$\int_{A} (\hat{z}\hat{y}E_x) \, \mathrm{d}A \approx \frac{1}{4} \hat{z}\hat{y}_{i,j}^{\mathrm{int}} E_x^{i,j} + O\left(\Delta^3\right),\tag{A4}$$

© 2008 The Authors, *GJI*, **175**, 486–514 Journal compilation © 2008 RAS

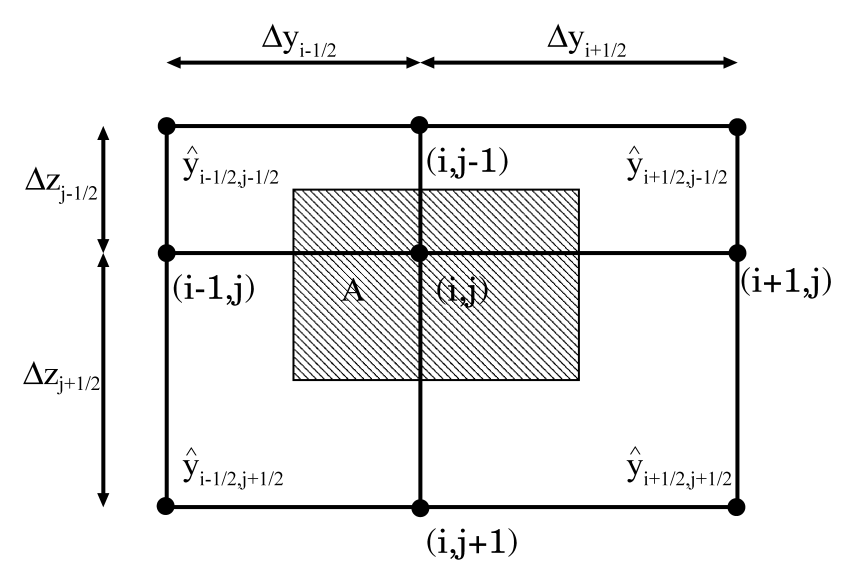


Figure A1. Finite-difference mesh around node (i,j). The four surrounding cells have admittivities $\hat{y}_{i-1/2,j-1/2}$, $\hat{y}_{i+1/2,j-1/2}$, $\hat{y}_{i-1/2,j+1/2}$ and $\hat{y}_{i+1/2,j+1/2}$. The heights and widths of the surrounding cells are $\Delta z_{j-1/2}$ and $\Delta y_{j-1/2}$ and $\Delta y_{i-1/2}$ and $\Delta y_{i+1/2}$, respectively. The rectangle A has its corner points at the centres of the cells.

$$\int_{\partial A} (\mathbf{n} \cdot \nabla E_{x}) \, dl \approx \frac{\Delta y_{i+1/2} + \Delta y_{i-1/2}}{2} \left[\frac{E_{x}^{i,j+1} - E_{x}^{i,j}}{\Delta z_{j+1/2}} - \frac{E_{x}^{i,j} - E_{x}^{i,j-1}}{\Delta z_{j-1/2}} \right]
+ \frac{\Delta z_{j+1/2} + \Delta z_{j-1/2}}{2} \left[\frac{E_{x}^{i+1,j} - E_{x}^{i,j}}{\Delta y_{i+1/2}} - \frac{E_{x}^{i,j} - E_{x}^{i-1,j}}{\Delta y_{i-1/2}} \right]
+ O(\Delta^{2}),$$
(A5)

where

$$\hat{y}_{i,j}^{\text{int}} = \hat{y}_{i-1/2,j-1/2} \Delta y_{i-1/2} \Delta z_{j-1/2} + \hat{y}_{i+1/2,j-1/2} \Delta y_{i+1/2} \Delta z_{j-1/2}
+ \hat{y}_{i-1/2,j+1/2} \Delta y_{i-1/2} \Delta z_{j+1/2} + \hat{y}_{i+1/2,j+1/2} \Delta y_{i+1/2} \Delta z_{j+1/2},$$
(A6)

$$\hat{y}_{i,j}^{\text{avg}} = \frac{1}{\Delta y_{i-1/2} \Delta z_{j-1/2} + \Delta y_{i+1/2} \Delta z_{j-1/2} + \Delta y_{i-1/2} \Delta z_{j+1/2} + \Delta y_{i+1/2} \Delta z_{j+1/2}} \hat{y}_{i,j}^{\text{int}}$$
(A7)

and $O(\Delta^2)$ are terms of second or higher order in $\Delta y_{i\pm 1/2}$ or $\Delta z_{j\pm 1/2}$.

After rearranging, one obtains

$$0 = 2 \frac{\Delta y_{i+1/2} + \Delta y_{i-1/2}}{\Delta z_{j+1/2}} E_x^{i,j+1} + 2 \frac{\Delta y_{i+1/2} + \Delta y_{i-1/2}}{\Delta z_{j-1/2}} E_x^{i,j-1}$$

$$+ 2 \frac{\Delta z_{j+1/2} + \Delta z_{j-1/2}}{\Delta y_{i+1/2}} E_x^{i+1,j} + 2 \frac{\Delta z_{j+1/2} + \Delta z_{j-1/2}}{\Delta y_{i-1/2}} E_x^{i-1,j}$$

$$- \left\{ 2 \frac{\Delta y_{i+1/2} + \Delta y_{i-1/2}}{\Delta z_{j+1/2}} + 2 \frac{\Delta y_{i+1/2} + \Delta y_{i-1/2}}{\Delta z_{j-1/2}} + 2 \frac{\Delta y_{i+1/2} + \Delta y_{i-1/2}}{\Delta z_{j-1/2}} + 2 \frac{\Delta z_{j+1/2} + \Delta z_{j-1/2}}{\Delta y_{i-1/2}} + 2 \frac{\Delta z_{j+1/2} + \Delta z_{j-1/2}}{\Delta z_{j-1/2}} + 2 \frac{\Delta$$

Similarly, the FDA of the TM mode can be derived. Gauss' Theorem gives

$$\int_{A} (\hat{z}H_{x}) dA = \int_{A} \left(\nabla \cdot \frac{1}{\hat{y}} \nabla H_{x} \right) dA = \int_{\partial A} \left(\mathbf{n} \cdot \frac{1}{\hat{y}} \nabla H_{x} \right) dI \tag{A9}$$

and the single terms can be approximated as

$$\int_{A} (\hat{z}H_{x}) dA \approx \hat{z}H_{x}^{i,j} \frac{(\Delta y_{i+1/2} + \Delta y_{i-1/2})(\Delta z_{j+1/2} + \Delta z_{j-1/2})}{4} + O\left(\Delta^{3}\right), \tag{A10}$$

$$\int_{\partial A} \left(\mathbf{n} \cdot \frac{1}{\hat{y}} \nabla H_{x} \right) dl \approx \frac{\Delta y_{i+1/2} + \Delta y_{i-1/2}}{2} \left[\frac{1}{\hat{y}_{i,j}^{d}} \frac{H_{x}^{i,j+1} - H_{x}^{i,j}}{\Delta z_{j+1/2}} - \frac{1}{\hat{y}_{i,j}^{u}} \frac{H_{x}^{i,j} - H_{x}^{i,j-1}}{\Delta z_{j-1/2}} \right] + \frac{\Delta z_{j+1/2} + \Delta z_{j-1/2}}{2} \left[\frac{1}{\hat{y}_{i,j}^{r}} \frac{H_{x}^{i+1,j} - H_{x}^{i,j}}{\Delta y_{i+1/2}} - \frac{1}{\hat{y}_{i,j}^{l}} \frac{H_{x}^{i,j} - H_{x}^{i-1,j}}{\Delta y_{i-1/2}} \right] + O(\Delta^{2}),$$
(A11)

where the vertically and horizontally averaged inverse admittivities are given by

$$\frac{1}{\underline{\hat{y}}_{i,j}^d} = \frac{\frac{1}{\hat{y}_{i+1/2,j+1/2}} \Delta y_{i+1/2} + \frac{1}{\hat{y}_{i-1/2,j+1/2}} \Delta y_{i-1/2}}{\Delta y_{i+1/2} + \Delta y_{i-1/2}},$$
(A12)

$$\frac{1}{\hat{\underline{y}}_{i,j}^{u}} = \frac{\frac{1}{\hat{y}_{i+1/2,j-1/2}} \Delta y_{i+1/2} + \frac{1}{\hat{y}_{i-1/2,j-1/2}} \Delta y_{i-1/2}}{\Delta y_{i+1/2} + \Delta y_{i-1/2}},$$
(A13)

$$\frac{1}{\hat{\underline{y}}_{i,j}^r} = \frac{\frac{1}{\hat{y}_{i+1/2,j+1/2}} \Delta z_{j+1/2} + \frac{1}{\hat{y}_{i+1/2,j-1/2}} \Delta z_{j-1/2}}{\Delta z_{j+1/2} + \Delta z_{j-1/2}},$$
(A14)

$$\frac{1}{\hat{y}_{i,j}^{l}} = \frac{\frac{1}{\hat{y}_{i-1/2,j+1/2}} \Delta z_{j+1/2} + \frac{1}{\hat{y}_{i-1/2,j-1/2}} \Delta z_{j-1/2}}{\Delta z_{j+1/2} + \Delta z_{j-1/2}}.$$
(A15)

Again, rearranging gives

$$0 = 2 \frac{\Delta y_{i+1/2} + \Delta y_{i-1/2}}{\Delta z_{j+1/2}} \frac{1}{\hat{\underline{y}}_{i,j}^{d}} H_{x}^{i,j+1} + 2 \frac{\Delta y_{i+1/2} + \Delta y_{i-1/2}}{\Delta z_{j-1/2}} \frac{1}{\hat{\underline{y}}_{i,j}^{u}} H_{x}^{i,j-1}$$

$$+ 2 \frac{\Delta z_{j+1/2} + \Delta z_{j-1/2}}{\Delta y_{i+1/2}} \frac{1}{\hat{\underline{y}}_{i,j}^{r}} H_{x}^{i+1,j} + 2 \frac{\Delta z_{j+1/2} + \Delta z_{j-1/2}}{\Delta y_{i-1/2}} \frac{1}{\hat{\underline{y}}_{i,j}^{l}} H_{x}^{i-1,j}$$

$$- \left\{ 2 \frac{\Delta y_{i+1/2} + \Delta y_{i-1/2}}{\Delta z_{j+1/2}} \frac{1}{\hat{\underline{y}}_{i,j}^{d}} + 2 \frac{\Delta y_{i+1/2} + \Delta y_{i-1/2}}{\Delta z_{j-1/2}} \frac{1}{\hat{\underline{y}}_{i,j}^{u}} \right.$$

$$+ 2 \frac{\Delta z_{j+1/2} + \Delta z_{j-1/2}}{\Delta y_{i+1/2}} \frac{1}{\hat{\underline{y}}_{i,j}^{r}} + 2 \frac{\Delta z_{j+1/2} + \Delta z_{j-1/2}}{\Delta y_{i-1/2}} \frac{1}{\hat{\underline{y}}_{i,j}^{u}}$$

$$+ \hat{z} \left(\Delta y_{i+1/2} + \Delta y_{i-1/2} \right) \left(\Delta z_{j+1/2} + \Delta z_{j-1/2} \right) \right\} H_{x}^{i,j}.$$

$$(A16)$$

If considered at all inner mesh nodes (i, j), eqs (A8) and (A16) form systems of linear equations in the unknown horizontal electric and magnetic field components of the TE-mode and the TM-mode, respectively. Assuming that there are N_{za} air cells, N_{zb} earth cells and a total of $N_z = N_{za} + N_{zb}$ cells in the vertical direction and N_y cells in the horizontal direction, the horizontal field components E_x or H_x are to be computed at $(N_z - 1) \cdot (N_y - 1)$ inner mesh nodes. Boundary values have to be supplied at the edges of the mesh. Along the upper edge of the air half-space, the incident plane wave is assumed to have unit amplitude and zero phase. At the lower edge of the earth half-space, the electromagnetic (EM) field is assumed to have totally decayed, and along the lateral edges, the horizontal field components E_x or H_x are assumed to be that of the corresponding 1-D admittivity section along the particular side. This results in a system of $(N_z - 1) \cdot (N_y - 1)$ linear equations $\mathbf{K}\mathbf{x} = \mathbf{s}$ (one equation for each interior node), with the coefficient matrix \mathbf{K} , the vector \mathbf{x} of unknown horizontal field components of the TE- or TM-mode and a vector \mathbf{s} of boundary values. If a central node is located next to one or two boundary nodes, the terms in eqs (A8) or (A16), which contain the electric or magnetic boundary field components, are placed in the corresponding row of the right-hand side vector \mathbf{s} . If the nodes are arranged such that the vertical index j varies fastest, the finite-difference eq. (A8) or (A16) of central node (i,j) is contained in row number $(i-2)(N_z - 1) + (j-1)$ of $\mathbf{K}\mathbf{x} = \mathbf{s}$.

The auxiliary field components (H_y, H_z) of the TE-mode are derived as partial derivatives of E_x at the air-Earth interface (nodes at $j = N_{za} + 1$), by expanding E_x in a Taylor series of second order, around the considered node (i,j) and substituting eq. (13) for the second-order term as proposed by Weaver *et al.* (1986). Vertical expansion, both upwards and downwards from the considered node yields a central

difference formula for the horizontal magnetic field component H_y as

$$-\hat{z}H_{y}^{i,j} = \left(\frac{\partial E_{x}}{\partial z}\right)_{i,j}$$

$$= \frac{\Delta z_{j+1/2}\Delta z_{j-1/2}}{\Delta z_{j+1/2} + \Delta z_{j-1/2}} \left\{ \frac{E_{x}^{i,j+1}}{\Delta z_{j+1/2}^{2}} - \frac{E_{x}^{i,j-1}}{\Delta z_{j-1/2}^{2}} - \frac{1}{\Delta z_{j+1/2}^{2}} - \frac{1}{\Delta z_{j+1/2}^{2}} - \frac{1}{\Delta z_{j-1/2}^{2}} - \frac{1}{\Delta z_{j-1/2}^{2}} + \frac{1}{2}\hat{z}\left(\hat{y}_{i,j}^{d} - \hat{y}_{i,j}^{u}\right) \right] E_{x}^{i,j} \right\},$$
(A17)

where

$$\hat{y}_{i,j}^d = \frac{\hat{y}_{i+1/2,j+1/2} \Delta y_{i+1/2} + \hat{y}_{i-1/2,j+1/2} \Delta y_{i-1/2}}{\Delta y_{i+1/2} + \Delta y_{i-1/2}},\tag{A18}$$

$$\hat{y}_{i,j}^{u} = \frac{\hat{y}_{i+1/2,j-1/2} \Delta y_{i+1/2} + \hat{y}_{i-1/2,j-1/2} \Delta y_{i-1/2}}{\Delta y_{i+1/2} + \Delta y_{i-1/2}}.$$
(A19)

Similarly, horizontal expansion both to the left- and right-hand side of the considered node yields a central difference formula for the vertical magnetic field component H_z of the form

$$\hat{z}H_{z}^{i,j} = \left(\frac{\partial E_{x}}{\partial y}\right)_{i,j}
= \frac{\Delta y_{i+1/2}\Delta y_{i-1/2}}{\Delta y_{i+1/2} + \Delta y_{i-1/2}} \left\{ \frac{E_{x}^{i+1,j}}{\Delta y_{i+1/2}^{2}} - \frac{E_{x}^{i-1,j}}{\Delta y_{i-1/2}^{2}} - \left[\frac{1}{\Delta y_{i+1/2}^{2}} - \frac{1}{\Delta y_{i-1/2}^{2}} + \frac{1}{2}\hat{z}\left(\hat{y}_{i,j}^{r} - \hat{y}_{i,j}^{l}\right)\right] E_{x}^{i,j} \right\}$$
(A20)

where

$$\hat{y}_{i,j}^r = \frac{\hat{y}_{i+1/2,j+1/2}\Delta z_{j+1/2} + \hat{y}_{i+1/2,j-1/2}\Delta z_{j-1/2}}{\Delta z_{j+1/2} + \Delta z_{j-1/2}}$$
(A21)

$$\hat{y}_{i,j}^{l} = \frac{\hat{y}_{i-1/2,j+1/2}\Delta z_{j+1/2} + \hat{y}_{i-1/2,j-1/2}\Delta z_{j-1/2}}{\Delta z_{j+1/2} + \Delta z_{j-1/2}}.$$
(A22)

A corresponding derivation of the auxiliary electric field components (E_y, E_z) of the TM-mode follows Weaver *et al.* (1985). The horizontal electric field component E_y is computed by expanding H_x in a Taylor series, both upwards and downwards from the considered node (i, j). Hence.

$$j_y^{i,j} = \left(\frac{\partial H_x}{\partial z}\right)_{i,j} = \frac{N_{i,j}}{\Delta z_{j+1/2} + \Delta z_{j-1/2}},\tag{A23}$$

where

$$\begin{split} N_{i,j} &= \frac{\Delta z_{j-1/2}}{\Delta z_{j+1/2}} H_x^{i,j+1} - \frac{\Delta z_{j+1/2}}{\Delta z_{j-1/2}} H_x^{i,j-1} - \frac{O_{i,j}}{2} \left(\frac{H_x^{i+1,j}}{\Delta y_{i+1/2}} - \frac{H_x^{i-1,j}}{\Delta y_{i-1/2}} \right) \\ &+ \left[\frac{\Delta z_{j+1/2}}{\Delta z_{j-1/2}} - \frac{\Delta z_{j-1/2}}{\Delta z_{j+1/2}} + \frac{1}{2} \frac{\Delta y_{i-1/2} - \Delta y_{i+1/2}}{\Delta y_{i-1/2} \Delta y_{i+1/2}} O_{i,j} \right. \\ &+ \left. \hat{z} \frac{\Delta z_{j-1/2} \Delta z_{j+1/2}}{2} \left(\hat{\underline{y}}_{i,j}^u - \hat{\underline{y}}_{i,j}^d \right) \right] H_x^{i,j}, \\ O_{i,j} &= -\frac{\Delta z_{j-1/2} \Delta z_{j+1/2}}{\Delta y_{i-1/2} + \Delta y_{i+1/2}} \left[\hat{\underline{y}}_{i,j}^d \left(\frac{1}{\hat{y}_{i+1/2,j+1/2}} - \frac{1}{\hat{y}_{i-1/2,j+1/2}} \right) \right. \\ &\left. - \hat{\underline{y}}_{i,j}^u \left(\frac{1}{\hat{y}_{i+1/2,j+1/2}} - \frac{1}{\hat{y}_{i-1/2,j+1/2}} \right) \right]. \end{split}$$

After obtaining $j_y^{i,j}$ from the above equations, the two one-sided values $E_y^{i-,j}$ and $E_y^{i+,j}$ of the electric field component E_y can be computed. In contrast to eq. (24) in Weaver *et al.* (1985), the current density $j_y^{i,j}$ must be divided by the left- and right-hand sided vertically averaged admittivities (eqs A22 and A21, respectively) to obtain $E_y^{i-,j}$ and $E_y^{i+,j}$, respectively, that is,

$$\hat{y}_{i,j}^l E_{\nu}^{i-,j} = \hat{y}_{i,j}^r E_{\nu}^{i+,j} = j_{\nu}^{i,j}. \tag{A24}$$

The use of averaged admittivities is motivated by considering the integrated current $I_y = \iint_{x-z-plane} j_y \, dx dz$ through any surface y = const. To assign a unique value to $E_y^{i,j}$, the current density $j_y^{i,j}$ is typically divided by the average admittivity $\hat{y}_{i,j}^{\text{avg}}$ given in eq. (A7), that is,

$$\hat{y}_{i,j}^{\text{avg}} E_{\nu}^{i,j} = j_{\nu}^{i,j}. \tag{A25}$$

APPENDIX B: SOLUTION METHODS FOR LINEAR SYSTEMS

As shown in Appendix A, the FDAs of Helmholtz eqs (13) and (14) result in system matrices that are sparse, complex and symmetric with two subdiagonals and two super-diagonals. For the solution of the FDAs, both direct and iterative solvers are desirable. The solution with a direct method is rewarding, as soon as the same system matrix is used for the solution with multiple right-hand side vectors (Rodi 1976; Siripunvaraporn & Egbert 2000), for example, for multiple pseudo-forward problems arising in the computation of the sensitivity matrix (see Appendix C). As the system matrix is non-Hermitian and, hence, not positive-definite, the LU-decomposition rather than the Cholesky-decomposition has to be used as a direct method (Golub & van Loan 1996). If the system of linear equations is to be solved for a single right-hand side vector, an iterative solver can provide significant computational savings over a direct method. The iterative bi-conjugate gradient method (BiCG), which is used by Siripunvaraporn & Egbert (2000) for quasi-static problems, breaks down if applied to the general forward problem with displacement currents. Freund (1992) gives two possible reasons for the breakdown. As the proper inner product for the base vectors of a Krylov subspace constructed during the Lanczos process of complex-symmetric matrices is $(\mathbf{x}, \mathbf{y}) = \mathbf{x}^T \mathbf{y}$, quasi-null vectors $(\tilde{\mathbf{v}}_j, \tilde{\mathbf{v}}_j) = \tilde{\mathbf{v}}_j^T \tilde{\mathbf{v}}_j = 0$ may occur and cause a division by zero, during the normalization of the new base vector $\mathbf{v}_j = \tilde{\mathbf{v}}_j/(\tilde{\mathbf{v}}_j, \tilde{\mathbf{v}}_j)$. In computer arithmetic, the tridiagonal matrix, constructed during the Lanczos-process, might be nearly singular and the solution update, constructed from the Petrov-Galerkin conditions, might give a bad approximation to the true solution, leading to erratic convergence behaviour with wildly varying residual norms. It should be possible to circumvent these problems by using the quasi-minimal residual method (QMR) as proposed by Freund (1992), where the problem of quasi-null vectors is amended with look-ahead techniques and the Petrov-Galerkin conditions are replaced by a quasi-minimal residual property. We have not yet succeed, however, in implementing the QMR solver for the general forward problem with displacement currents. Therefore, we use the direct LU-method as the sole solver at present.

APPENDIX C: COMPUTATION OF THE SENSITIVITY MATRIX

An efficient scheme for the computation of sensitivity matrices was proposed by Rodi (1976) and Rodi & Mackie (2001). The kth impedance or VMT datum for a given model m is expressed in terms of the horizontal electric or magnetic field component of the TE- or TM-mode, respectively, as

$$Z^{k}(\mathbf{m}) = \frac{\mathbf{a}_{k}(\mathbf{m})^{T} \mathbf{x}(\mathbf{m})}{\mathbf{b}_{k}(\mathbf{m})^{T} \mathbf{x}(\mathbf{m})},$$
(C1)

$$\mathbf{x}(\mathbf{m}) = \begin{cases} H_x \text{ at inner mesh nodes for TM-mode impedance} \\ E_x \text{ at inner mesh nodes for TE-mode impedance or VMT} \end{cases}$$
 (C2)

and $\mathbf{a}_k(\mathbf{m})$ and $\mathbf{b}_k(\mathbf{m})$ are coefficient vectors from the central difference computation of the auxiliary fields in the TM-mode impedance, TE-mode impedance and VMT.

The entry of the sensitivity matrix for the kth impedance or VMT datum with respect to (w.r.t.) the lth model parameter is then computed

$$J^{kl}(\mathbf{m}) = \frac{\partial Z^{k}(\mathbf{m})}{\partial m^{l}}$$

$$= \frac{1}{\mathbf{b}_{k}^{T} \mathbf{x}} \frac{\partial \left(\mathbf{a}_{k}^{T} \mathbf{x}\right)}{\partial m^{l}} - \frac{\mathbf{a}_{k}^{T} \mathbf{x}}{\left(\mathbf{b}_{k}^{T} \mathbf{x}\right)^{2}} \frac{\partial \left(\mathbf{b}_{k}^{T} \mathbf{x}\right)}{\partial m^{l}}$$

$$= \left(\frac{1}{\mathbf{b}_{k}^{T} \mathbf{x}} \frac{\partial \mathbf{a}_{k}}{\partial m^{l}} - \frac{\mathbf{a}_{k}^{T} \mathbf{x}}{\left(\mathbf{b}_{k}^{T} \mathbf{x}\right)^{2}} \frac{\partial \mathbf{b}_{k}}{\partial m^{l}}\right)^{T} \mathbf{x} + \left(\frac{1}{\mathbf{b}_{k}^{T} \mathbf{x}} \mathbf{a}_{k} - \frac{\mathbf{a}_{k}^{T} \mathbf{x}}{\left(\mathbf{b}_{k}^{T} \mathbf{x}\right)^{2}} \mathbf{b}_{k}\right)^{T} \frac{\partial \mathbf{x}}{\partial m^{l}}.$$
(C3)

The definitions

$$\mathbf{c}_k = \frac{1}{\mathbf{b}_k^T \mathbf{x}} \mathbf{a}_k - \frac{\mathbf{a}_k^T \mathbf{x}}{\left(\mathbf{b}_k^T \mathbf{x}\right)^2} \mathbf{b}_k,\tag{C4}$$

$$\mathbf{d}_{kl} = \left(\frac{1}{\mathbf{b}_k^T \mathbf{x}} \frac{\partial \mathbf{a}_k}{\partial m^l} - \frac{\mathbf{a}_k^T \mathbf{x}}{\left(\mathbf{b}_k^T \mathbf{x}\right)^2} \frac{\partial \mathbf{b}_k}{\partial m^l}\right) \tag{C5}$$

and the relation from the forward problem,
$$\mathbf{K} \frac{\partial \mathbf{x}}{\partial m^l} = -\frac{\partial \mathbf{K}}{\partial m^l} \mathbf{x} + \frac{\partial \mathbf{s}}{\partial m^l},$$
give (C6)

$$J^{kl}(\mathbf{m}) = \mathbf{d}_{kl}^{T} \mathbf{x} + \mathbf{c}_{k}^{T} \mathbf{K}^{-1} \left(-\frac{\partial \mathbf{K}}{\partial m^{l}} \mathbf{x} + \frac{\partial \mathbf{s}}{\partial m^{l}} \right)$$

$$= \mathbf{d}_{kl}^{T} \mathbf{x} + \mathbf{u}_{k}^{T} \left(-\frac{\partial \mathbf{K}}{\partial m^{l}} \mathbf{x} + \frac{\partial \mathbf{s}}{\partial m^{l}} \right), \tag{C7}$$

© 2008 The Authors, GJI, 175, 486-514 Journal compilation © 2008 RAS

where the computation of \mathbf{u}_k as a solution of the pseudo-forward problem $\mathbf{K}^T \mathbf{u}_k = \mathbf{c}_k$ exploits the reciprocity of the forward problem (i.e. the symmetry of the forward system matrix \mathbf{K} and its inverse). The computation of \mathbf{u}_k for k = 1, ..., N is significantly faster than the computation of $\mathbf{K}^{-1}(-\frac{\partial \mathbf{K}}{\partial m^l}\mathbf{x} + \frac{\partial \mathbf{s}}{\partial m^l})$ for l = 1, ..., M in the case of typical 2-D problems, where the number of model parameters exceeds the number of data, that is, where M > N.

A model parameter $m^l = \rho_{i+1/2,j+1/2}$ is connected to the cell to the lower right-hand side of a node (i,j) through $l = j - N_{za} + (i-1) *N_{zb}$. Similarly, each data index k is connected to a single surface node $(i_s, j_s = N_{za} + 1)$ for a given frequency, where i_s and j_s indicate the node at which a certain receiver station is located.

C1 TM-mode

The computation of the sensitivities for the TM-mode turns out to be intriguingly complicated, as the derivatives of inverse admittivities w.r.t. resistivities are involved.

In the TM-mode, E_y is expressed through \mathbf{a}_k and H_x according to eqs (A23) and (A25) and \mathbf{b}_k is zero except for the kth entry, which is 1. Hence,

$$\mathbf{a}_k^T \mathbf{x} = E_y^k,$$

$$\mathbf{b}_k^T \mathbf{x} = H_y^k$$

and

$$\mathbf{c}_k = \frac{1}{H_x^k} \mathbf{a}_k - \frac{Z_{yx}^k}{H_x^k} \left(0, \dots, 0, \underbrace{1}_{k \text{th arry}}, 0, \dots, 0 \right), \tag{C8}$$

$$\mathbf{d}_{kl} = \frac{1}{H_v^k} \frac{\partial \mathbf{a}_k}{\partial m^l}.$$
 (C9)

The computation of \mathbf{d}_{kl} is simplified as \mathbf{b}_k does not depend on any model parameter. Furthermore, as \mathbf{a}_k is computed with a five-point-stencil FDA, each \mathbf{a}_k depends only on the admittivities of the four cells surrounding a node (i_s, j_s) , with a receiver, and sensitivities are only computed for the resistivities of two such cells, that is, those immediately below the surface. Consequently, the indices of the involved model parameters are $i_s - 1/2$, $j_s + 1/2$ and $i_s + 1/2$, respectively. For brevity, the notation $i = i_s$ and $j = j_s$ is used. Eqs (A23) and (A25) yield

$$\begin{split} \frac{\partial \mathbf{a}_{k}^{T}}{\partial \rho_{i\pm 1/2,j+1/2}} \mathbf{x} &= \mathbf{j}_{y}^{k} \partial \hat{\mathcal{L}}_{i,j}^{\text{avg}\pm} + \frac{1}{\hat{y}_{i,j}^{\text{avg}}} \frac{1}{2} \frac{\Delta z_{j-1/2} \Delta z_{j+1/2}}{\Delta z_{j+1/2} + \Delta z_{j-1/2}} \\ & \left\{ -\hat{z} \frac{\partial \hat{\mathcal{L}}_{i,j}^{d}}{\partial \rho_{i\pm 1/2,j+1/2}} H_{x}^{i,j} + \frac{1}{\Delta y_{i-1/2} + \Delta y_{i+1/2}} \cdot \right. \\ & \frac{\partial}{\partial \rho_{i\pm 1/2,j+1/2}} \left[\hat{\hat{y}}_{i,j}^{d} \left(\frac{1}{\hat{y}_{i+1/2,j+1/2}} - \frac{1}{\hat{y}_{i-1/2,j+1/2}} \right) \right] \\ & \left(\frac{H_{x}^{i+1,j}}{\Delta y_{i+1/2}} + \frac{\Delta y_{i+1/2} - \Delta y_{i-1/2}}{\Delta y_{i-1/2} \Delta y_{i+1/2}} H_{x}^{i,j} - \frac{H_{x}^{i,j} - H_{x}^{i-1,j}}{\Delta y_{i-1/2}} \right) \right\} \\ &= \mathbf{j}_{y}^{k} \partial \hat{\mathcal{L}}_{i,j}^{\text{avg}\pm} + \frac{1}{\hat{y}_{i,j}^{\text{avg}}} \frac{1}{2} \frac{\Delta z_{j-1/2} \Delta z_{j+1/2}}{\Delta z_{j+1/2} + \Delta z_{j-1/2}} \\ & \left[\left(-\hat{z} \partial \hat{\underline{y}}_{i,j}^{d\pm} + \frac{\Delta y_{i+1/2} - \Delta y_{i-1/2}}{\Delta y_{i-1/2}} P_{i,j}^{\pm} \right) H_{x}^{i,j} \right. \\ & \left. + \frac{1}{\Delta y_{i+1/2}} P_{i,j}^{\pm} H_{x}^{i+1,j} - \frac{1}{\Delta y_{i-1/2}} P_{i,j}^{\pm} H_{x}^{i-1,j} \right], \end{split}$$
 (C10)

where the definitions

$$\begin{split} \partial \hat{\underline{y}}_{i,j}^{\text{avg}\pm} &= \frac{\partial}{\partial \rho_{i\pm 1/2,j+1/2}} \left(\frac{1}{\hat{y}_{i,j}^{\text{avg}}} \right) \\ &= \frac{\Delta y_{i+1/2} + \Delta y_{i-1/2}}{\left(\hat{y}_{i,j}^r \Delta y_{i+1/2} + \hat{y}_{i,j}^l \Delta y_{i-1/2} \right)^2} \Delta y_{i\pm 1/2} \frac{\Delta z_{j+1/2}}{\Delta z_{j+1/2} + \Delta z_{j-1/2}} \sigma_{i\pm 1/2,j+1/2}^2 \\ &= \frac{1}{\hat{y}_{i,j}^{\text{avg}}} \frac{1}{\hat{y}_{i,j}^r \Delta y_{i+1/2} + \hat{y}_{i,j}^l \Delta y_{i-1/2}} \Delta y_{i\pm 1/2} \frac{\Delta z_{j+1/2}}{\Delta z_{j+1/2} + \Delta z_{j-1/2}} \sigma_{i\pm 1/2,j+1/2}^2, \end{split}$$

$$\begin{split} \partial \hat{y}_{i,j}^{d\pm} &= \frac{\partial \hat{y}_{i,j}^d}{\partial \rho_{i\pm 1/2,j+1/2}} \\ &= -\frac{\Delta y_{i+1/2} + \Delta y_{i-1/2}}{\left(\frac{1}{\hat{y}_{i+1/2,j+1/2}} \Delta y_{i+1/2} + \frac{1}{\hat{y}_{i-1/2,j+1/2}} \Delta y_{i-1/2}\right)^2} \Delta y_{i\pm 1/2} \frac{\sigma_{i\pm 1/2,j+1/2}^2}{\hat{y}_{i\pm 1/2,j+1/2}^2} \\ &= -\frac{\frac{\hat{y}_{i,j}^d}{\hat{y}_{i+1/2,j+1/2}} \Delta y_{i+1/2} + \frac{1}{\hat{y}_{i-1/2,j+1/2}} \Delta y_{i-1/2}}{\hat{y}_{i+1/2,j+1/2}^2} \Delta y_{i\pm 1/2} \frac{\sigma_{i\pm 1/2,j+1/2}^2}{\hat{y}_{i\pm 1/2,j+1/2}^2}, \\ P_{i,j}^{\pm} &= \frac{1}{\Delta y_{i+1/2} + \Delta y_{i-1/2}} \frac{\partial}{\partial \rho_{i\pm 1/2,j+1/2}} \left[\hat{y}_{i,j}^d \left(\frac{1}{\hat{y}_{i+1/2,j+1/2}} - \frac{1}{\hat{y}_{i-1/2,j+1/2}} \right) \right] \\ &= \frac{1}{\Delta y_{i+1/2} + \Delta y_{i-1/2}} \left[\partial \hat{y}_{i,j}^{d\pm} \left(\frac{1}{\hat{y}_{i+1/2,j+1/2}} - \frac{1}{\hat{y}_{i-1/2,j+1/2}} \right) \pm \hat{y}_{i,j}^d \frac{\sigma_{i\pm 1/2,j+1/2}^2}{\hat{y}_{i\pm 1/2,j+1/2}^2} \right] \end{split}$$

were used. The quantity $\hat{y}_{i,j}^{\text{avg}}$ is given according to eq. (A7).

The derivative of the system matrix of the forward problem **K** w.r.t. a single model parameter m^l in eq. (C7) results in a matrix $\partial \mathbf{K}/\partial m^l$ that has only four rows with non-zero entries. The parameter $m^l = \rho_{i+1/2, j+1/2}$ enters into the rows of **K** that correspond to the central nodes (i, j), (i, j+1), (i+1, j) and (i+1, j+1) (cf. Fig. A1), that is, into rows number

$$iul = (i-2)(N_z - 1) + (j-1)$$
 (C11)

$$idl = (i-2)(N_z - 1) + j$$
 (C12)

$$iur = (i-1)(N_z - 1) + (j-1)$$
 (C13)

$$idr = (i-1)(N_z - 1) + j.$$
 (C14)

The computation of $\partial \mathbf{K}/\partial m^l$ is further simplified by the symmetry of \mathbf{K} . For a central node (i,j) the coefficient of the EM field component at its right-hand side node is the same as the coefficient of the EM field component at the left-hand side node of its neighbouring central node (i+1,j). Similarly, for a central node (i,j) the coefficient of the EM field component at its lower node is the same as the coefficient of the EM field component at the upper node of its neighbouring central node (i,j+1). Furthermore, as the left- and right-hand coefficients contain vertically averaged inverse admittivities and the lower and upper coefficients contain horizontally averaged inverse admittivities, the derivative of the coefficient of the right-hand node of the central node (i,j) w.r.t. $\rho_{i+1/2,j+1/2}$ equals the derivative of the coefficients of the right-hand node of its neighbouring central node (i,j+1) w.r.t. $\rho_{i+1/2,j+1/2}$. Similar rules are valid for the coefficients of left-hand, upper and lower nodes at correspondingly neighbouring nodes. Hence,

$$\frac{\partial \mathbf{K}(iul, iul + (N_z - 1))}{\partial \rho_{i+1/2, j+1/2}} = \frac{\partial \mathbf{K}(idl, idl + (N_z - 1))}{\partial \rho_{i+1/2, j+1/2}} = \frac{\partial \mathbf{K}(iur, iur - (N_z - 1))}{\partial \rho_{i+1/2, j+1/2}}
= \frac{\partial \mathbf{K}(idr, idr - (N_z - 1))}{\partial \rho_{i+1/2, j+1/2}} = 2\frac{\Delta z_{j+1/2}}{\Delta y_{i+1/2}} \frac{\sigma_{i+1/2, j+1/2}^2}{\hat{y}_{i+1/2, j+1/2}^2},$$
(C15)

$$\frac{\partial \mathbf{K}(iul, iul+1)}{\partial \rho_{i+1/2, j+1/2}} = \frac{\partial \mathbf{K}(iur, iur+1)}{\partial \rho_{i+1/2, j+1/2}} = \frac{\partial \mathbf{K}(idl, idl-1)}{\partial \rho_{i+1/2, j+1/2}}
= \frac{\partial \mathbf{K}(idr, idr-1)}{\partial \rho_{i+1/2, j+1/2}} = 2\frac{\Delta y_{i+1/2}}{\Delta z_{j+1/2}} \frac{\sigma_{i+1/2, j+1/2}^2}{\hat{y}_{i+1/2, j+1/2}^2},$$
(C16)

$$\frac{\partial \mathbf{K}(iul, iul)}{\partial \rho_{i+1/2, j+1/2}} = \frac{\partial \mathbf{K}(iur, iur)}{\partial \rho_{i+1/2, j+1/2}} = \frac{\partial \mathbf{K}(idl, idl)}{\partial \rho_{i+1/2, j+1/2}}
= \frac{\partial \mathbf{K}(idr, idr)}{\partial \rho_{i+1/2, j+1/2}}
= -2 \frac{\Delta z_{j+1/2}}{\Delta y_{i+1/2}} \frac{\sigma_{i+1/2, j+1/2}^2}{\hat{y}_{i+1/2, j+1/2}^2} - 2 \frac{\Delta y_{i+1/2}}{\Delta z_{j+1/2}} \frac{\sigma_{i+1/2, j+1/2}^2}{\hat{y}_{i+1/2, j+1/2}^2}.$$
(C17)

C2 TE-mode

In the TE-mode, H_y is expressed through \mathbf{b}_k and E_x according to eq. (A17) and \mathbf{a}_k is zero except for the kth entry, which is 1. Hence, $\mathbf{a}_k^T \mathbf{x} = E_x^k$,

$$\mathbf{b}_{k}^{T}\mathbf{x}=H_{v}^{k}$$

© 2008 The Authors, *GJI*, **175**, 486–514 Journal compilation © 2008 RAS

and

$$\mathbf{c}_k = \frac{1}{H_y^k} \left(0, \dots, 0, \underbrace{1}_{k \text{th entry}}, 0, \dots, 0 \right) - \frac{Z_{xy}^k}{H_y^k} \mathbf{b}_k, \tag{C18}$$

$$\mathbf{d}_{kl} = -\frac{Z_{xy}^k}{H_x^k} \frac{\partial \mathbf{b}_k}{\partial m^l},\tag{C19}$$

as \mathbf{a}_k does not depend on any model parameter.

The derivative in $\mathbf{d}_{k1}^T \mathbf{x}$ is computed from eq. (A17) as

$$\frac{\partial \mathbf{b}_{k}^{T}}{\partial \rho_{i\pm 1/2, j+1/2}} \mathbf{x} = \frac{1}{2} \frac{\Delta z_{j+1/2} \Delta z_{j-1/2}}{\Delta z_{j+1/2} + \Delta z_{j-1/2}} \left(-\sigma_{i\pm 1/2, j+1/2}^{2} \Delta y_{i\pm 1/2} \frac{1}{\Delta y_{i+1/2} + \Delta y_{i-1/2}} \right) E_{x}^{i,j}.$$
(C20)

As m^l only enters into the coefficient of the central node in eq. (A8), the matrix $\partial \mathbf{K}/\partial m^l$ contains only four non-zero entries, which are all on the diagonal. Hence,

$$\frac{\partial \mathbf{K}(iul, iul)}{\partial \rho_{i+1/2, j+1/2}} = \frac{\partial \mathbf{K}(idl, idl)}{\partial \rho_{i+1/2, j+1/2}} = \frac{\partial \mathbf{K}(iur, iur)}{\partial \rho_{i+1/2, j+1/2}} = \frac{\partial \mathbf{K}(idr, idr)}{\partial \rho_{i+1/2, j+1/2}}
= -\hat{z} \left(-\sigma_{i+1/2, j+1/2}^2 \Delta z_{j+1/2} \Delta y_{i+1/2} \right).$$
(C21)

C3 VMT mode

In the VMT mode, H_z is expressed through \mathbf{a}_k and E_x according to eq. (A20) and H_y is expressed through \mathbf{b}_k and E_x according to eq. (A17). Hence,

$$\mathbf{a}_{k}^{T}\mathbf{x}=H_{\tau}^{k},$$

$$\mathbf{b}_{k}^{T}\mathbf{x}=H_{v}^{k}$$

and

$$\mathbf{c}_k = \frac{1}{H_y^k} \mathbf{a}_k - \frac{B_k}{H_y^k} \mathbf{b}_k,\tag{C22}$$

$$\mathbf{d}_{kl} = \frac{1}{H_v^k} \frac{\partial \mathbf{a}_k}{\partial m^l} - \frac{B_k}{H_v^k} \frac{\partial \mathbf{b}_k}{\partial m^l}.$$
 (C23)

The derivative in the first term of $\mathbf{d}_{k1}^T \mathbf{x}$ is computed from eq. (A20) as

$$\frac{\partial \mathbf{a}_{k}^{T}}{\partial \rho_{i\pm 1/2,j+1/2}} \mathbf{x} = \frac{1}{2} \frac{\Delta y_{i+1/2} \Delta y_{i-1/2}}{\Delta y_{i+1/2} + \Delta y_{i-1/2}} \left(\pm \sigma_{i\pm 1/2,j+1/2}^{2} \frac{\Delta z_{j+1/2}}{\Delta z_{j+1/2} + \Delta z_{j-1/2}} \right) E_{x}^{i,j}. \tag{C24}$$

The derivative in the second term of $\mathbf{d}_{kl}^T \mathbf{x}$, that is, $(\partial \mathbf{b}_k / \partial m^l)^T \mathbf{x}$, is already given by eq. (C20).

As the linear system of equations that is solved in the forward problem of the VMT is the one solved in the TE-mode, the entries of the matrix $\partial \mathbf{K}/\partial m^l$ are given as in eq. (C21).